

**Novel molecular ion implantation technology
for proximity gettering in silicon wafer
for CMOS image sensor**

Ryo Hirose

March 2020

Abstract

For the advanced CMOS image sensor fabrication, the strong proximity gettering silicon wafers are required to remove the metallic impurity contaminations during device fabrication process from device active region.

In this thesis, the characteristics of novel molecular ion implantation technology for proximity gettering technology are studied.

In the Chapter 2, the equipments which are used in this thesis are described. The basic mechanisms of ion implanter, secondary ion mass spectroscopy (SIMS), transmission electron measurement (TEM), and atom probe tomography are explained. Especially, molecular gas source is ionized by the electron impact for form the molecular ion beam in the ionization chamber of the ion implanter.

The detailed experiment for forming the novel molecular ion beam is described in the chapter 3. In this chapter, the formation of CH₃O molecular ion beam is achieved. And also the basic characteristics of CH₃O ion implantation to the silicon wafer is described. It is found that the depth of concentration peaks of implanted carbon and oxygen are formed in the same depth. This phenomenon is considered to be occurred by the difference of implantation energy due to the energy distribution according to the mass number of each atoms which consist with molecular ion. Furthermore, it is found that the ion implantation damage introduced by the CH₃O ion implantation is higher than C₂H₃ ion implantation which is conventional hydrocarbon molecular ion implantation. The increase of the ion implantation damage is considered to be caused by the oxygen as the additional atom in CH₃O ion.

In the chapter 4, the basic characteristics of CH₃O ion implanted silicon epitaxial wafer is described. The unique ion implantation defect which is determined as end of range (EOR) defect is observed in the CH₃O ion implantation region after epitaxial growth. The shape of this EOR defect is determined to the {111} stacking faults by TEM and FFT analysis. This defect is considered to be formed by the increased damage in CH₃O ion implantation. The formation behavior of EOR defects is also described. The ramping up rate of 15 °C/sec can increase the density of defect after 1100 °C. From the study of defect behavior on annealing temperature and time, the ramping up rate dependence on the density of defect after at 1100 °C for 300 sec annealing is caused by the temperature dependence of formation behavior of EOR defect and diffusion behavior of oxygen and carbon.

In the chapter 5, the effect of proximity gettering sinks introduced by the CH₃O ion implantation on the gettering capability and CMOS image sensor performance are described. The increase of gettering capability on nickel is achieved using CH₃O ion implantation. The increase of gettering capability is considered to be occurred by the EOR defect which function as gettering site. Furthermore, the decrease of the density of white spot defects is achieved using CH₃O ion implanted silicon epitaxial wafers. This result suggests that proximity gettering technology using CH₃O ion implantation can contribute to improve electrical performance of CMOS image sensors.

From these results, it can be summarized that proximity gettering technology using CH₃O molecular ion implantation technology is effective in the fabrication of advanced CMOS image sensor.

Acknowledgments

The author would like to express his deep gratitude to Associate professor Jiro Matsuo of Kyoto University for his continuous help throughout this study.

The author also would like to thank Professor Manabu Saito and Ikuo Kanno of Kyoto University for their comments, advice and helpful discussions on the manuscript.

The author would like to thank Assistant Professor Toshio Seki of Kyoto University for his comments, advice and helpful discussions on the manuscript.

This research was made possible by the Advanced Evaluation & Technology Development Department of SUMCO CORPORATION. The author would like to express deep gratitude to Representative Director, COO & President Dr. Hisashi Furuya, Executive Officer, Deputy General Manager, Technology Division Mr. Naoki Ikeda, and General Manager, Advanced Evaluation & Technology Development Department Dr. Kazunari Kurita of SUMCO CORPORATION for their continuous guidance, kind discussions, and encouragements throughout this study.

The author is very grateful to General Manager Mr. Tadashi Ikejiri, Group Manager Mr. Tsutomu Nagayama, and Dr. Naoki Miyamoto of NISSIN ION EQUIPMENT CO.,LTD. for their continuous help, kind discussions, and contributions in this study. The molecular ion implantation was carried out with their great help.

The author would like to thank to Dr. Rafael Manory for his helpful comments and supports on the manuscript.

The author would like to thank to Mr. Hideyuki Ando of Fuzzy Logic Systems Institute for gave advice on RTA treatment.

He also would like to thank to Manager Mr. Yoshihiro Koga, Assistant Manager Mr. Hidehiko Okuda, Assistant Manager Mr. Ryosuke Okuyama, Assistant Manager Mr. Takeshi Kadono, Assistant Manager Dr. Ayumi Onaka-Masada, Mr. Satoshi Shigematsu, Mr. Koji Kobayashi, Dr. Akihiro Suzuki of SUMCO CORPORATION for their significant discussions and experimental advices.

Finally, he especially thanks his parents for their continuous support and encouragement.

Contents

1. <u>Introduction</u>	1
1.1 Back ground	1
1.2 Overview of gettering technology and technical issues	8
1.3 Proximity gettering technology using ion implantation technology	11
1.4 Purpose of this study	17
2. <u>Experimental equipment</u>	18
2.1 Introduction	18
2.2 Ion implantation equipment	19
2.3 SIMS	21
2.4 TEM	25
2.5 3D-APT	29
2.6 Conclusion	31
3. <u>Development of CH₃O ion implantation technology</u>	32
3.1 Introduction	32
3.2 Ionization of diethyl ether using CLARIS®	33
3.3 Distribution depth profiles of C, H, and O after CH ₃ O ion implantation	36
3.4 Dependence of amorphous formation on CH ₃ O ion dose	41
3.5 Comparison of the ion implantation damage between CH ₃ O and C ₂ H ₃	43
3.6 Conclusion	47
4. <u>Defect formation behavior in CH₃O ion implantation region</u>	48
4.1 Introduction	48
4.2 Experimental methods	49
4.2.1 Si epitaxial growth: Sample preparation	49
4.2.2 Rapid thermal annealing (RTA) sample preparation	51
4.2.3 Analysis method	51
4.3 Characteristics of the CH ₃ O ion implantation region after Si epitaxial growth	53
4.3.1 Defect observation in the CH ₃ O ion implantation region	53

4.3.2 Diffusion behavior of C, O, and H	60
4.4 EOR defect formation behavior in the CH ₃ O ion-implanted region	64
4.4.1 Defect type in CH ₃ O ion-implanted region	65
4.4.2 Dependence of the density of CH ₃ O ion implantation defects on the ramping-up rate	68
4.4.3 Mechanism underlying defect density dependence on ramping-up rate	74
4.5 Conclusion	81

5. Characteristics of CH₃O ion implanted silicon epitaxial wafer 83

5.1 Introduction	83
5.2 Experimental sample conditions	84
5.2.1 The gettering test wafer sample	84
5.2.2 The CMOS image sensor sample	85
5.2.3 Analysis method	85
5.3 Enhancement of gettering capability using the CH ₃ O ion implantation technique	86
5.4 Characteristics and effects of the CH ₃ O ion-implantation region for CMOS image sensor fabrication processes and performance	95
5.4.1 Gettering effect of the CH ₃ O ion-implantation region on metallic impurity contamination during the CMOS image sensor device fabrication process	95
5.4.2 Diffusion behavior of implanted elements by CH ₃ O ion implantation during the CMOS image sensor fabrication process	99
5.4.2.1 C-diffusion behavior	99
5.4.2.2 O gettering behavior	101
5.4.2.3 H gettering behavior	103
5.4.3 Defect morphology observation in the CH ₃ O ion-implantation region	106
5.4.3.1 BMD formation behavior	106
5.4.3.2 CH ₃ O ion-implanted defect behavior	108
5.4.4 Reduction in white spot defect density by using CH ₃ O ion implantation	121
5.5 Conclusion	125

6. Conclusion

Chapter. 1

Introduction

1.1 Back ground

With the development of the information society and following performance improvement, solid-state imaging devices have been used for a variety of purposes. Today, high-quality images can be obtained by improving the performance of a solid-state imaging device mounted on a smartphone. These captured images can now be easily shared using social networking services (SNS), and such services are essential to daily life.

In addition, the use of solid-state imaging devices is becoming more and more widespread in society; for example, the adoption of safety equipment for motor vehicles, the increase in surveillance cameras, and their application in medical devices for the purpose of safety improvements. For use in vehicles, solid-state image sensors require high-sensitivity performance to establish automatic driving technology. In traditional smartphones, one solid-state image sensor was mounted in one unit. However, in recent years, to obtain higher-quality images, more than four solid-state image sensors are mounted. In this way, solid-state imaging devices have become indispensable in modern society, and it is considered that demand will increase in the future together with higher performance.

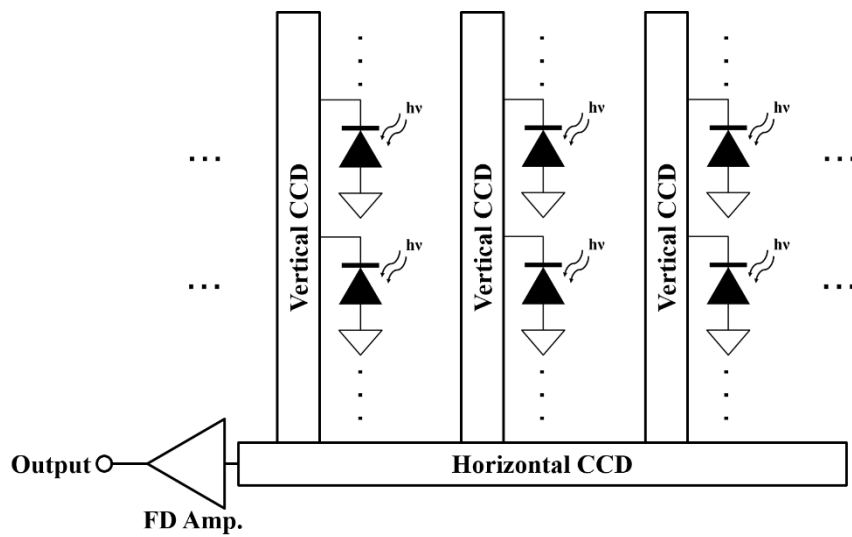
The solid-state imaging device was developed by Schuster *et al.* in 1966 [1]. Various types of solid-state image sensors have been developed from this invention, but two types

of image sensors are used currently: charge-coupled device (CCD) and complementary metal oxide semiconductor (CMOS).

A schematic image of the CCD and CMOS image sensor systems is shown in Figure 1.1. The CCD image sensor was invented by Boyel and Smith at Bell Laboratories in 1969, and was reported in the following year [2]. The basic structure of a CCD image sensor is as follows [3]. The charge obtained by photoelectric conversion with a photodiode (PD) is stored in a metal oxide semiconductor (MOS) capacitor. The accumulated electric charge is detected by its transfer to a floating diffusion (FD) amplifier using two vertical and one horizontal CCDs. Because the CCD image sensor outputs the charges accumulated for all pixels simultaneously, it can reduce the distortion of the image when shooting an object moving at high speed. Furthermore, the number of FD amplifiers in a CCD is lower than that of a CMOS image sensor. For this reason, there was merit in the fact that the variation in an FD amplifier could be reduced, so that practical use and high image quality were promoted earlier than the CMOS image sensor.

By contrast, the CMOS image sensor is faster than CCD, and the prototype is an image sensor using bipolar phototransistors reported by Schuster *et al.* in 1966 [1]. The CCD image sensor transfers the stored charge, as shown in the structural diagram in Figure 1.1. By contrast, in the case of the CMOS image sensor, there is an amplifying element for each pixel and the charge in the PD changes the signal voltage on the spot. After conversion, the signal voltage is transferred to the output circuit. Therefore, it has a feature that it is strong against noise during transfer because of the signal is amplified before the transfer.

(a)



(b)

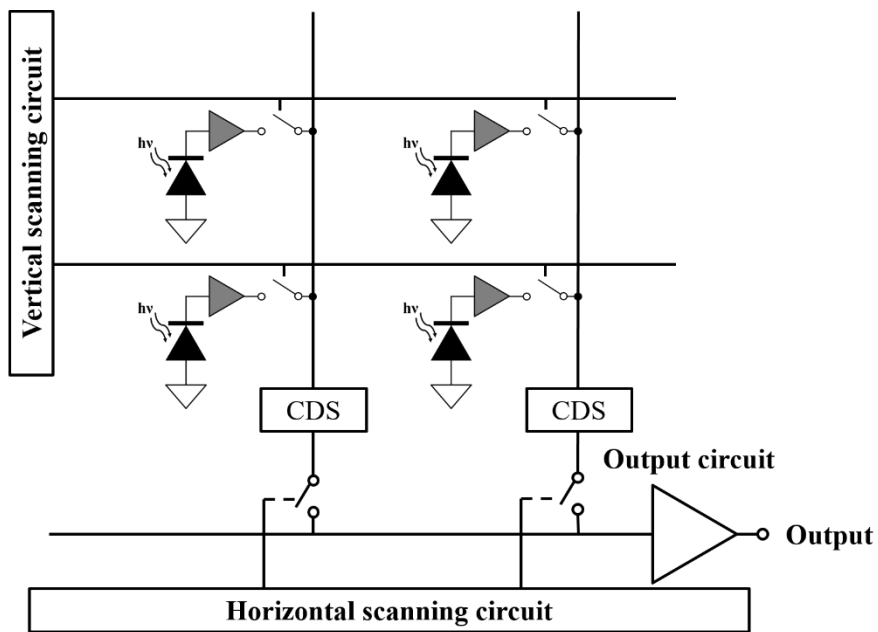


Fig. 1.1. Schematic diagrams of the image sensor system (a) CCD, (b) CMOS

In addition, because CMOS image sensors are manufactured in a general semiconductor manufacturing process, it is possible to form a system-on-chip that can form various integrated circuits on the same substrate and add new functions [4-10]. There have been a few technical issues such as noise due to the variations in the amplifier circuit in each pixel [11, 12].

There are two types of electrical noise in CMOS image sensors: random noise, which lowers the sensitivity of the entire image sensor, and fixed pattern noise, which originates from a specific pixel where some cause occurred. In addition, there are two types of cases that occur in PDs and cases that occur in electric circuits. Thus, the electrical noises are roughly classified into four types. There is a random noise at the level of $1/f$ that is generated in the electric circuit in the solid-state imaging device [13-17]. It is known that this noise is mainly generated in the amplifier circuit. The transistor constituting the amplifier circuit has an insulating film and a Si crystal interface. At this interface, there exists an interface level due to the Si dangling bonds, and a shallow level is formed in the band gap of the Si crystal. This interface state easily generates charges by external energy such as thermal energy, which causes electrical noise. To reduce this noise, noise removal techniques such as using a correlated double sampling (CDS) circuit were developed [11, 12].

One example of random noise generated in PDs is the dark current shot noise. This noise is generated due to the shallow-level state formed by interface states existing in PD similar to the $1/f$ noise. As a method for removing this noise, there is an embedded PD technology that forms a high-concentration B layer on the surface of the PD region [12, 18, 19]. This technology forms an electrical potential barrier against electrons by forming a high-concentration B layer on the PD surface. This potential barrier enables us to

separate the generation and recombination of the electron and hole pairs generated in the PD surface layer and the PD, respectively, and contributes significantly to noise reduction in CMOS image sensors.

Examples of fixed pattern noise in a PD are the “white spot defects” caused by metallic impurity contamination during device processing [20-22]. A schematic image of the PD is shown in Figure 1.2. In the PD, photoelectric conversion is performed by generation and separation of electrons and holes using energy obtained by absorbing incident light. The light intensity is determined by the density of electrons and holes generated at this time. Therefore, it is important to increase the sensitivity of the CMOS image sensor by converting the incident light energy into a pair of electrons and holes without waste and extracting this pair as an electrical signal. Here, it is known that metallic impurity elements form an energy level in a deep region in the band gap of an Si crystal. This deep energy level serves as a starting point for easily forming a pair of electrons and holes by external energy other than light, such as heat. Therefore, a phenomenon called “white spot defect” occurs in which a pair of electrons and holes is formed even when light is not incident due to contamination of a metallic impurity in the PD, and current is detected.

In CMOS image sensors, it is known that the factor of the dark current is classified by three; surface generation current, diffusion current, and generation current [23]. The Surface generation current is caused in the surface of PD. The amount of current at a room temperature is known highest in the dark current. The surface current can be suppressed by making an inversion layer at the surface of the PD [23]. The diffusion current is caused by the diffusion of minority carrier from the bulk of silicon substrate to the PD. The amount of this current is the smallest in the dark current at a room temperature. The generation current is caused by deep energy levels formed by the metallic contaminations.

As shown in Fig. 1.3, the generation current is much higher than diffusion current at room temperature. If there is no generation current, it is expected that the dark current can be reduced to 1/10 at room temperature. Furthermore, the PD is known to be very sensitive to metallic impurity contamination, and there are reports that it is affected by very low concentrations of contamination of about 10^6 cm^{-2} [24].

Therefore, removing metallic impurity contamination from a device formation region such as a PD in a CMOS image sensor is a serious technical issue for improving the performance and the device yield.

In a device process, gettering is a technique for removing metallic impurity contamination from the device formation region [25, 26]. This is a technique for forming a gettering sink that functions as a metallic impurity capture site, outside the device formation region. Therefore, the development of a more effective gettering technology is required for advanced CMOS image sensors.

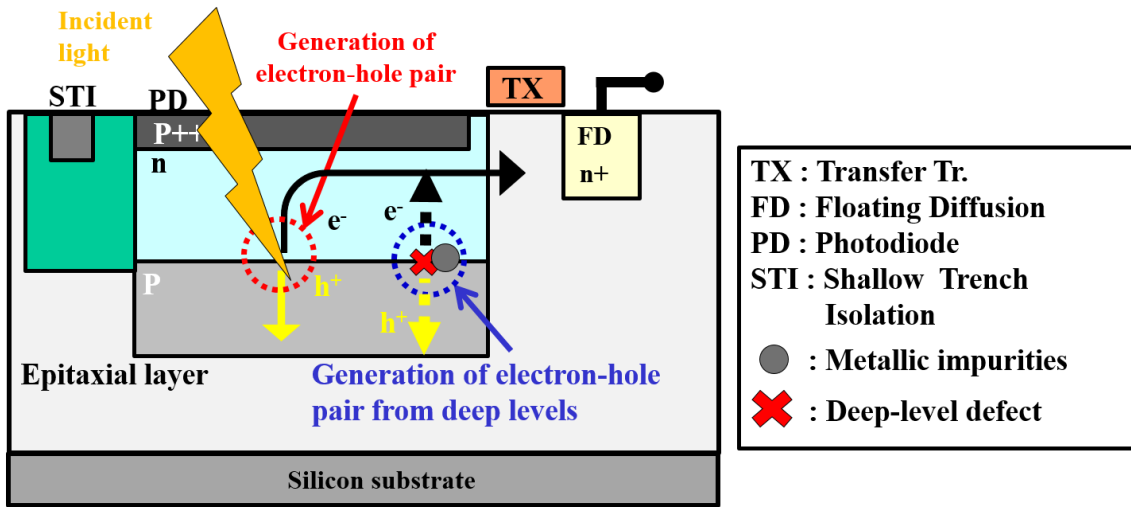


Fig. 1.2. Schematic diagram of the PD

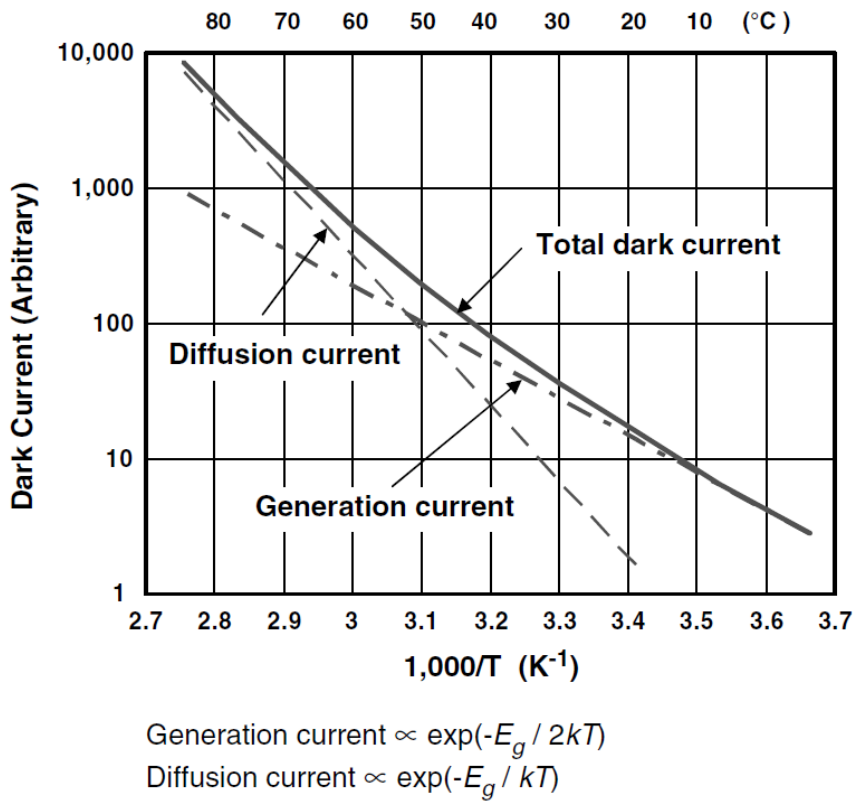


Fig. 1.3. Temperature dependence of dark current [23]

1.2 Overview of gettering technology and technical issues

As mentioned in Section 1.1, there is an improvement in the technical problem of the gettering capability of Si wafers for solid-state imaging devices. Because the image pickup element is formed on the surface layer of the Si wafer, the surface layer of the wafer cannot be processed. Therefore, a gettering technique has been developed by processing the back surface or the bulk region of the Si wafer. A schematic image of each gettering technology is shown in Figure 1.4.

The first gettering technology is extrinsic gettering (EG), which forms a gettering sink by processing the back side of the Si wafer [25-39]. This technology forms a gettering sink by forming a film such as polysilicon or by intentionally forming a damage layer using ion implantation or mechanical processing on the back surface. This technique has the advantage that a gettering sink can be formed without any special treatment during the device process. On the other hand, in EG, the formation region of the gettering sinks is far from the device formation region. Thus, in a recent heat treatment of a device becomes at a low temperature and for a short time, the metallic impurities did not diffuse to the gettering sink during the device process, and the EG did not function satisfactorily.

To solve this issue, intrinsic gettering (IG) was developed as a method of forming a gettering sink closer to the device formation region. As the most general IG method, there is a technique for forming an oxygen precipitate that becomes a gettering sink inside a Si wafer [25, 26, 40-47]. This technology consists of precipitating oxygen eluted from the quartz crucibles used to form Si single crystals by heat treatment. Therefore, IG can impart a gettering sink without any special process except heat treatment, and the gettering sink can form closer to the device formation region than in EG. In recent device processes, the heat treatment temperature has been lowered and the time has been

shortened. Such processes achieved neither a high enough temperature nor a heat treatment that was long enough for precipitating dissolved O in Si crystals, and therefore they did not achieve sufficient gettering ability.

To solve this problem, a technique of doping a trace amount of C or N that promotes O precipitation is also used [26, 48, 49]. However, IG is still required for the heat treatment to form the gettering sinks.

Proximity gettering technology using ion implantation technology has been developed as a technology for forming a gettering sink closer to the device formation region without requiring a high temperature and a long heat treatment.

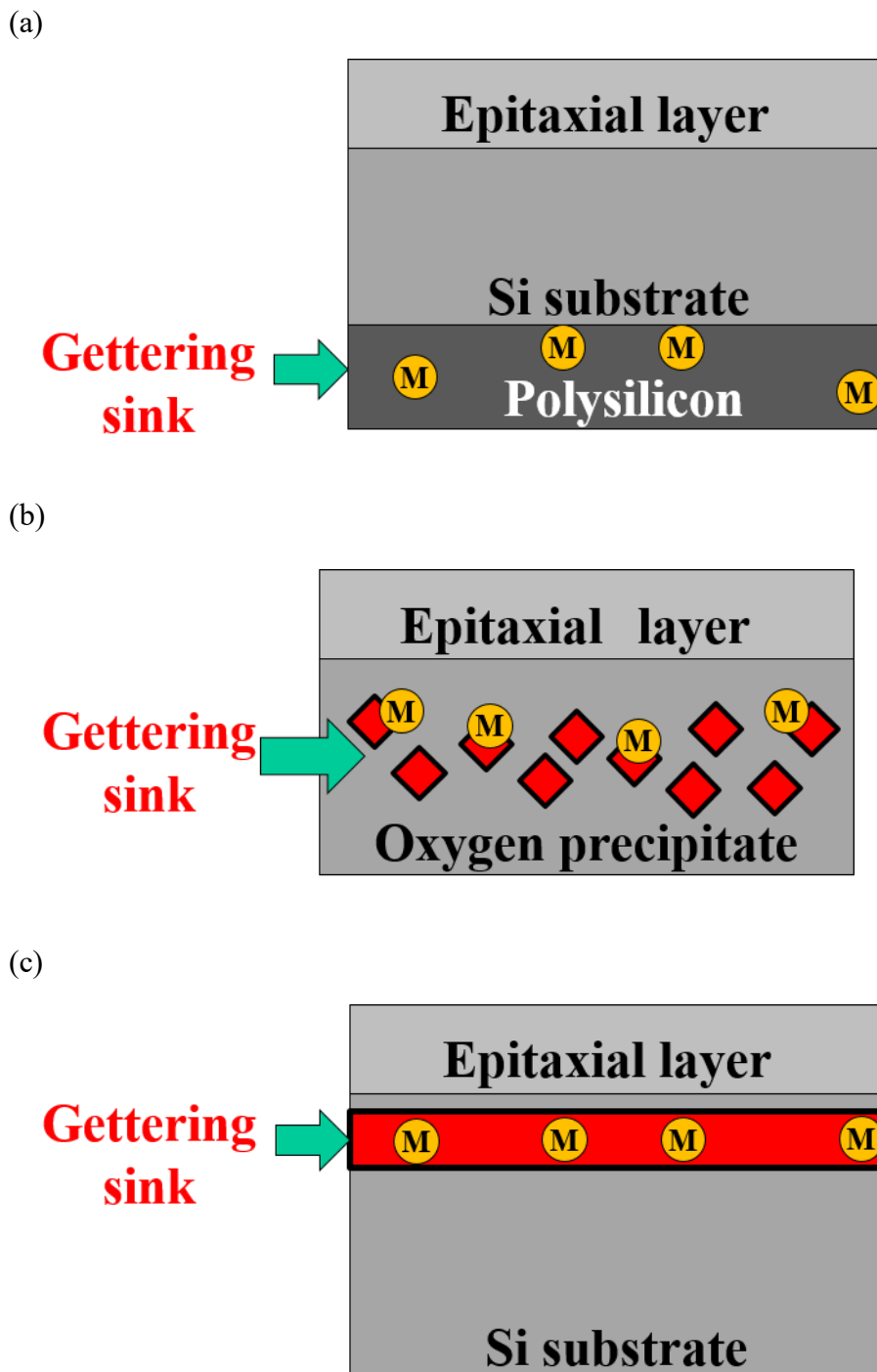


Fig. 1.4. Schematic diagram of each gettering technology:

(a) EG, (b) IG, and (c) proximity gettering

1.3 Proximity gettering technology using ion implantation technology

To form the gettering sinks near the device formation region, a gettering technology using high-energy ion implantation has been studied. Kuroi *et al.* studied proximity gettering technology using high-energy ion implantation with various monomer ions [50]. They reported that secondary defects formed in the ion implantation region after the recovery annealing function as gettering sinks.

For CMOS image sensor manufacturing processes, an epitaxial wafer with high-energy ion implantation of C monomer ions are used [51-53]. These technologies can form a gettering sink closer to the device formation region at a lower temperature and in a shorter time than the O precipitation heat treatment in IG. Furthermore, the gettering sink can be formed uniformly. On the other hand, in case of high-energy ion implantation technology, the formed secondary defects may be extended by heat treatment during the device process, and may reach the device formation region to induce defects. Another issue is that a recovery heat treatment is necessary to the fabrication of Si epitaxial wafers. This recovery heat treatment cause an increase in Si wafer costs and may contaminate the Si wafer by metallic impurities.

Therefore, our group has developed a gettering technology using hydrocarbon molecular ion implantation technology for forming a gettering sink closer to the device formation region and without requiring a recovery heat treatment [54-61]. Figure 1.5 shows a schematic image of the manufacturing process of the hydrocarbon molecular ion implanted Si epitaxial wafers. This technique is characterized by implantation of molecular ions composed of a plurality of carbons and hydrogens and epitaxially growing a Si single crystal on the implanted surface.

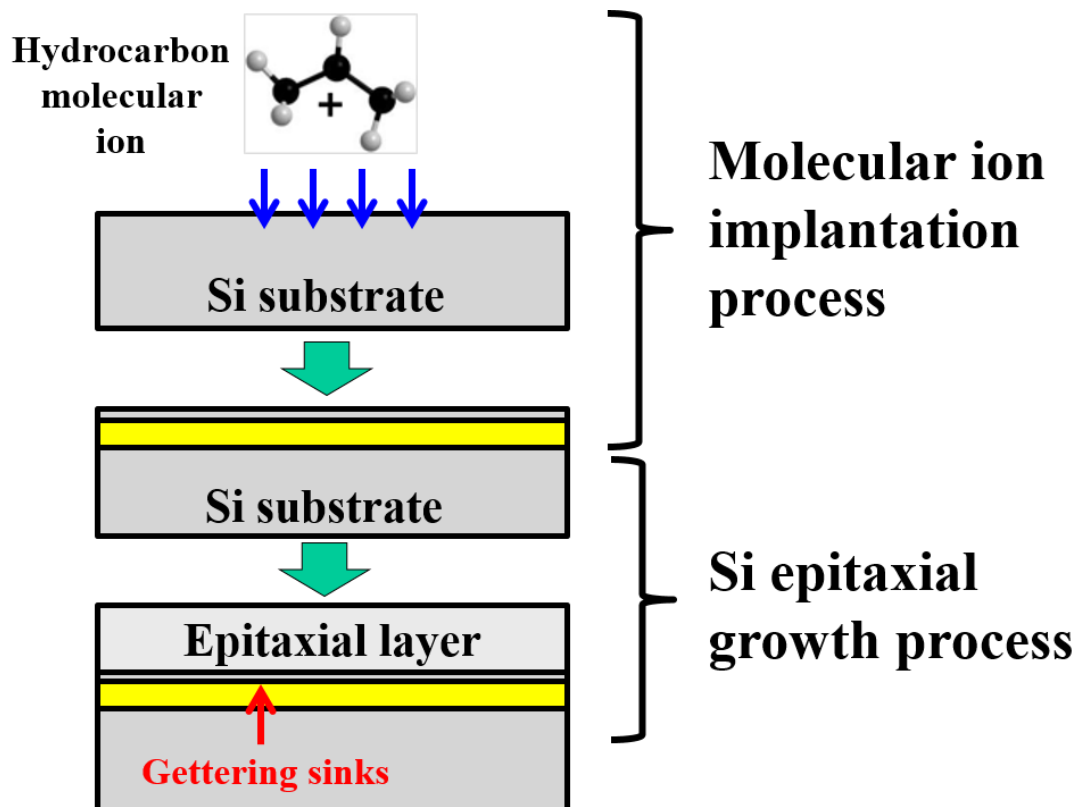


Fig. 1.5. Schematic diagram of the manufacturing process of hydrocarbon molecular ion implanted Si epitaxial wafers

The molecular ion implantation technology used in this technique was developed based on the cluster ion-beam-forming technology developed by Yamada *et al.* [62-64]. Gas cluster ion beams are obtained by clustering thousands of argon atoms by adiabatic compression and ionizing them using electron impact [62, 63]. In the case of hydrocarbon molecular ion implantation, the molecular ion beam is obtained by the ionization of hydrocarbon molecules such as cyclohexane using electron impact. Therefore, the molecular ion beam used in this technology is also a cluster ion beam in that it is composed of a plurality of elements, but the ion is generated using fragment ions, which are obtained by ionizing a hydrocarbon compound. Because of the formation, the author calls it “molecular ion implantation.”

From previous studies, a hydrocarbon molecular ion implanted Si epitaxial wafer is known to have three characteristics. One is the high gettering capability for metallic impurity contamination in the implantation region. Kurita *et al.* reported that concentration peaks of metallic impurity contamination were observed after the p–n junction formation processes. The second is the O-trapping capability in the ion implantation region. As described in Section 1.2, there is a certain O concentration in the Si substrate used for the Si epitaxial wafer. Kaneda *et al.* proposes that O diffused from the Si substrate and B implanted into the device formation region form a complex that forms deep-level states, which may degrade the performance of the image sensor [65, 66].

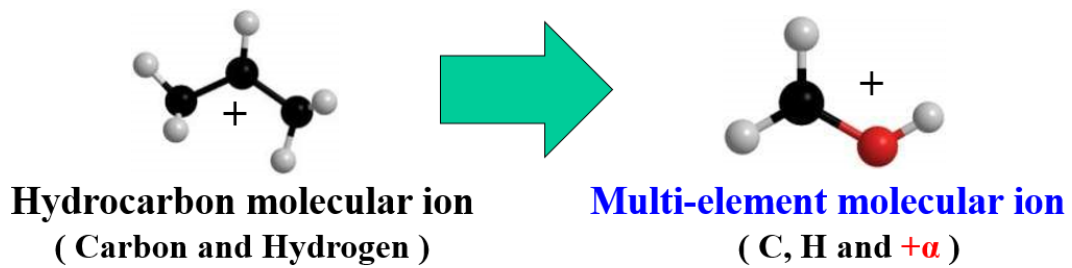
The O-trapping capability of the hydrocarbon ion implantation region achieves a low O concentration of the epitaxial layer by trapping O that diffuses from the substrate to the epitaxial layer during the device process. The third characteristic is the passivation effect by H trapped in the hydrocarbon molecular ion implantation region. Okuyama *et al.* reported that a high H concentration remains in the hydrocarbon molecular ion

implantation region after epitaxial growth, and this H is released from the implanted region during subsequent heat treatment [61]. They reported that the amount of H released at this time is higher than the conventional density of dangling bonds at the Si/SiO₂ interface [67]. Therefore, the released H is expected to passivate the interface region during heat treatment in the device fabrication process.

Si epitaxial wafers ion-implanted with hydrocarbon molecules with these characteristics have been demonstrated to improve the electrical characteristics of CMOS image sensors and were commercialized. However, the demand for a CMOS image sensor with a higher sensitivity is expected to increase, and development of a technology that induces a better gettering capability to the Si wafer is required. To respond to this technical issue, we have conceived and developed a multi-element molecular ion implantation technology, which is based on the hydrocarbon molecular ion implantation technology.

Figure 1.6 shows the concept of multi-element molecular ion implantation technology. Whereas the hydrocarbon molecular ion is used for implanting molecular ions consisting of multiple carbons and hydrogens, the multi-element molecular ion implantation technique consists of three elements, with one element in addition to C and H. As already noted, in the case of hydrocarbon molecular ion implantation, molecular ions consisted of two kinds of elements: C, which can form a gettering sink for metallic impurity contaminations, and H, which is expected to have a passivation effect on the interface state. However, these two types of elements are not the only elements expected to have gettering and passivation effects by ion implantation. As shown in Fig. 1.6, for example, F diffuses to the Si/SiO₂ interface, and a passivation effect is expected by passivating the dangling bonds of Si [68-70].

Concept of multi-element molecular ion implantation



Example of α element

Period /Group	13	14	15	16	17	18
1						He
2	B	C	N	O	F	Ne
3	Al	Si	P	S	Cl	Ar
4	Ga	Ge	As	Se	Br	Kr

Purpose



Gettering



Passivation

Fig. 1.6. Concept of multi-element molecular ion implantation technology

In addition, it is known that a Si crystal layer containing a high concentration of B has a gettering effect for the metallic impurity contamination of elements such as Fe by forming Fe–B pairs [25, 26]. Thus, it is expected that the gettering capability or passivation effect is improved using multi-element molecular ion implantation for proximity gettering technology.

In this study, we worked on the development of molecular ion implantation technology consisting of three elements—C, H, and O—for the purpose of further improving gettering capability. Oxygen is expected to form a gettering sink different from the gettering sinks formed by C. Shirasawa *et al.* reported the result of first-principles calculations by density functional theory (DFT) that vacancies and O in the ion implantation region are expected to function as gettering sinks by forming VO pairs [71-73]. Kuroi *et al.* reported that secondary defects formed in the implanted region by oxygen monomer high-energy ion implantation function as gettering sinks [50]. Therefore, additional O is expected to improve the gettering capability of an ion implantation region.

1.4 Purpose of this study

This thesis aims to further improve the gettering capability of hydrocarbon molecular ion implantation technology, and has developed a new molecular ion implantation technology consisting of three elements of C, H, and O, and the characteristics of Si epitaxial wafers using this technology.

Chapter 2 summarizes the ion implanter and analyzer used in this study.

In Chapter 3, the development of CH₃O ion implantation technology using a new gas source and the analysis of ion implantation characteristics for Si wafers are described.

Chapter 4 provides the results of investigations on the basic characteristics of Si epitaxial wafers using the CH₃O ion implantation technique. In the CH₃O ion implantation region, it has been found that unique ion implantation defects that cannot be formed in the hydrocarbon molecular ion implantation region are formed. The formation behavior of this specific defect is summarized.

In Chapter 5, we investigated the effect of proximity gettering technology using CH₃O ion implantation on the CMOS image sensor fabrication processes. In addition, from the electrical characteristics evaluation of the CMOS image sensor, it was found that the density of the white defects in CMOS image sensor can be reduced using CH₃O ion-implanted Si epitaxial wafers.

Finally, Chapter 6 presents a summary of the results of this study.

Chapter. 2

Experimental equipment

2.1 Introduction

In Chapter 1, we stated the importance of making improvements in gettering capability. In a previous study of ion implantation technology for proximity gettering technology, a monomer or molecular ion was used. In the case of monomer ion implantation, several kinds of atoms are used. As indicated by Kuroi *et al.*, high-energy monomer ions such as B, O, and other implanted ions can form gettering sinks [50]. In the case of molecular ion implantation, Kurita *et al.* reported that gettering sinks can be formed using hydrocarbon molecular ion implantation [58]. However, the effect of molecular ions consisting of three kinds of atoms has not been reported. Therefore, we will first try to develop a new molecular ion implantation consisting of three kinds of atoms using ion implantation equipment.

The origin of gettering sinks are defects in the Si crystal. As Kuroi *et al.* reported, the EOR defects introduced by the monomer ion implantation act as gettering sinks [50]. In the case of gettering technology using hydrocarbon molecular ion implantation, the 5nm sized defects formed by the aggregation of implanted carbon act as gettering sinks. Thus, the analysis of the defect in the ion implantation region and the distribution profile of implanted atoms are important for understanding the mechanism of gettering technology. In this study, we use secondary ion mass spectrometry (SIMS) to analyze the distribution depth profiles of atoms. Transmission electron microscopy (TEM) and Scanning TEM (STEM) were used to analyze the defect formation behavior in the ion implantation region.

Atomic scale analysis on the distribution of atoms around defects was performed using three-dimensional atomic probe tomography (3D-APT).

In this section, we describe the operation of the equipment and the analytical methods that were used in this study.

2.2 Ion implantation equipment [62-64, 74-77]

For the development of new molecular ion implantation, we used the CLARIS® machine, which is the ion implantation instrument made by NISSIN. This ion implanter can process 12-inch Si wafers. A schematic diagram of the ion implantation instrument is shown in Figure 2.1. The ion implantation equipment consisted of an ionization chamber, an acceleration electrode, a mass spectrometer, a beam focusing system and a process chamber. In the ionization chamber, molecular ions and radical fragments are formed by fragmentation of gas source in the ionization using the electron impact. For the hydrocarbon molecular ion implantation, a hydrocarbon molecule such as cyclohexane is used as the gas source. Because the hydrocarbon molecule consisted of several C and H atoms, the molecular ion formed after ionization also consisted of several C and H atoms. In this study, we used diethyl ether as a new gas source for the formation of the multi-element molecular ion. The molecular ions are accelerated by the acceleration electrode. The maximum acceleration energy in CLARIS® is 80 keV [77]. In this study, the acceleration energy was 80 keV. After acceleration, the molecular ions are separated according to their mass by the magnetic mass separation system.

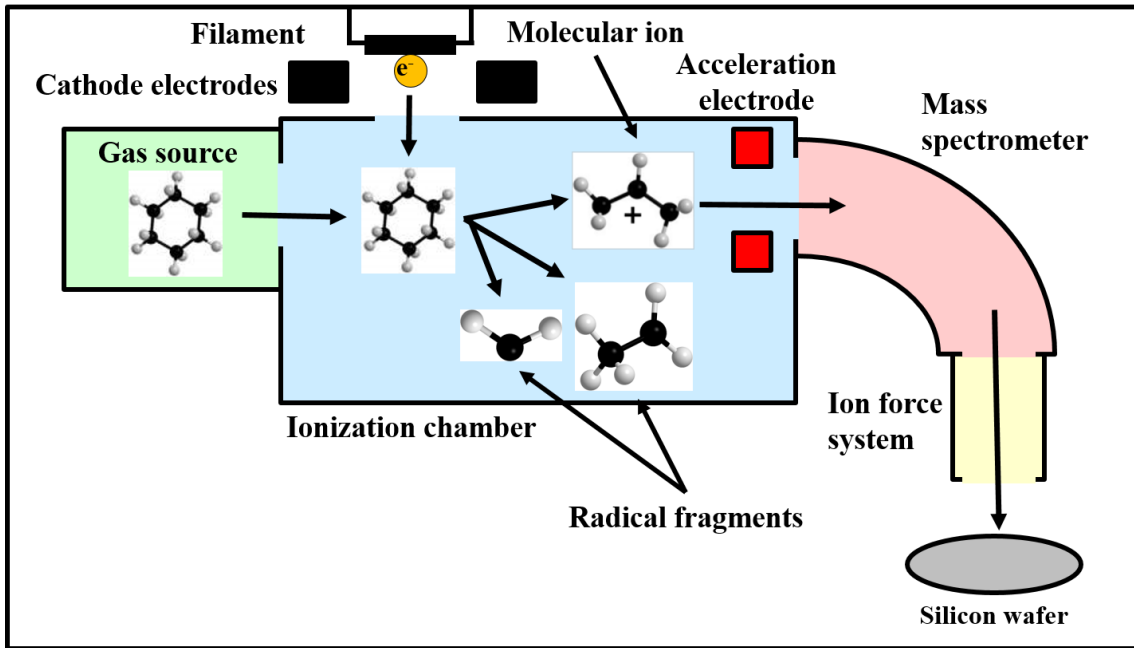


Fig. 2.1. Schematic diagram of the ion implantation apparatus

The mass spectrum was obtained by measuring the beam current with a Faraday cup and varying the magnetic field strength of the mass separator. The focused molecular ion beam is formed by the beam focusing system after mass separation in the process chamber. Beam focusing is performed by the electric or magnetic field [62, 77]. In the case of CLARIS®, a magnetic quadrupole triplet lens was used [77]. Finally, the focused ion beam is irradiated onto the Si wafer in the process chamber. The maximum ion beam current depends on the molecular ion species; it is reported that $B_{18}H_x^+$ can be implanted at 3.5 mA using CLARIS® [77].

2.3 SIMS [78-80]

In this study, we used a Cameca SIMS instrument to determine the concentration depth profiles of implanted atoms such as C, H, and O, and metallic impurities such as Fe, Cu, and Ni.

The SIMS analysis was performed by mass separation of secondary ions formed by irradiation of primary ions such as O^- , O_2^+ or Cs^+ [78]. Figure 2.2 shows an example of a SIMS instrument. A SIMS apparatus consists of a primary ion irradiation system, a secondary ion optics system, and a signal processing system [78]. In the primary ion irradiation system, the primary ion is formed using an ionization system such as a surface ionization ion source and duoplasmatron. The primary ion is highly purified by the separator and then focused by the condenser and objective lens. After that, the primary ion beam is irradiated onto the sample. Figure 2.3 presents a schematic diagram of secondary ion formation in SIMS analysis.

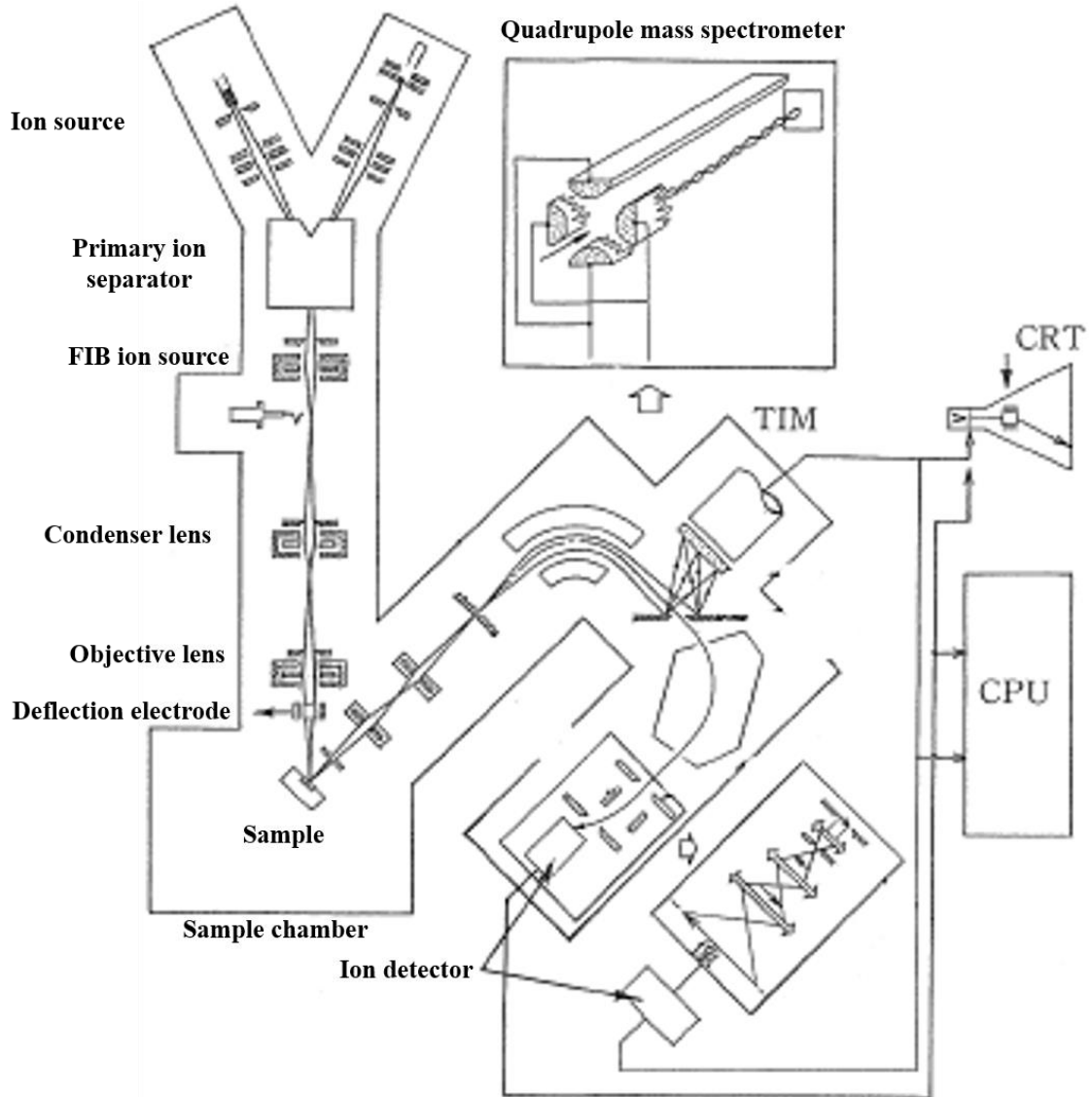


Fig. 2.2. Schematic diagram of the SIMS analytical instrument [74]

The sample is etched by the primary ion beam, and then a secondary ion is released from the sample surface. The signal intensity of the secondary ions depends on the concentration and ionization efficiency of the target element or molecule. If the ionization efficiency is constant, the concentration depth profile is measured by the sputtering rate of the Si wafer using the primary ion and the signal intensity of secondary ions. The ionization efficiency of secondary ions is dependent on the primary ions [78]. Therefore, the primary ion needs to be selected according to the kind of atom analyzed. In general, Cs^+ is used for the analysis of atoms that easily form negative ions, and O^- and O_2^+ are used for the analysis of metals that easily form positive ions. Cs^+ is used as a primary ion for the analysis of C, H, and O. O_2^+ is used as the primary ion for the analysis of Fe, Ni, and Cu.

This type of SIMS analysis method is called dynamic SIMS analysis. There are two types of mass spectrometry (MS) methods for dynamic SIMS: magnetic and quadrupole. Magnetic MS uses a mass separation method utilizing an electric and magnetic field. The accelerated ions are separated by the difference in the orbit radius depending on the strength of the magnetic and electric field on m/z (m is the mass of the ionized atom, and z is the charge of the ion). The magnetic type is able to measure with high resolution and high sensitivity. Quadrupole MS (QMS) uses four cylindrical electrodes. A high-frequency electric field is formed by applying a DC voltage and an AC voltage to each pair of electrodes. Mass separation is performed by the difference in the m/z that can pass through this high-frequency electric field. QMS has the advantage of analysis capability near the surface layer and high depth resolution.

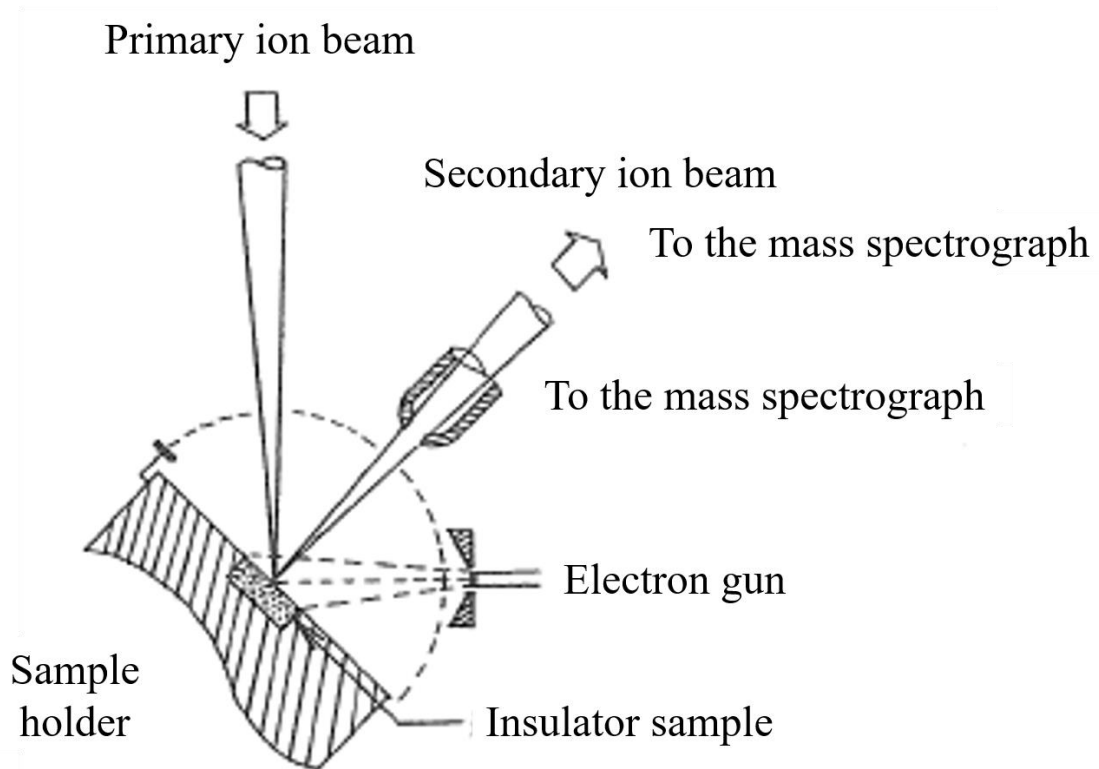


Fig. 2.3. Schematic diagram of secondary ion formation in SIMS analysis [74]

However, this method has the disadvantage of low mass resolution. For example, QMS cannot separate between $^{28}\text{Si}^{2+}$ and $^{14}\text{N}^+$ [81].

In this study, we used QMS for the analysis of the concentration depth profile after ion implantation because of the high resolution near the surface region. For analysis of the Si epitaxial wafer, magnetic MS was used for mass analysis.

2.4 TEM and STEM [82, 83]

We used TEM and STEM to observe crystal defects in the molecular ion implantation region. Figure 2.4 shows the schematic diagram of the TEM equipment. The TEM analysis is an observation method using an electron beam. The TEM instrument consists of an electron source, a condenser lens, an objective lens, an intermediate lens, a projector lens, and the screen. Electrons drawn from the filament are converged by the condenser lens and form the electron beam. After that, the electron beam is irradiated onto the sample. The incident electrons are scattered by the sample and form a transmitted wave and a diffracted wave. These waves form the diffraction pattern on the screen (Figure 2.5(a)). This diffraction pattern indicates the reciprocal space coordinate obtained by the Fourier transform of the real space coordinates of the atom (Figure 2.5(b)). Thus, observation using TEM can allow analysis of the atomic arrangement of the crystal by the inverse Fourier transform of the diffraction pattern. In the case of Si crystal analysis, TEM is used for analyzing crystal defects. For STEM observation, the electron beam diffraction similar to in TEM. STEM observes while scanning a sample using a focused electron beam. Both instruments are used for observation of Si crystal defects.

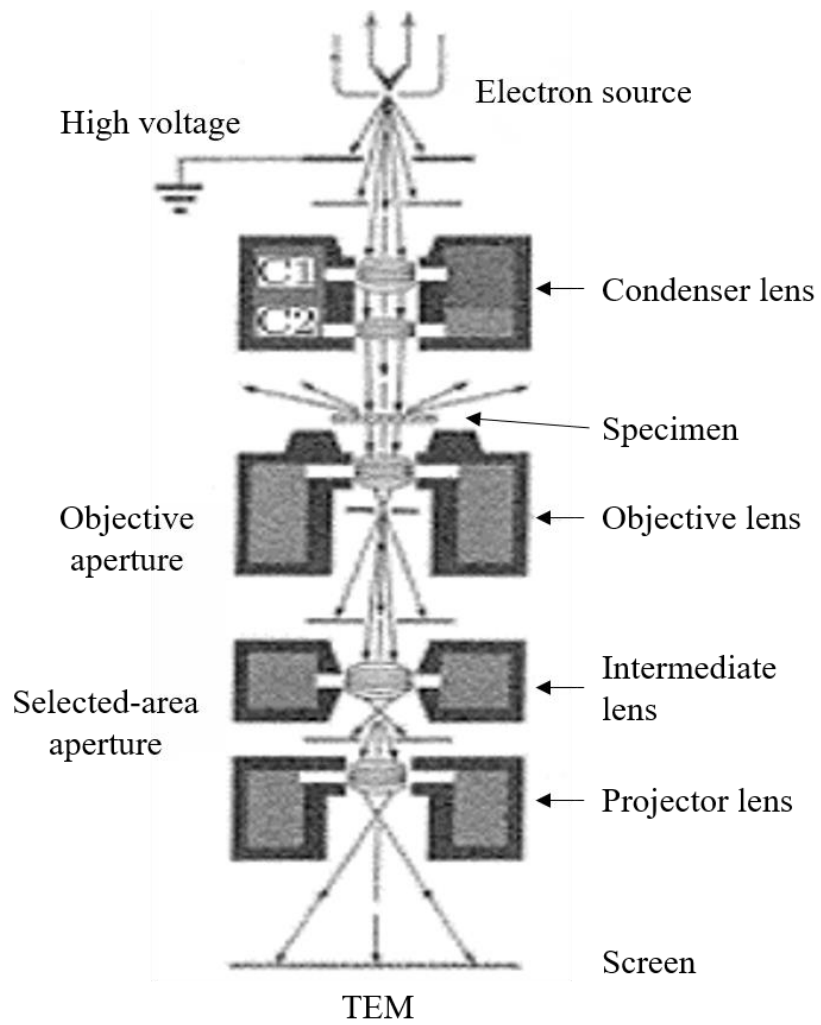


Fig. 2.4. Schematic diagram of TEM analysis [82]

TEM has a feature that it is easy to obtain a diffraction contrast based on the crystal structure, and STEM has a feature that it is easy to obtain contrast depending on the atomic number.

The sample for TEM observations has to be thinner than 100 nm, because the electron beam needs to penetrate the sample. The thickness of the sample for STEM observations can be a little thicker than the sample for TEM. Sample preparation for these methods was performed using two methods. One method uses polishing and ion milling. This method can process samples with low damage. The second method uses a focused ion beam (FIB). A thin sample is taken out directly from the base samples. The process time using FIB is shorter than the polishing and ion milling processes. In this study, the ion milling process was used for high resolution (HR) and the FIB process was used for low resolution (LR) TEM observations.

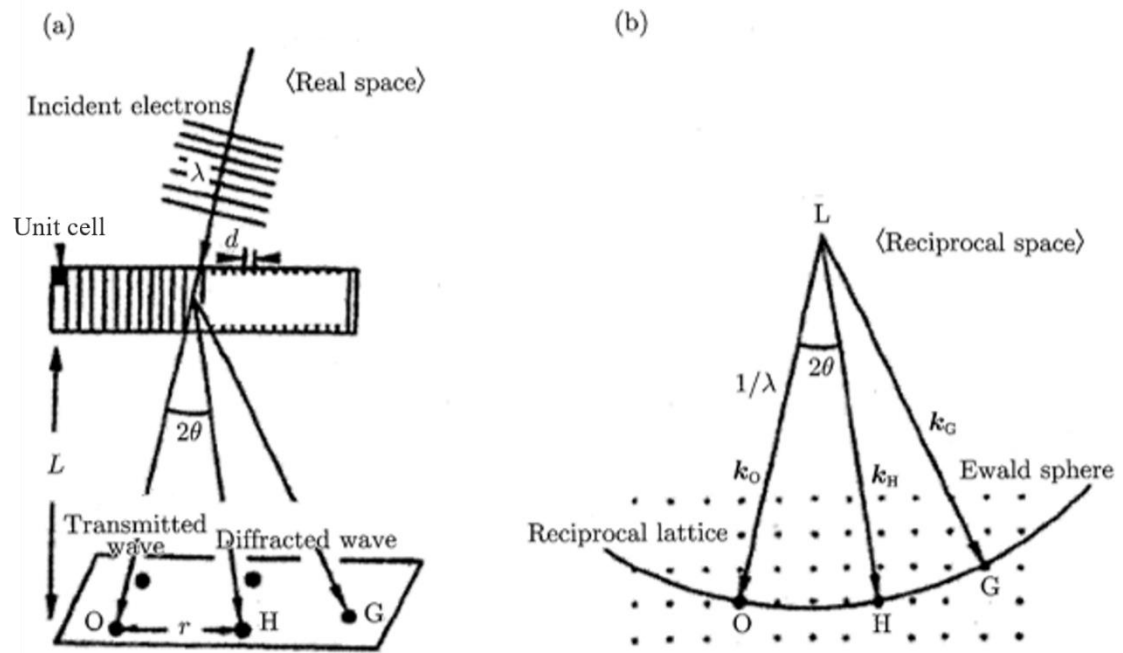


Fig. 2.5. Imaging principle of TEM analysis [82]

2.5 3D-APT

For 3D-APT we used the LEAP4000XSi instrument (Ametek Cameca) for the analysis of the atomic distribution profile in the CH₃O ion implantation region [84]. The 3D-APT analysis method uses electron field evaporation. The analyzed sample is processed into a needle shape with a tip radius of curvature of about 10 to 100 nm using FIB [85-86]. A steady voltage and a pulse voltage are applied to the sample, and ions desorbed from the tip are detected by a position detector and are reconstructed into a 3D atom distribution. The atom identification is performed by time-of-flight (TOF) MS, which measures and calculates the m/z dependence on the time to reach the detector.

In conventional 3D-APT, field evaporation is performed by a pulse voltage, and therefore, analyzed samples have been limited to conductive materials such as metals [86]. To resolve this issue, laser-assisted APT (L-APT) was developed and enabled analysis of semiconductor and insulator materials [87-89]. Figure 2.6 shows a schematic diagram of L-APT analysis. In L-APT, the electron evaporation is performed under the assistance of pulsed laser irradiation. The mechanism of laser assistance is still under study, but it is considered that the thermal energy induced by laser was the dominant effect of assistance [90, 91]. Furthermore, the special and mass resolution dependence on the wavelength of the laser was reported [92, 93]. From these reports, the resolutions were improved using a short-wavelength laser. In this study, a wavelength of 325 nm was used for the pulsed laser.

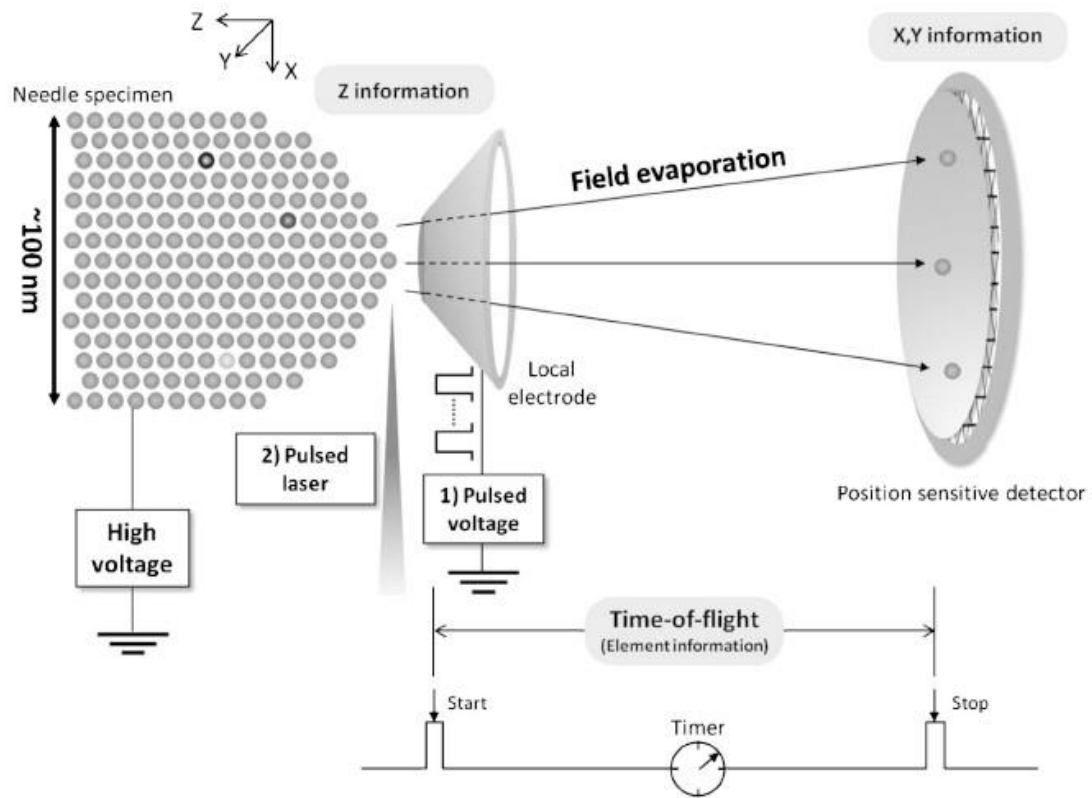


Fig. 2.6. Schematic diagram of 3D-APT analysis [94]

2.6 Conclusion

In this section, we presented the equipment and analysis methods used in this study. To develop the new molecular ion implantation, we used Nissin's CLARIS® ion implanter for cluster ion implantation. To analyze the atomic distribution depth profiles, we used SIMS. TEM was used for the analysis of the defects in the Si crystal. A more detailed distribution of atoms around the defect was analyzed by the 3D-APT method using laser assist. From these analyses, we investigated the characteristics of the new molecular ion implantation.

Chapter. 3

Development of CH₃O ion implantation technology

3.1 Introduction

In processes such as ion implantation or annealing, the CMOS image sensor fabrication induces metallic impurity contamination. This metallic impurity forms deep energy levels in the Si band gaps, which in turn cause degradation of the CMOS image sensors by an increase in white spot defects. Removal of metallic impurities from the device-active region is necessary for highly sensitive CMOS image sensors. Thus, to improve the gettering capability of the proximity gettering technique for the removal of metallic impurities, a Si wafer was required.

As described in Chapter 1, the gettering capability in proximity gettering is expected to be enhanced using multi-element molecular ion implantation technology that implants molecular ions composed of C, H, and O. Molecular ion implantation of this kind has not been reported to date, and the characteristics were also not clear. In particular, to achieve proximity gettering it is important to understand the damage behavior, because the epitaxial growth is performed on the ion-implanted surface. When the damage on the Si surface was high, the single-crystal epitaxial growth could not be performed successfully. Therefore, the purpose of this section is the development and basic study of the characteristics of the multi-element molecular (CH₃O) ion implantation technique.

In our previous work, hydrocarbon molecular ion implantation was performed by CLARIS® using a hydrocarbon molecule such as cyclohexane [54-61]. To develop the

CH₃O ion implantation, we first demonstrated the use of a multi-element molecular ion beam using diethyl ether, which consisted of C, H, and O, as the gas source. We also investigated the damage behavior for CH₃O ion implantation and compared it with implantation using the typical hydrocarbon molecule of C₂H₆. Differences in implantation damage by the molecular species were observed. These results clarify damage formation behavior for molecular ion implantation containing three elements, and are considered to contribute to the development of multi-element molecular ion implantation technology.

3.2 Ionization of diethyl ether using CLARIS®

Mass spectra of the diethyl ether ion source are shown in Figure 3.1, which suggests dependence of the beam current on the mass number. The ions were accelerated to 80 keV. As shown in Figure 3.1, there are groups of mass spectral peaks. The dissociation of the bond between the elements is consistent with the ionization by electron impact [77]. Considering the structure of diethyl ether, the groups of beam current peaks are classified by the number of C and O atoms. For example, it is assumed for the group with a mass of around 43 that these molecular ions consist of two C, one O and several H atoms. As is clear from Figure 3.1, various molecular ions that are assumed to include O, such as mass numbers 31, 45, 59, and 73 were observed. Silverstein *et al.* reported that these molecular ions are particular ions formed by the ionization of diethyl ether using electron impact [95]. They also reported that the ion is stabilized by an unshared electron pair in the O atom. In the case of diethyl ether, because it has a structure in which C₂H₅– groups are bonded to O, the C–C bond in C₂H₅ is easy to dissociate.

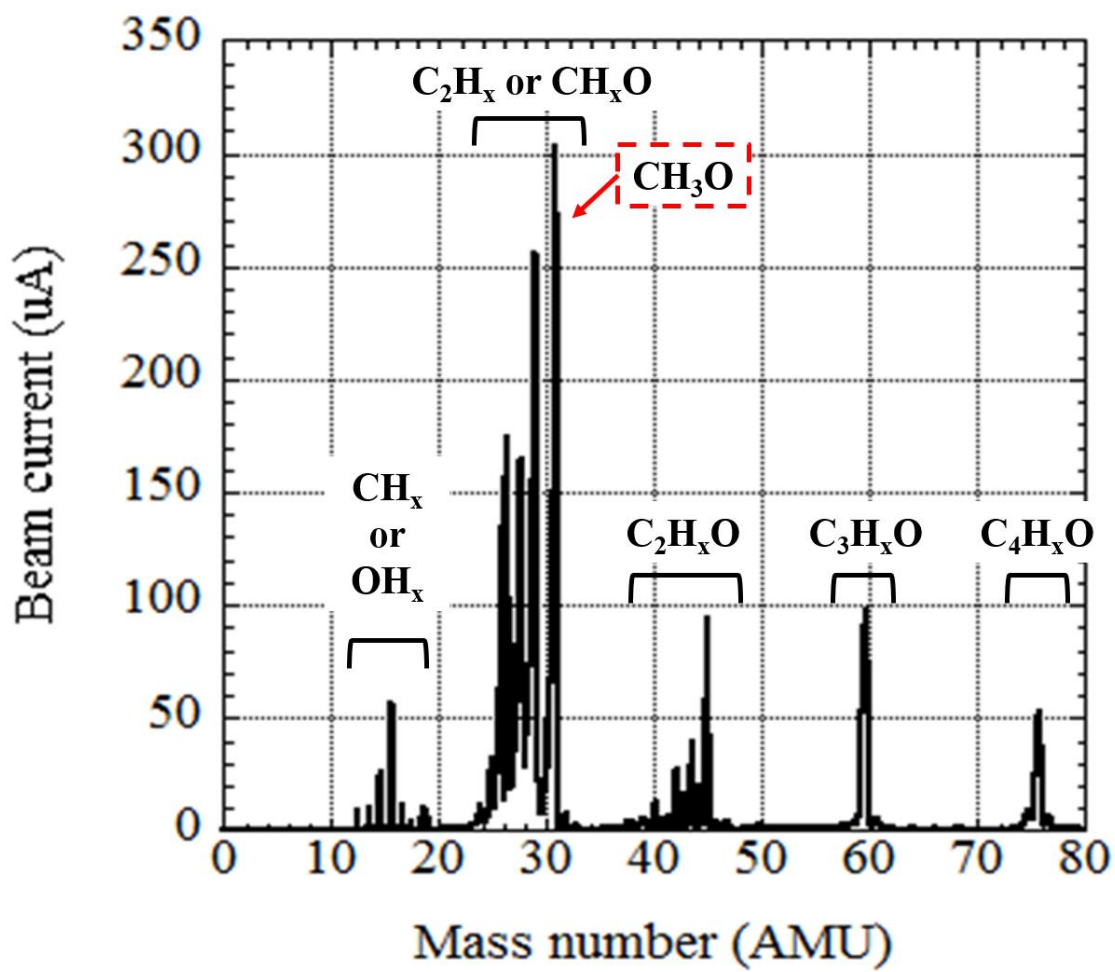


Fig. 3.1. Mass spectrum of molecular ions obtained by ionization of diethyl ether

Furthermore, because O has an unshared electron pair, it is easy to ionize when the C–O bond is dissociated by electron impact [95]. Thus, it is easy to form the molecular ion that includes O by ionization of diethyl ether using the electron impact method. Then, from these various molecular ions containing C and O, we selected the molecular ion with the mass number of 31 to implant for two reasons. The first one is that a single molecular ion can be separated. For example, in the case of a mass number of 29, there are two possibilities: the molecular ions C_2H_5 and CHO. It is not possible to separate between the C_2H_5 and CHO ions using the mass separator of CLARIS®. Therefore, this mass number is not suitable for ion implantation. By contrast, the mass number of 31 ion is assumed to consist only of the CH_3O molecular ion, which is the smallest molecular ion comprising three elements.

The second reason is to avoid excessive surface damage. Ishikawa reported that the acceleration energy of a molecular ion is distributed to the atoms of which the molecular ion is composed [96]. Therefore, increasing the size of the molecular ion means reducing the acceleration energy of the atoms of which it consists. The decrease in acceleration energy translates into increased damage in the Si substrate surface because of the shallower ion implantation region.

As mentioned in Chapter 2, to fabricate the proximity gettering Si epitaxial wafer, an epitaxial layer needs to be formed on the ion-implanted surface. A smaller amount of damage induced by the ion implantation is better for the epitaxial growth process. Considering these reasons, we selected an ion beam of mass number 31 for the proximity gettering technique.

3.3 Distribution depth profiles of C, H, and O after CH₃O ion implantation

Figure 3.2 shows the depth distributions of C, H, and O obtained from SIMS analysis. The implantation was performed with a molecular ion dose of 5.0×10^{14} molecular ions/cm², at an acceleration energy of 80 keV, a beam current of 550 μ A, and tilt and twist angles of 0°. The concentration peak depth of each atom (Figure 3.2) was 132 nm for C, 57 nm for H, and 137 nm for O. These results suggest that the three elements, C, H, and O, were implanted simultaneously. The concentration of implanted C was 5.1×10^{14} atoms/cm², H was 1.8×10^{15} atoms/cm², and O was 4.0×10^{14} atoms/cm². The ratio of the atomic doses of C, H, and O was almost 1:3:1, similar to the ratio in CH₃O. It was determined that the mass of 31 was from the CH₃O ion.

In addition, the O concentration peak is located slightly deeper than that of C, and the H peak is located closest to the surface at 40 nm depth. These differences in the depth of concentration peak are considered to be due to the distribution of the molecular ion implantation energy into individual elements that comprise the molecular ion and to the difference in the energy loss process in the Si crystal. Ishikawa proposed a model of the distribution of the ion implantation energy to the individual elements according to the mass number of the atom [96]. In this model, the accelerated molecular ion was considered to be a lump that moves linearly at constant speed and the binding energy between the elements was ignored, because the binding energy between the elements was in the order of a few eV, whereas the acceleration energy was in the order of tens of keV.

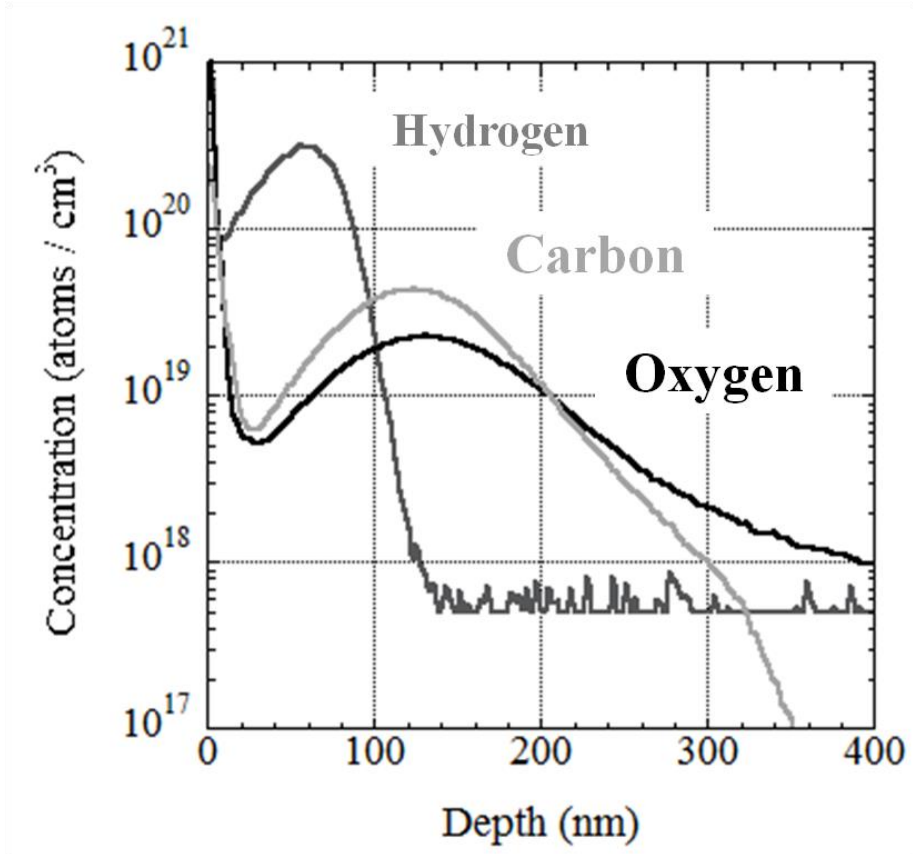


Fig. 3.2. SIMS depth distribution of C, H, and O after CH₃O ion implantation

Typically, when a molecular ion strikes a Si wafer, the molecular ion implantation energy is distributed to the individual atoms. These implantation energies are calculated as

$$E_i = M_i / M \times E, \quad (1)$$

where E is the implantation energy of a molecular ion, E_i is the implantation energy of each atom comprising the ion, M is the mass number of the molecular ion, and M_i is the mass number of each element.

Table I shows the implantation energies of individual elements in implantation of the CH_3O molecular ion at 80 keV, calculated by Eq. (1). According to Table I, the implantation energy of O is higher than that of C. On the other hand, the implantation energy of H is extremely low compared with C and O. Using the implantation energy calculated as shown in Table I, the difference of R_p is considered from the viewpoint of nuclear stopping power. The normalized energy ε is represented by the following equation.

$$\varepsilon = \frac{a_{TF} M_2}{Z_1 Z_2 e^2 (M_1 + M_2)} E$$

Where, the a_{TF} is the Thomas-Fermi radius, M_1 is the mass number of ion, M_2 is the mass number of target atom, Z_1 is atomic number of ion, Z_2 is the atomic number of target atom, e is the elementary charge, and E is the implantation energy. According this equation, the ε of carbon is 2.98, oxygen is 2.71, and hydrogen is 2.05. The dependence of nuclear stopping cross section is shown in Fig. 3.3 [97]. As shown in Fig. 3.3, the nuclear stopping cross section is the highest in the hydrogen. This result suggests that the nuclear stopping energy is the highest in hydrogen compare with carbon and oxygen. It is considered that this difference of nuclear stopping cross section is the reason of the difference of R_p in CH_3O ion-implantation.

Ishikawa *et al.* calculated the correlation between the standardized projection range and the standardized mass number in molecular ion implantation [96]. They reported that the projection range (R_p) in molecular ion implantation can be calculated as

$$R_p[\text{nm}] = \frac{1.1 \times 10^{25}}{N [\text{cm}^{-3}]} \frac{M_1 + M_2}{3M_1 + M_2} \frac{(Z_1^{2/3} + Z_2^{2/3})^{1/2}}{Z_1 Z_2} E[\text{keV}], \quad (2)$$

where R_p is the depth of the projection range peak, and N is the atomic density of the target object. In the case of the Si wafer, N can be considered to be $5.0 \times 10^{22} \text{ cm}^{-3}$. E is the ion implantation energy, M_1 is the mass number of the atoms comprising the molecular ion, and M_2 is the mass number of the target atoms. In the case of the Si wafer, it can be assumed that M_2 is 28, the mass number of Si^{28} ; Z_1 is the atomic number of the each atoms of which the molecular ion consists. Z_2 is the atomic number of the target atoms. In the case of the Si wafer, Z_2 can be assumed to be 14, the atomic number of Si. Substituting the ion implantation energy, M_1 , and Z_1 of each element, the R_p of C was 147 nm, O was 153, and H was 100. The depth of C and O concentration peaks after CH_3O ion implantation was almost the same. By contrast, the R_p of H was formed nearer to the surface compared with that of C and O. As shown in Table I, the ion implantation energy of H was much lower than that of C and O, because the mass number of H is much lower than that of C and O. And those of C and O were at almost the same depth.

TABLE I. Distribution of implantation energies in CH_3O implantation calculated by Eq. (1)

<i>Molecular ion</i>	<i>Mass number</i>	<i>Molecular ion implantation energy (keV)</i>	<i>C implantation energy (keV)</i>	<i>H implantation energy (keV)</i>	<i>O implantation energy (keV)</i>
CH₃O	31.0	80.0	31.0	2.6	41.3

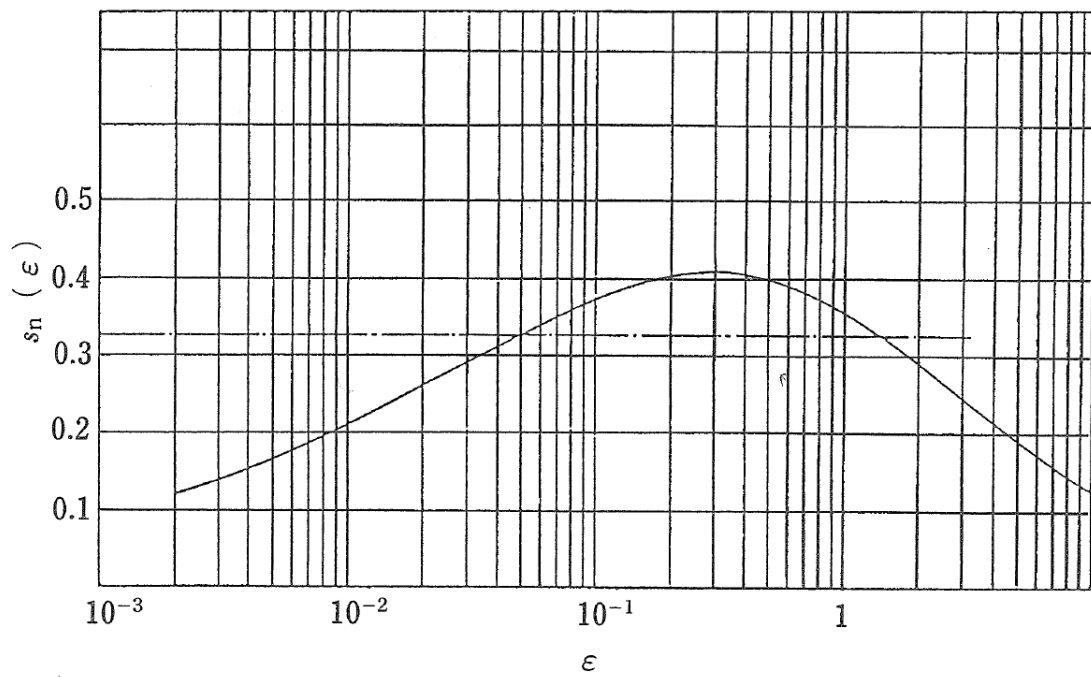


Fig. 3.3. ϵ dependence of nuclear stopping cross section [97].

3.4 Dependence of amorphous formation on CH₃O ion dose

Figure 3.4 shows a cross-sectional image of a Si wafer after CH₃O ion implantation analyzed using TEM. The CH₃O ion dose was $5.0 \times 10^{14} \sim 2.0 \times 10^{15}$ ions/cm². An amorphous layer was observed at a dose of 1.0 to 2.0×10^{15} ions/cm². The amorphous layer is formed within the Si wafer and this layer is expanded to the surface of the wafer due to the dose increase. This trend is similar to that of molecular ion implantation, but not to that of the Ar cluster ion beams.

The Ar cluster ion consists of thousands of Ar atoms. However, the CH₃O ion consists of only five atoms. Therefore, the size effect in the ion implantation damage is assumed to be small. Furthermore, the ion implantation energy distribution to individual elements is higher in the CH₃O than in the Ar cluster ion. Aoki *et al.* reported the implantation energy of the Ar atom in an Ar cluster ion to be only a few eV [62]. By contrast, as shown in Table I, the implantation energy of an individual atom in CH₃O ion implantation was higher than 1 keV. In particular, the implantation energy of C and O was higher than 20 keV. As a result, the trend of CH₃O ion implantation damage is similar to that of monomer ion implantation.

These results suggest that the damage peak of CH₃O ion implantation is formed within the Si wafer bulk and the damage of surface is smaller. This damage trend is also similar to that observed in hydrocarbon molecular ion implantation. In our previous report, the epitaxial growth was performed on the hydrocarbon molecular ion-implanted surface [58, 98]. Thus, it was expected that epitaxial growth can be successfully performed on the CH₃O ion-implanted surface.

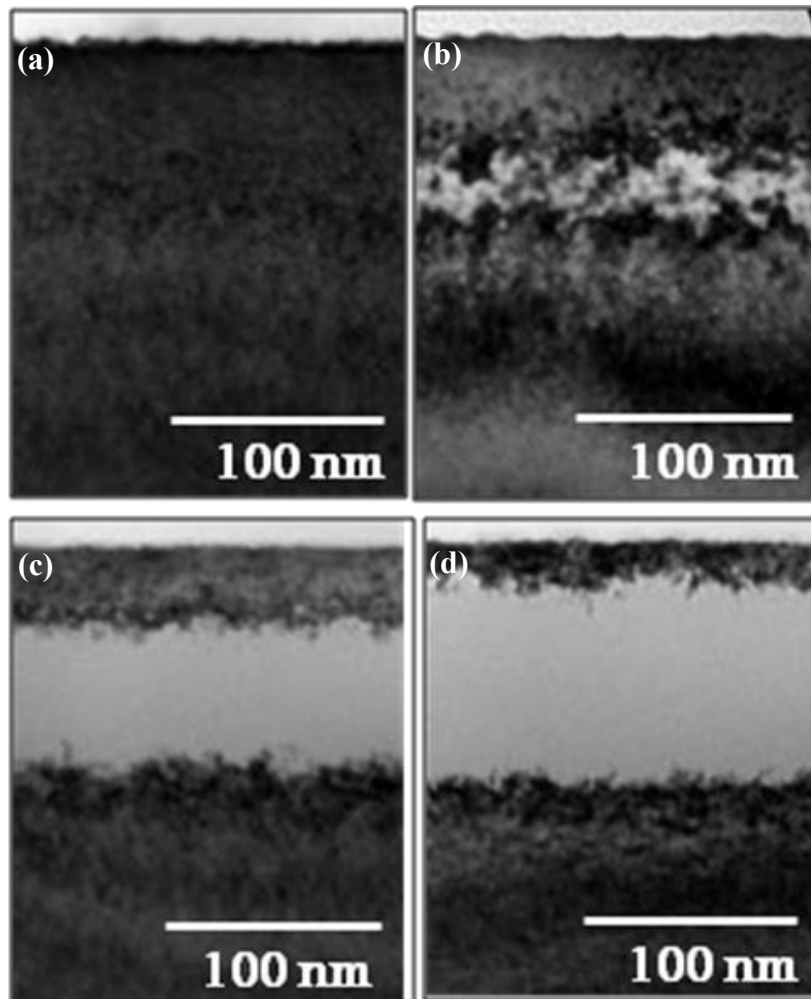


Fig. 3.4. Cross-sectional image of CH₃O molecular ion-implanted region.

The molecular ion dose [molecular ions/cm²] was

(a) 5.0×10^{14} , (b) 1.0×10^{15} , (c) 1.5×10^{15} , and (d) 2.0×10^{15} .

3.5 Comparison of the ion implantation damage between CH₃O and C₂H₃

In Section 3.4, we discussed the trend of CH₃O ion implantation damage as being similar to that of the hydrocarbon molecular ion implantation. However, the CH₃O ion contains a new species, O, which is heavier than C. The effect of O on the ion implantation damage was not clear. In this section, we conduct a comparison of the ion implantation damage between CH₃O and C₂H₃; the latter gas is the conventional hydrocarbon molecular ion.

Figure 3.5 shows a cross-sectional image of a Si wafer after CH₃O and C₂H₃ ion implantation under the same conditions, an ion dose of 1.0×10^{15} ions/cm², acceleration energy of 80 keV, beam current of 550 μ A, and tilt and twist of 0°. According to Figure 3.5, an amorphous layer was observed only for CH₃O molecular ion implantation. This result suggests that the damage to the Si wafer is higher under molecular ion implantation with CH₃O than with C₂H₃. In the CH₃O ion, one C atom from the C₂H₃ ion is replaced by O. It is found that the presence of O enhances the formation of the amorphous layer.

To consider this phenomenon, we conducted a simulation on the amount of damage in the molecular ion-implanted region by using technology computer-aided design (TCAD) with the Sentaurus simulation process from Synopsys Inc. [99]. Figure 3.6 shows the damage distribution (red line), C distribution (black line), H distribution (green line), and O distribution (blue line) of CH₃O (solid line) and C₂H₃ (dotted line) with implantation at the molecular ion dose of 5.0×10^{14} ions/cm².

The damage determined from the TCAD simulation defines the vacancy concentration formed by implantation. In CH₃O ion implantation, the damage peak was higher than in C₂H₃ ion implantation, but this trend was the same as that observed with TEM imaging.

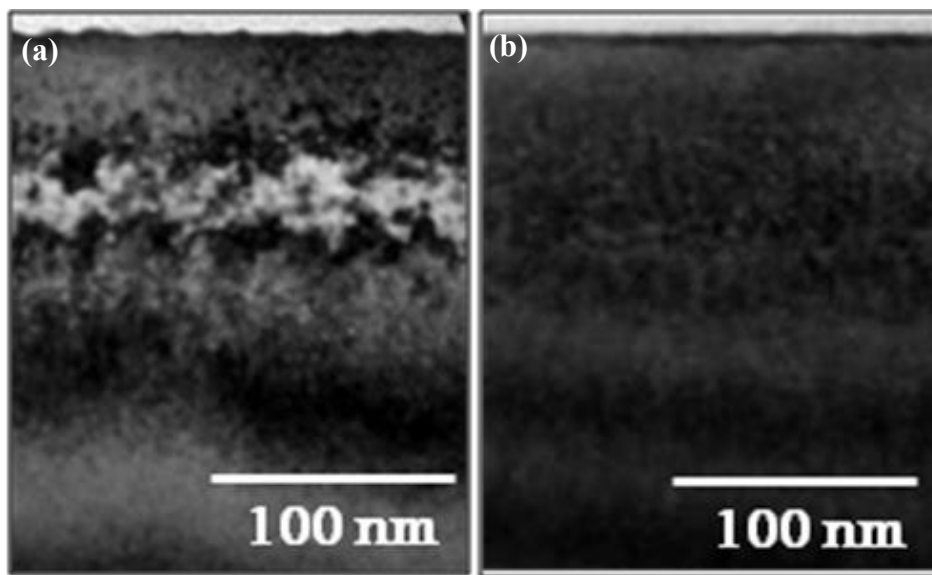


Fig. 3.5. Cross-sectional TEM image of the molecular ion-implanted region with a dose of 1×10^{15} [molecular ions/cm²]

(a) CH₃O-ion-implanted wafer, (b) C₂H₃-ion-implanted wafer

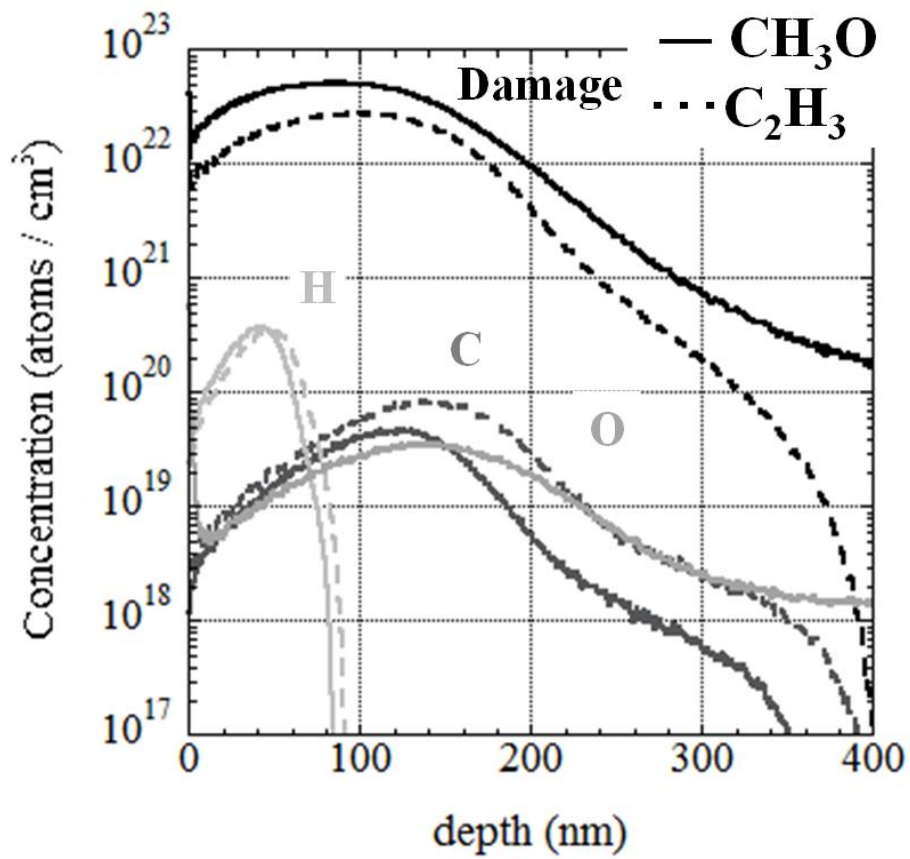


Fig. 3.6. Distribution depth profiles of C, H, and O and damage calculated using TCAD simulation

It is considered that the ion implantation damage induced by H was much smaller than that induced by C and O, because the mass number and the ion implantation energy were much lower. It is considered that the damage increase has occurred as follows. First, the damage increased with the increase in the mass number due to the change of one element from C¹² to O¹⁶. In the region that is deeper than that of the damage concentration peak, damage concentration profile is according to the concentration profile of implanted oxygen. Thus, the trajectory of implanted O highly contributes to implantation damage.

Second, the damage concentration peak increases by the shift in the R_p of C to nearer the surface. Table II shows the implantation energy of each of the elements in CH₃O and C₂H₃ ion implantation calculated at 80 keV using Eq. (1). The ion implantation energy of C in CH₃O is lower than that in C₂H₃. The decrease in C implantation energy caused the C implantation depth to be shallower, and the C concentration peak to become high. The increase in the peak concentration introduced by ion implantation is assumed to cause an increase in the peak concentration of the ion implantation damage. By combination of these two factors, it was assumed that the damage peak concentration formed per one C atom increased by the change of C₂H₃ ion to CH₃O.

From these results, there is a high possibility of forming a vacancy and an O complex by heat treatment. Thus, we expected that CH₃O molecular ion implantation can enhance the gettering capability for metallic impurities.

TABLE II. Distribution of implantation energies in CH₃O and C₂H₃ ions calculated using Eq. (1)

<i>Molecular ion</i>	<i>Mass number</i>	<i>Molecular ion implantation energy (keV)</i>	<i>C implantation energy (keV)</i>	<i>H implantation energy (keV)</i>	<i>O implantation energy (keV)</i>
CH ₃ O	31.0	80.0	31.0	2.6	41.3
C ₂ H ₃	27.0	80.0	35.6	3.0	

3.6 Conclusion

In this chapter, a new CH₃O molecular ion implantation technique was developed and its basic characteristics described. The results are summarized as follows:

1. A molecular ion beam consisting of three elements, namely C, H, and O was obtained using diethyl ether as the ion source.
2. From the SIMS measurement of the concentration depth profiles of the three elements in the molecular ion implantation region, it was found that the molecular ion with mass number of 31 was the CH₃O ion. From this result, we confirmed the development of the CH₃O ion implantation technique.
3. From the cross-sectional TEM image, it was found that an amorphous layer is formed within the Si substrate due to the CH₃O molecular ion implantation. This result suggests that the trend of CH₃O molecular ion implantation damage behavior was the same as that of C₂H₃ molecular ion implantation. This means that epitaxial growth after CH₃O molecular ion implantation is very likely.
4. From the cross-sectional TEM image, it was found that the damage from CH₃O molecular ion implantation was higher than that from C₂H₃. We considered that this increase in damage is caused by the increase in the mass number of the molecular ion. This tendency was also observed in the calculation results of the TCAD simulator.

Chapter. 4

Defect formation behavior in CH₃O ion implantation region

4.1 Introduction

The removal of metallic impurity contamination from the device active region is important for an advanced CMOS image sensor. As described in Chapter 1, the gettering technique is a powerful method of removing contamination by metallic impurities introduced by device fabrication processes such as heat treatment or ion implantation.

One of the origins of the gettering capability is the defect formed in the bulk of the Si substrate. In the case of IG, O precipitation acts as the gettering sink [25, 28]. In the case of EG, the scratches formed on the back side of the Si substrate by the mechanical damage also act as gettering sinks [33, 100, 101].

In the case of proximity gettering using ion implantation, the origin of the gettering capability is also the defect introduced by ion implantation. Kuroi *et al.* reported that the crystal defects in the ion-implanted region after annealing act as gettering sinks [50]. Kurita *et al.* reported that the defects formed by aggregation of C that are introduced by the hydrocarbon molecular ion implantation act as gettering sinks [54-58].

The morphology of this defect is not a crystal defect such as stacking fault or dislocation loop. However, they reported that this types of defects act as a strong gettering sink. Clarifying the morphology and formation behavior of the defect introduced by ion implantation is important for understanding the origin of the gettering capability.

In particular, the Si epitaxial growth undergoes an annealing process at 1100 °C. It is important to understand the defect formation behavior with this annealing condition.

In this chapter, we investigate the defect morphology and formation behavior of CH₃O ion implantation defects. First, we present the morphology of the defect formed in the CH₃O ion implantation region. We then investigate the defect morphology and diffusion behavior of the ion-implanted elements after the Si epitaxial growth process. Finally, we investigate the density of the CH₃O ion implantation defect dependence on the ramping-up rate. We believe that these experimental results contribute toward understanding the origin of the gettering capability of the CH₃O ion implantation region and strengthen the gettering capability.

4.2 Experimental methods

4.2.1 Si epitaxial growth: Sample preparation

The samples were 12-inch n-type (100) P-doped Czochlarski (CZ) Si single-crystal wafers that were implanted with CH₃O (multi-element molecular) ions and (hydrocarbon molecular) C₂H₃ ions at room temperature. Figure 4.1 shows the sample fabrication flow of the CH₃O and C₂H₃ ion-implanted Si epitaxial wafers. The fabrication flow of these wafers includes two processes: molecular ion implantation and Si epitaxial growth (Figure 4.1). As indicated in Chapter 2, the ion implantations with CH₃O and C₂H₃ were performed using Nissin's ion implanter CLARIS[®] [77] at an implantation energy of 80 keV/ion. The implantation dose of the CH₃O ion was 5.0×10^{14} – 2.0×10^{15} ions/cm², which is converted to a C dose of 5.0×10^{14} – 2.0×10^{15} C atoms/cm². The implantation dose of the C₂H₃ ion was 3.75×10^{14} – 5.0×10^{14} ions/cm² converted to a C dose of 7.5×10^{14} – 1.0×10^{15} C atoms/cm², similar to the C dose for the CH₃O ion.

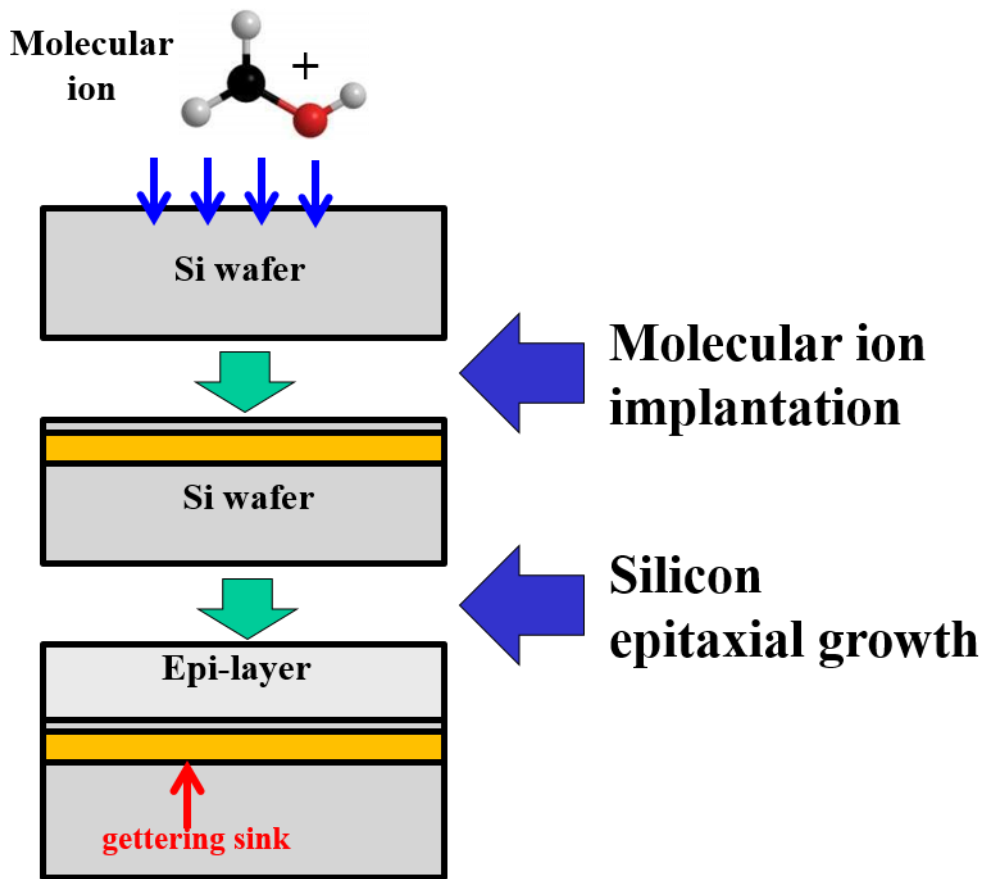


Fig. 4.1. Sample preparation flow of molecular ion-implanted Si epitaxial wafer

The ion beam current was the same for both gases, 550 μA . After CH_3O ion and C_2H_3 ion implantation, Si epitaxial growth was performed using chemical vapor deposition (CVD). The epitaxial layer thickness was 9.0 μm .

4.2.2 Rapid thermal annealing (RTA) sample preparation

Ion implanted samples were annealed by RTA in N_2 ambient using AccuThermo Aw610 of HiSOL, Inc. The temperature during RTA was measured using a pyrometer. Figure 4.2 shows a typical heat treatment profile. To accurately control the ramping-up rate, heating was carried out from 500 $^\circ\text{C}$ for 10 s (because the pyrometer of AccuThermo Aw610 cannot measure temperature below 450 $^\circ\text{C}$). With this setting, an accurate ramping-up rate can be obtained from 500 to 1100 $^\circ\text{C}$. The ramping-up rates were 4, 8, 15, and 60 $^\circ\text{C}/\text{s}$.

4.2.3 Analysis method

As mentioned in Chapter 2, STEM and TEM analyses were carried out to obtain images of the defects in the (multi-element molecular) ion-implanted region after RTA. The distributions of implanted C and O were analyzed by SIMS. The concentration depth profile of interstitials induced by CH_3O ion implantation was calculated using the Sentaurus TCAD process simulator from Synopsys [99].

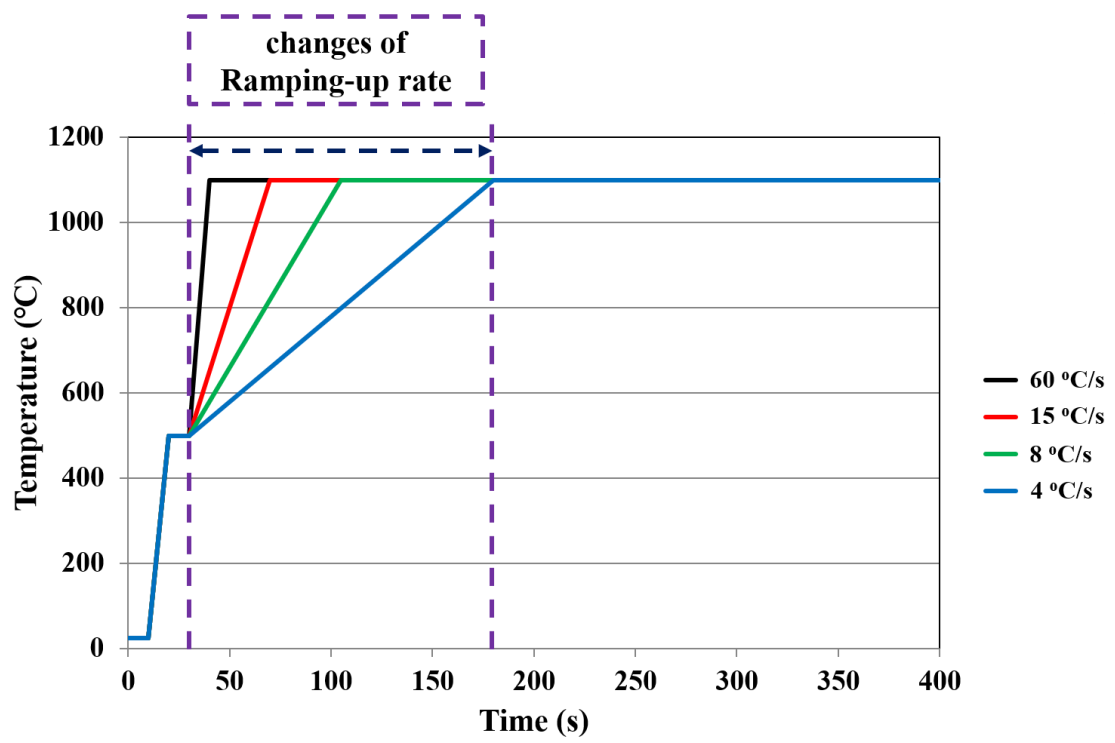


Fig. 4.2. Profiles of various RTA processes at different rates, as shown

4.3 Characteristics of the CH₃O ion implantation region after Si epitaxial growth

The Si epitaxial process involves a high-temperature heat treatment of 1100 °C or higher for several minutes. The defects that act as gettering sinks were formed during this process. Therefore, understanding the defect formation and diffusion behavior in the CH₃O ion implantation region during the Si epitaxial process is important for understanding the origin of gettering sinks. In this section, we discuss the morphology of the defects in the CH₃O ion implantation region formed after Si epitaxial growth and examine the differences in the defect formation behavior between C₂H₃ and CH₃O ion implantation regions.

4.3.1 Defect observation in the CH₃O ion implantation region

Figure 4.3 shows cross-sectional TEM images of the CH₃O ion implantation region. The implantation energy was 80 keV, and the dose was 5.0×10^{14} – 2.0×10^{15} C atoms/cm². In these images, defects of about 50 nm were observed in the CH₃O ion implantation region in the samples with a dose above 7.5×10^{14} – 2.0×10^{15} C atoms/cm². No such large defects were observed at a dose of 5.0×10^{14} C atoms/cm², suggesting that formation of defects of about 50 nm is dose dependent. This tendency is thought to be related to ion implantation damage. In the Chapter, 3.3, we reported that the critical dose of CH₃O ion implantation is approximately 1.0×10^{15} ions/cm². Thus, it is considered that the excessive damage induced into the Si crystal by CH₃O ion implantation is one of the causes of the occurrence of secondary defects.

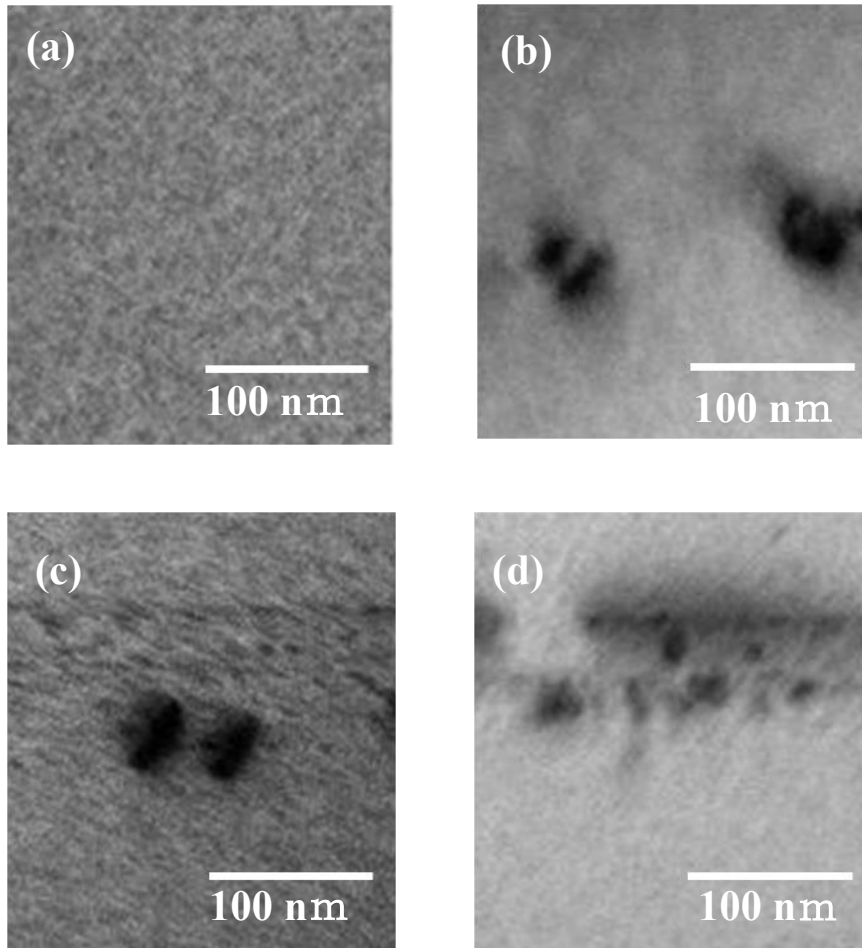


Fig. 4.3. Cross-sectional TEM images of CH₃O ion implantation region.

The implantation doses were (a) 5.0×10^{14} , (b) 7.5×10^{14} , (c) 1.0×10^{15} , and (d) 2.0×10^{15} ions/cm². The implantation energy was 80 keV

Figure 4.4 shows a high-resolution cross-sectional TEM image of the CH₃O ion implantation region. The implantation energy was 80 keV/ion, and the dose was 1.0×10^{15} C atoms/cm². The interface of the epitaxial layer and the Si substrate is indicated by the black dashed line in Figure 4.4. The implantation region of the CH₃O ion was observed at a depth of approximately 120 nm from the interface between the epitaxial layer and the Si substrate. Two types of defects (5 and 50 nm defects) were observed in the CH₃O ion implantation region. The 5 nm defect is observed at a depth of approximately 80 nm and the 50 nm defect is observed at a depth of approximately 160 nm from the interface between the epitaxial layer and the Si substrate. Therefore, the 50 nm defect region is deeper than the 5 nm defect formation region in the CH₃O-implanted region.

A similar type of 5 nm defect was observed in the hydrocarbon molecular ion implantation region [54-58]. The formation of this defect is due to the C implantation and is act as gettering sink. The CH₃O ion contains a C atom. Hence, the 5 nm defect in the CH₃O ion implantation region is considered to be due to the C implantation and also affects the gettering sink. From this result, it is assumed that the CH₃O ion implantation region has at least the same degree of gettering capability as the hydrocarbon molecular ion implantation region. The 50 nm defect is a new type of defect. Okuyama *et al.* reported on defect formation in the hydrocarbon molecular ion implantation region [98]. In the sample with a high hydrocarbon molecular ion dose, 40 nm defects formed in the ion-implanted region after epitaxial growth. This defect is due to recrystallization of the amorphous region formed by ion implantation and is located on the surface side of the hydrocarbon molecular-implanted region. However, for CH₃O ion implantation, the 50 nm defects are located on the back side of the implanted region (Figure 4.4).

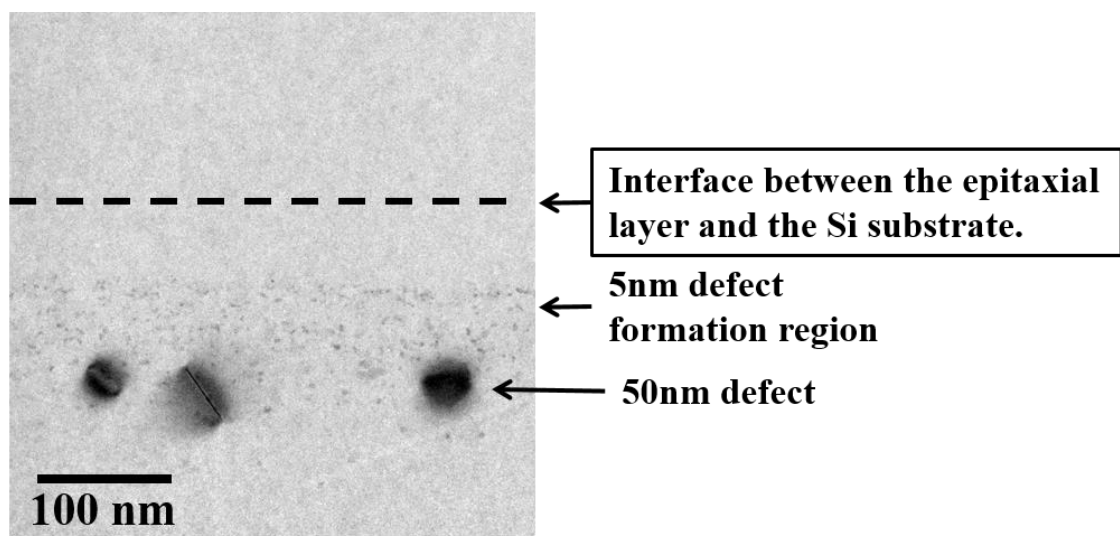


Fig. 4.4. Clear resolution cross-sectional TEM image of the CH₃O ion implantation region.

The ion dose was 1.0×10^{15} ions/cm²

Thus, it is considered that the 50 nm defects are peculiar to the CH₃O ion implantation region. The formation of defects of 50 nm is considered to be the effect of adding O to the ions. To analyze the origin of the 50 nm defects, we conducted high-resolution TEM observations and fast Fourier transform (FFT) analysis.

Figure 4.5 (a) shows a high-resolution cross-sectional TEM image of 50 nm defects in the CH₃O ion implantation region. The 50 nm defect has a linear shape in the direction of Si {111} (Figure 4.4(a)). For a detailed analysis of this type of defect, we took an FFT pattern on the edge of a defect. An enlarged TEM image of a defect edge and the FFT pattern are shown in Figure 4.5 (b).

Figure 4.5 (c) was extracted from the FFT pattern by extracting only the Si {111} direction component. From Figure 4.5 (c), the 50 nm defects are the stacking faults inserted with one atomic layer in the Si {111} direction. There seems to be two types of 50 nm defects, i.e., round and linear in the Si {111} direction, as shown in Figure 4.3. However, the round defects are assumed to be Si {111} stacking faults in the direction perpendicular to the TEM analysis direction. Therefore, it is assumed that the round and linear defects are the same. Thus, the 50 nm defects are considered to be Si {111} stacking fault defects.

Okuyama *et al.* reported defects of near size in the ion-implanted region of hydrocarbon molecular implantation. They reported from the electron diffraction pattern that the 40 nm defects in the hydrocarbon molecular ion implantation region were Si single crystals [98]. From the difference in diffraction patterns, the defect in the CH₃O-implanted region is thought to be different from that in the hydrocarbon molecular implantation region. The 50 nm defect is peculiar to the CH₃O implantation region.

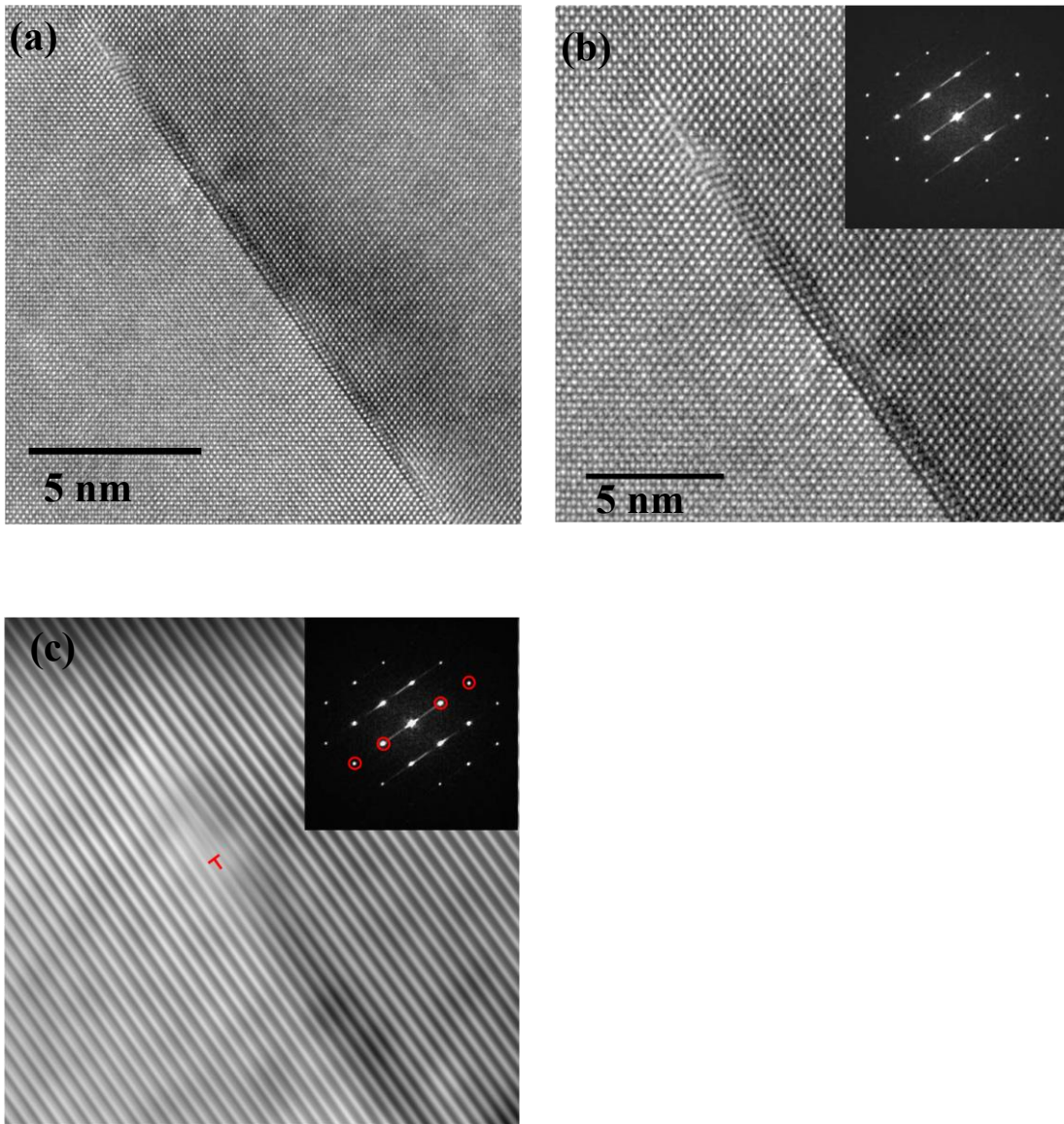


Fig. 4.5. High-resolution cross-sectional TEM image of 50 nm defects in CH₃O ion implantation region. (a) Overall image of the 50 nm defects; (b) expansion image of 50 nm defects; (c) FFT

To consider the origin of the 50 nm defects, we calculated and compared the damage distribution after C₂H₃ and CH₃O implantation by TCAD simulation. Figure 3.5 shows the distribution profiles of C, H, and O and the damage calculated by TCAD simulation. The implanted energy was 80 keV. Both CH₃O and C₂H₃ were implanted at a dose of 5.0×10^{14} ions/cm². The tilt and twist were 0°. The damage concentration was calculated by the Frenkel pair model that defines the interstitial Si (I) and vacancy (V) concentration generated due to the ion implantation. In the high-dose condition, the damage concentration is saturated due to supersaturated generation of I and V. In this situation, it is not possible to compare the damage profiles in CH₃O and C₂H₃. Therefore, it was calculated at a dose of 5.0×10^{14} ions/cm², at which the damage profile of the ion implantation region can be compared. As shown in Figure 3.5, the damage concentration increased for CH₃O ion implantation, even at the same ion dose. In CH₃O, one C atom of C₂H₃ is replaced with O. This result shows that the impact of O on the ion implantation damage is extremely large.

From Figure 3.5, it was found that the damage from CH₃O ion implantation is larger in the region of deeper than a C concentration peak at 160 nm depth as compared with C₂H₃ implantation. The damage profile indicated that there is more formation of I and V damage with implantation with CH₃O than with C₂H₃. Therefore, it is considered that excessive I would remain without recombination with V during heat treatment of the epitaxial growth layer. A previous study reported that excessive I induced by ion implantation forms defects by aggregation, called “end of range” (EOR) defects, during the heat treatment [102-104]. This increase of the concentration of I in the region of deeper than C concentration peak is consistent with the defect of 50 nm is an intrinsic type stacking fault as shown in Figure 4.5. Furthermore, it agrees with the fact that 50 nm

defects are located behind C complex defects as shown in Figure 4.4. Therefore, the origin of 50 nm defects is considered to be aggregates of interstitial Si formed in deep regions by additional O implantation during ion implantation with CH₃O, like the EOR defect.

Kuroi *et al.* reported that the EOR defect acts as a gettering site. It is expected that the 50 nm defect acts as a gettering site [50]. Thus, the gettering capability of the CH₃O ion-implanted region is expected to be higher than that of a hydrocarbon molecular ion-implanted region because of the formation of new defects.

4.3.2 Diffusion behavior of C, O, and H

Figure 4.6 shows the C, H, and O distribution depth profiles of CH₃O ion-implanted Si epitaxial wafers. The implantation energy was 80 keV and the dose was 1.0×10^{15} C atoms/cm². The epitaxial layer thickness was 9 μm. From these results, the CH₃O ion implantation region had concentration peaks of C, H, and O.

The peak concentration of the C impurity in the CH₃O ion-implanted region was higher than 3.3×10^{17} atoms/cm², which is the maximum solid solubility of C in Si single-crystal wafers [105]. This trend was the same as for the hydrocarbon molecular ion-implanted region. Kurita *et al.* reported that a high concentration of C is observed after epitaxial growth in the hydrocarbon molecular ion-implanted region, and an aggregate of C is formed in this region as a gettering sink [54-58]. Therefore, it is speculated that the CH₃O ion implantation region has almost the same characteristics as the hydrocarbon molecular ion implantation region. In the CH₃O ion-implanted region, C and O had approximately the same concentration peaks. Such a trend was not observed in the hydrocarbon molecular ion implantation region.

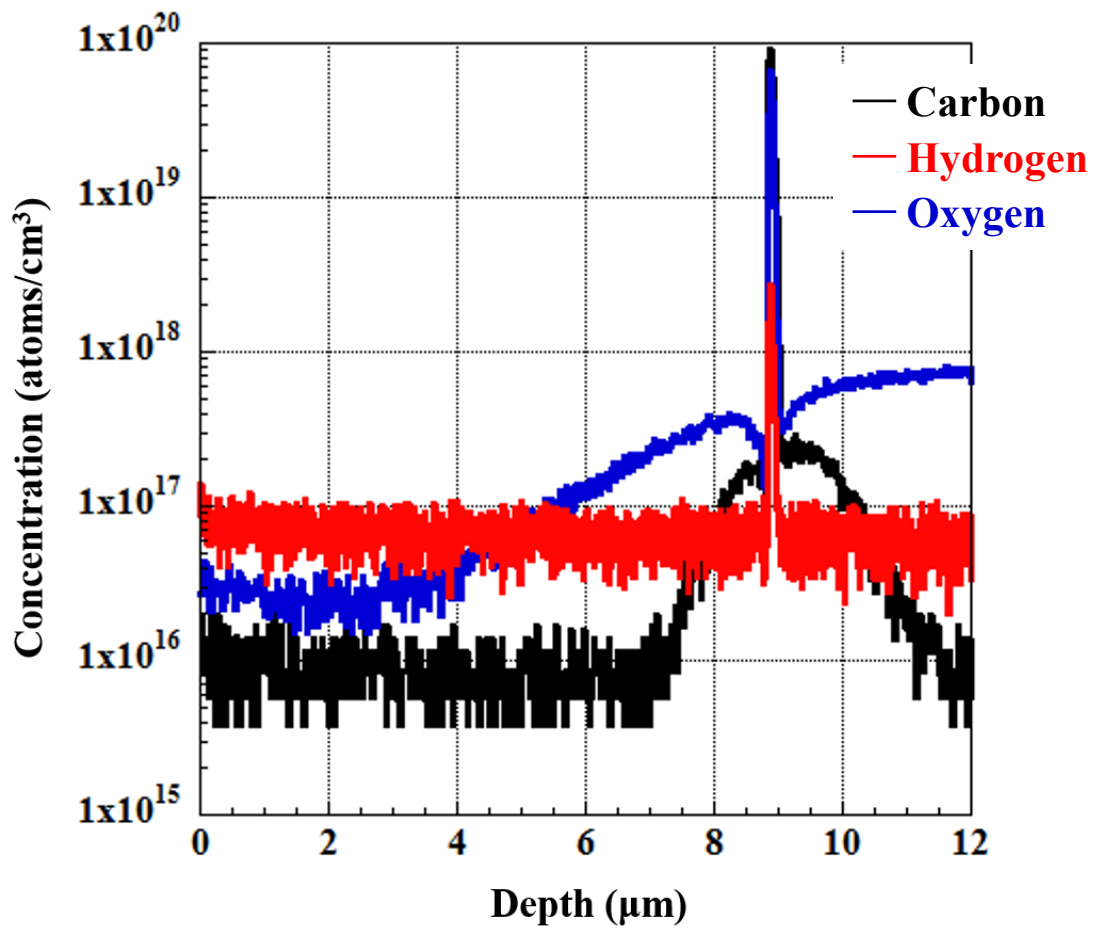


Fig. 4.6. Depth distribution profiles of C, H, and O in CH₃O ion-implanted epitaxial wafer obtained using SIMS. The blue line is C, the black line is H, and the red line is O

Figure 4.7 shows the distribution depth profiles of O in CH₃O and C₂H₃ ion-implanted Si epitaxial wafers. The C dose was the same in both CH₃O and C₂H₃ ion implantations, i.e., 1.0×10^{15} C atoms/cm². As shown in Figure 4.7, the O peak concentration of the CH₃O ion-implanted sample was 6.5×10^{19} atoms/cm³. The O peak concentration of the C₂H₃ ion-implanted sample was 3.1×10^{18} atoms/cm³. The O peak concentration of the CH₃O ion-implanted sample was up to more than 10 times higher than that of the C₂H₃ ion-implanted sample. These results suggest that particular complexes possibly formed in the CH₃O ion implantation region, which are not formed in the hydrocarbon molecular ion implantation region. By contrast, the O concentration of the CH₃O ion-implanted sample in the epitaxial layer was up to approximately two times higher than that in the C₂H₃ ion-implanted sample. These results suggest that almost all the O implanted by CH₃O ion is fixed in the CH₃O ion implantation region. The detailed mechanism of the implanted O behavior is not clear. However, it is assumed that there are two mechanisms.

First, O is gettered in the C implantation region. Kurita *et al.* reported that the hydrocarbon molecular ion implantation region can getter the O impurity [58]. A hydrocarbon molecular ion contains C and H, and the CH₃O ion also contains C and H. Thus, it is assumed that there is a possibility that O is gettered in the CH₃O ion-implanted region.

Second, the VO complex forms in the CH₃O ion implantation region. Using DFT calculations, Shirasawa *et al.* calculated the possibility of VO complex formation in the hydrocarbon molecular ion implantation region [71-73]. As shown in Figure 4.5, the CH₃O ion implantation forms a high concentration of vacancies by collisions with the Si crystal. Furthermore, a high O concentration remained in the CH₃O ion implantation region after epitaxial growth (Figure 4.7).

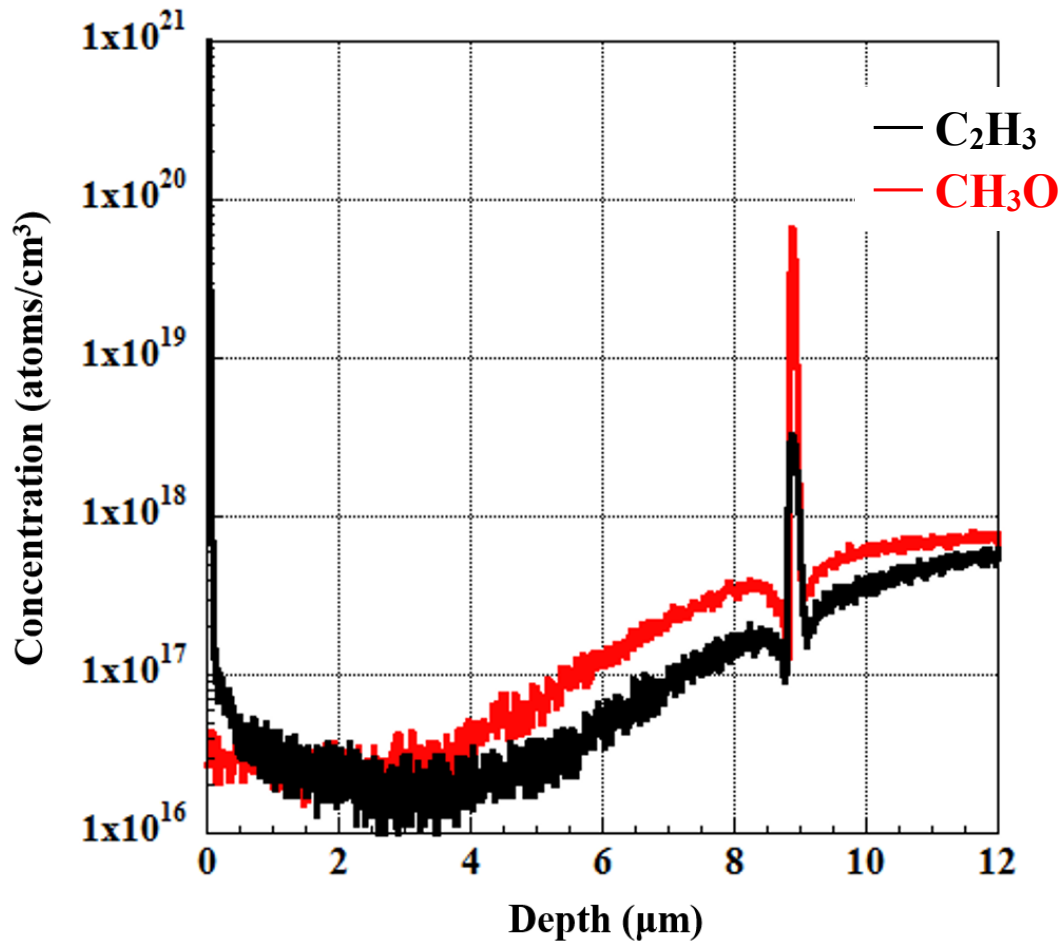


Fig. 4.7. O distribution profiles of CH_3O and C_2H_3 ion-implanted Si epitaxial wafers. The red line is the CH_3O ion-implanted Si epitaxial wafer, and the black line is the C_2H_3 ion-implanted one. The epitaxial thickness was 9 μm

Thus, the CH₃O ion implantation region is expected to have a high concentration of VO complexes. Shirasawa *et al.* also reported that VO complexes in the ion implantation region possibly act as a gettering site for metallic impurities. Thus, if VO complexes were formed in the CH₃O ion implantation region, this is expected to enhance the gettering capability of metallic impurities.

4.4 EOR defect formation behavior in the CH₃O ion-implanted region

In the previous section, we found that a particular defect was formed in the CH₃O ion implantation region. As described in Chapter 1, defects can act as gettering sites. Therefore, because of the existence of particular defects, it is expected that the gettering capability of the CH₃O ion-implanted region would be higher than the gettering capability of the hydrocarbon molecular ion-implanted region because of the additional defect formation. However, for advanced CMOS image sensors, the gettering capability needs to be further enhanced. To enhance the gettering capability, it is important to understand defect formation behavior. In this section, we will report on the defect formation behavior in the CH₃O ion implantation region using RTA. In Section 4.4.1, we discuss the morphology of the defect formed in the CH₃O ion implantation region. We discuss the types of defects formed in the CH₃O ion implantation region. In Section 4.4.2, we discuss the dependence of defect density on the ramping-up rate in the CH₃O ion implantation region. In Section 4.4.3, we discuss the mechanisms of the formation and disassemble behavior of the CH₃O ion implantation defect.

4.4.1 Defect type in CH₃O ion-implanted region

Figure 4.8 shows the TEM images of the CH₃O ion-implanted region after (a) CH₃O ion implantation at a dose of 1.0×10^{15} ions/cm² and (b) RTA at a ramping-up rate of 15 °C/s, a temperature of 1100 °C, and an annealing time of 300 s. Figure 4.9 shows the damage profile calculated by TCAD simulation after CH₃O ion implantation at an energy of 80 keV and a dose of 1.0×10^{15} ions/cm².

As shown in Figure 4.8(a), an amorphous region was formed at a depth of approximately 80 nm from the Si surface. By contrast, after RTA for 300 s, defects were formed at 1100 °C at a depth of 120 nm from the Si surface, as shown in Figure 4.8(b). TCAD calculation results showed that the damage concentration peak is observed at a depth of approximately 80 nm from the Si surface (Figure 4.9). The damage in the TCAD calculation represents interstitial Si and vacancies generated by CH₃O ion implantation. The damage concentration peak in the TCAD calculation results is at the same depth as the amorphous layer, and so the damage profile calculated by TCAD is in good agreement with the TEM findings. Furthermore, from the TCAD calculation results, the characteristics of the profile of the CH₃O ion implantation-generated damage, i.e., the damage concentration peak and the decay with increasing depth, are similar to those of monomer ion implantation.

Jones and Rozgonyi classified monomer ion implantation defects into five types on the basis of their crystallinity after ion implantation, the positional relationship among defects formed after heat treatment, and the behavior of implanted elements after heat treatment [102]. They classified the defects formed behind the a/c interface into type II under ion implantation conditions in which an amorphous layer is formed.

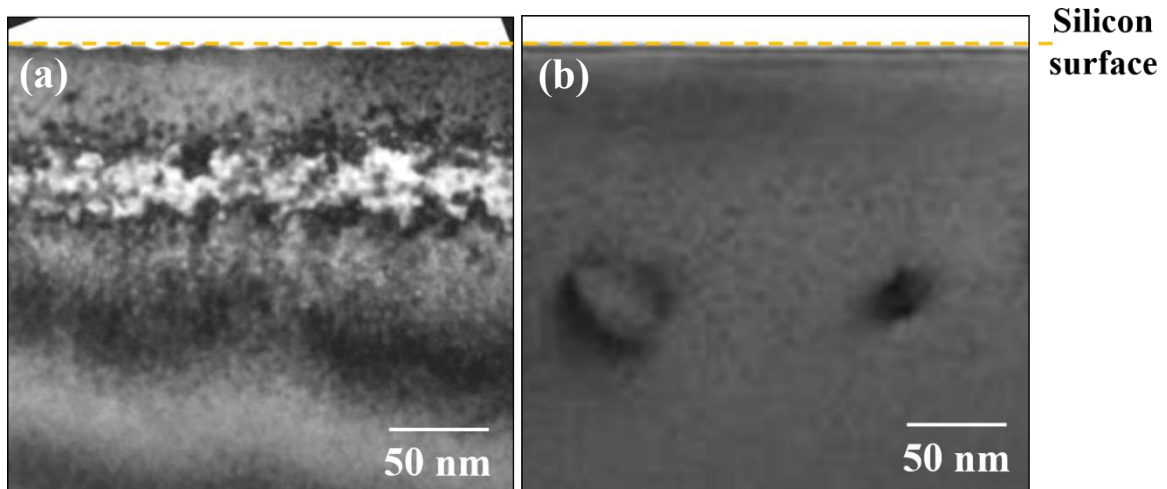


Fig. 4.8. Cross-sectional TEM images of CH₃O ion-implanted region after (a) CH₃O ion implantation and (b) RTA

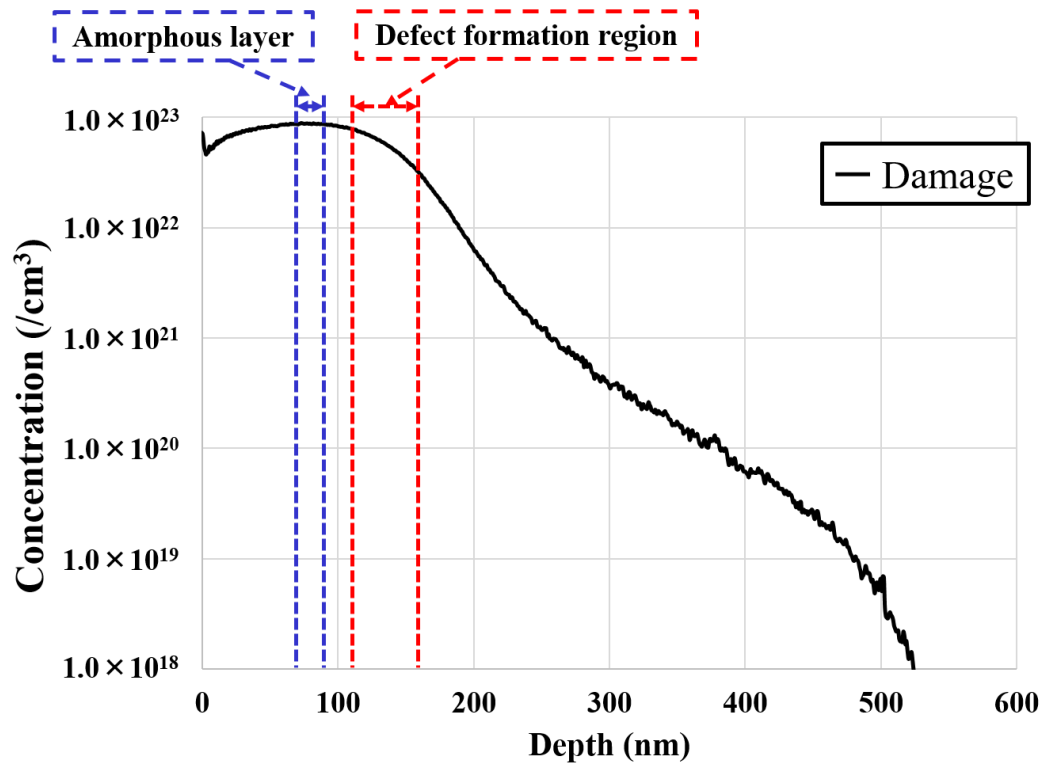


Fig. 4.9. Profiles of damage concentration generated by CH₃O ion implantation calculated by TCAD simulation

They also reported that a type II defect is formed by aggregation of interstitial Si introduced by ion implantation. A comparison of TEM images after CH₃O ion implantation and RTA (see Figure 4.8(a, b)), shows that the depth of defects in the CH₃O ion-implanted region is deeper than that in the amorphous layer. This defect morphology is in good agreement with the type II defect reported by Jones and Rozgonyi [102]. Thus, the defects introduced by CH₃O ion implantation are considered to be type II and are formed by aggregation of interstitial Si.

The same types of defects were observed in the CH₃O ion implantation region after the epitaxial growth process, as discussed in Section 4.3.1. This result suggests that the defect formation behavior in RTA is the same as that in the epitaxial growth process. Therefore, it is considered that the defect behavior during the Si epitaxial process can be demonstrated using RTA.

4.4.2 Dependence of the density of CH₃O ion implantation defects on the ramping-up rate

In the previous section, we demonstrated that the morphology of CH₃O ion implantation generated defects after RTA. We also confirmed that these defects are of type II and correspond to those after epitaxial growth. Ito *et al.* reported that the formation behavior of an EOR defect which is type II depends on the heat treatment temperature and changes with temperature between 500 and 1100 °C [75]. Thus, the formation behavior of the defect in the CH₃O ion implantation region is assumed to depend on the heat treatment condition. Furthermore, the ramping-up process in the epitaxial growth process has a heat treatment at 500–1100 °C. Therefore, it is assumed that the defect formation behavior in the CH₃O ion implantation region changes by the change in

ramping-up rate. In this section, we show the effect of the ramping-up rate during RTA at 1100 °C on the formation of CH₃O ion-implanted defects.

Figure 4.10 shows TEM images of a CH₃O ion-implanted Si wafer after 300 s RTA at 1100 °C. The ramping-up rate was in the range of 4–60 °C/s between 500 and 1100 °C. The density of the CH₃O ion-implanted defect after RTA changed with the change in ramping-up rate (Figure 4.10). Figure 4.11 shows the density of CH₃O ion-implanted defects after RTA. The density of CH₃O ion-implanted defects is lowest at 4 °C/s and highest at 15 °C/s (Figure 4.11). These results suggest that the density of CH₃O ion implantation defects is dependent on the ramping-up rate.

Tamura *et al.* reported that the EOR defects introduced by monomer ion implantation form during annealing at temperatures between 600 and 1000 °C [106]. They also reported that EOR defects are repaired after annealing at 1100 °C. The ramping up during annealing at temperatures between 600 and 1000 °C, in which range EOR defects are formed, is longest at 4 °C/s. It is assumed that the defect density is the highest at the ramping-up rate of 4 °C/s. However, the density of the defects after 1100 °C for 300 s was highest at 15 °C/s. These results suggested that the density of the defects is affected by the defect behavior during both the ramping up and the 1100 °C annealing.

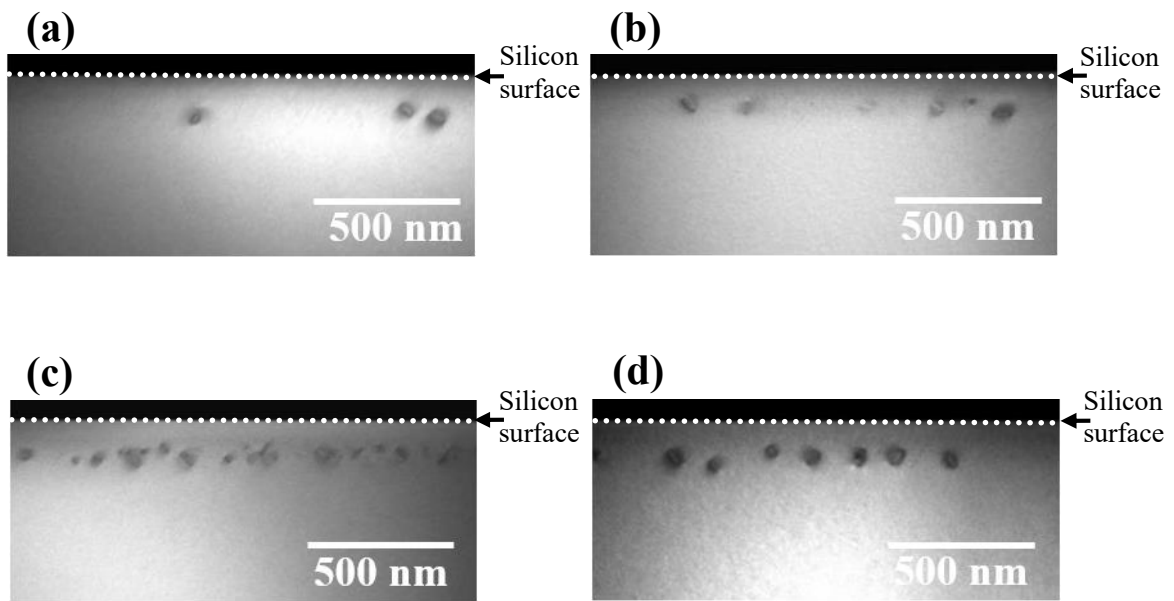


Fig. 4.10. TEM images of CH₃O ion-implanted region after RTA at 1100 °C for 300 s, at ramping-up rates of (a) 4, (b) 8, (c) 15, (d) 60 °C/s

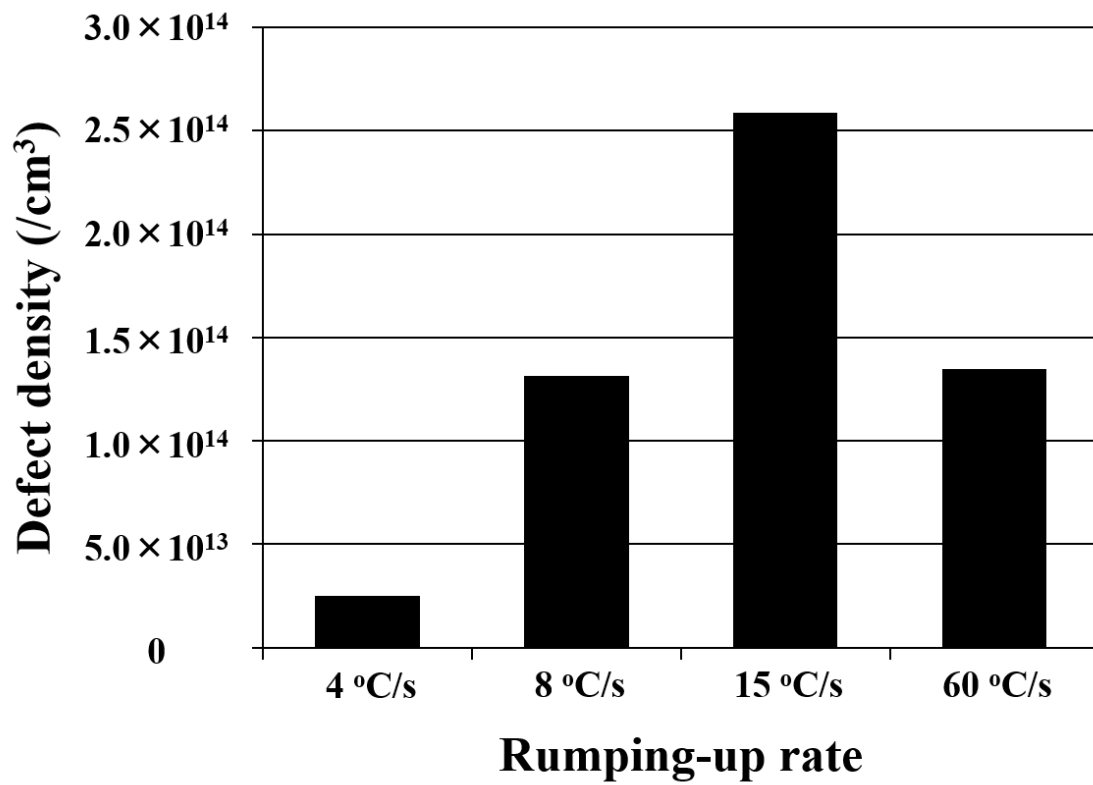


Fig. 4.11. Dependence of density of CH₃O ion-implanted defects on rumping-up rate

Figure 4.12 shows the dependence of the defect density on the 1100 °C annealing time and ramping-up rate. The defect density decreased with increasing annealing time at 1100 °C (Figure 4.12). This finding indicates that the CH₃O ion-implanted defects get corrected during 1100 °C annealing. Additionally, it is observed that the defect density for CH₃O ion implantation is dependent on the ramping-up rate. In the case of 0 s annealing at 1100 °C, the defect density is almost the same at all ramping-up rates. On the other hand, the defect density of the 15 °C/s sample was higher than that in the other samples after longer annealing. This finding suggests that the defects in the sample that was ramped up at 15 °C/s are corrected with more difficulty than those at other ramping-up rates. Increasing the defect density may increase the gettering capability. Therefore, it is assumed that the 15 °C/s ramping-up rate can increase the gettering capability of the CH₃O ion-implanted Si epitaxial wafer.

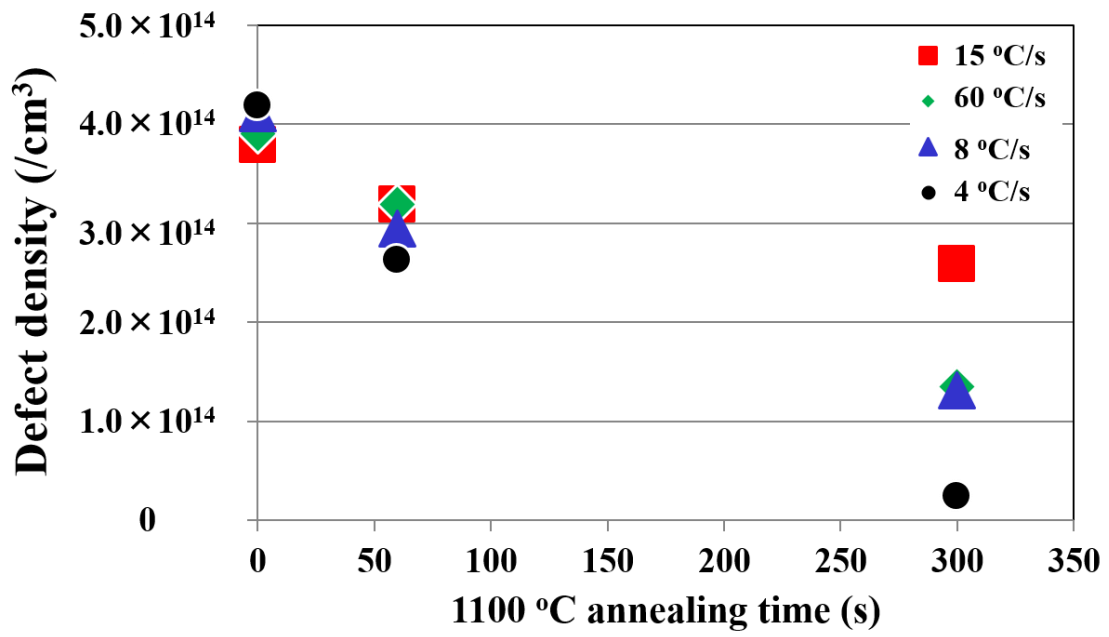


Fig. 4.12. Dependence of density of CH₃O ion-implanted defects on ramping-up rate and annealing time

4.4.3 Mechanism underlying defect density dependence on ramping-up rate

In previous sections, we showed that the ramping-up rate contributes to the change in the density of CH₃O ion-implanted defects. In particular, the ramping-up rate of 15 °C/s provided the highest density of CH₃O ion-implanted defects remaining after 1100 °C annealing. This finding suggests that the ramping-up rate should not be too low or too high to obtain a sufficiently high density of CH₃O ion implantation defects remaining. Then, why is it difficult to repair the defects formed at 15 °C/s? It is considered that this defect behavior was determined by the defect repair behavior during 1100 °C annealing and the defect formation behavior during ramping up.

First, we consider the repair mechanism of CH₃O ion implantation defects during 1100 °C annealing. Tamura *et al.* examined the behavior of defects introduced by monomer ion implantation and found that the defects were corrected by annealing at 1100 °C and Bonafos reported that the EOR defects are corrected owing to the release of interstitial Si [106]. However, the CH₃O ion implantation defects remained after 1100 °C annealing (Figure 4.3(b)). Thus, the defect repair behavior during annealing at 1100 °C cannot be explained by only the interstitial Si behavior. Figure 4.13(a, b) respectively shows the SIMS depth profiles of C and O after 300 s at annealing at temperatures of 800, 900, 1000, and 1100 °C. The ramping-up rate was set at 60 °C/s to avoid the effect of the defect formation behavior during ramping up. After 800 °C annealing, only one concentration peak is observed. By contrast, two peaks are observed at other annealing temperatures. In our previous studies of Chapter. 3, these two peaks corresponded to C-related and ion-implanted defects. These results suggest that the C and O implanted during CH₃O ion implantation are fixed around the CH₃O ion implantation defects.

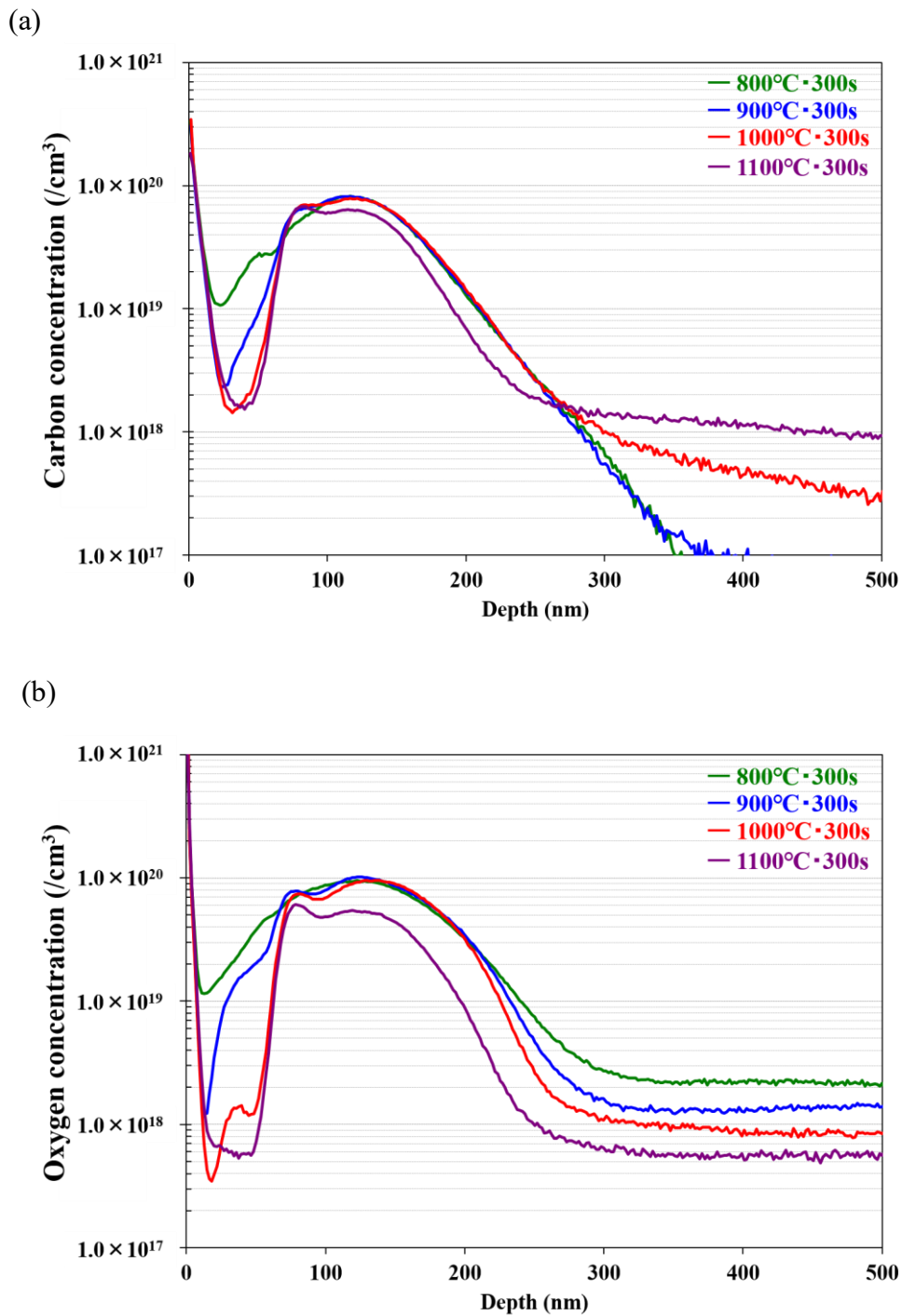


Fig. 4.13. SIMS analysis results of CH_3O ion-implanted region after RTA treatment.

Depth profiles of (a) C and (b) O concentrations

It was previously reported that the EOR defects introduced by monomer ion implantation are stabilized by the O in the Si wafer [107-109]. The CH₃O ion implantation defects are stabilized by the high concentrations of aggregated C and O around ion-implanted defects. Therefore, the interaction between the CH₃O ion implantation defect and C and O is considered to be important for the CH₃O ion implantation defect remaining after 1100 °C annealing.

The mechanism of the repair behavior during annealing at 1100 °C is considered to be as follows. Initially, the CH₃O ion implantation defects are destabilized by the release of C and O from the defects during annealing at 1100 °C. Then, interstitial Si is released from CH₃O ion implantation defects. As a result, the defects get repaired during the annealing at 1100 °C. Therefore, C and O pinning are important for the stabilization of the CH₃O ion implantation defects during annealing at 1100 °C.

Second, we consider the dependence of the defect density formed during RTA on the ramping-up rate. In a previous report on the behavior of defects introduced by monomer ion implantation, the defect morphology changed with annealing temperature. Ito *et al.* reported that the size of EOR defects introduced by monomer ion implantation increases by annealing between 800 and 1000 °C [75]. Thus, the morphology of CH₃O ion implantation defects is considered to be dependent on the annealing temperature (see Figure 4.14 for the 300 s annealing at 800, 900, 1000, and 1100 °C). The ramping-up rate was set at 60 °C/s to avoid the effect of the defect formation behavior during the ramping up. As shown in Figure 4.14, defects larger than 50 nm were observed at annealing temperatures above 900 °C. On the other hand, no defects of this size were observed after annealing at 800 °C. Furthermore, the defect density after 1100 °C annealing was lower than after annealing at 900 and 1000 °C.

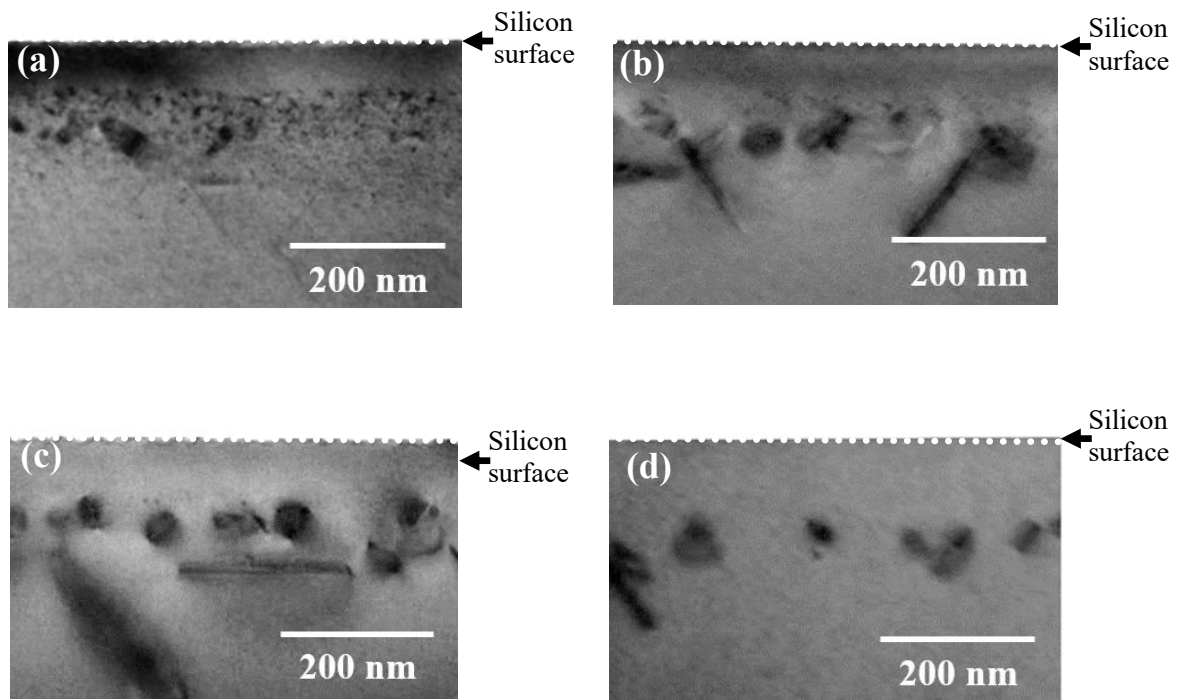


Fig. 4.14. TEM images of CH₃O ion-implanted region after RTA for 300 s at (a) 800, (b) 900, (c) 1000, and (d) 1100 °C

These results suggest that the CH₃O ion implantation defects were formed by annealing at temperatures of about 900 °C, and it is assumed that the duration of annealing at these temperatures is important for increasing the CH₃O ion implantation defect density.

Then, we demonstrated the defect behavior during RTA at 900 °C for various annealing durations. Figure 4.15 shows the TEM images of the CH₃O ion-implanted Si wafer at 900 °C annealed for 0, 60, and 300 s at a ramping-up rate of 60 °C/s. As shown in Figure 4.15, the defects appear to have extended with increasing annealed duration. As Bonafos *et al.* reported, the EOR defects become larger in a short time of a few seconds because of the absorbance of interstitial Si during annealing at around 900 °C [104]. In the case of CH₃O ion implantation, the defects are considered to also absorb the interstitial Si and extend during the annealing at 900 °C. Furthermore, C and O at high concentrations aggregated around the CH₃O ion implantation defects formed during annealing at 900 °C (Figure 4.13). Therefore, it is considered important that annealing at around 900 °C should proceed for some time to form stable CH₃O ion implantation defects.

On the basis of the above mechanisms, we consider the question “Why were the CH₃O ion implantation defects formed at 15 °C/s rarely repaired during annealing at 1100 °C. Figure 4.16(a–c) shows schematic diagrams of CH₃O ion implantation defects immediately after ramping up.

In the case of ramping up at a low rate of 4 °C/s, it is considered that the defects were easily repaired during the annealing at 1100 °C. The interstitial Si concentration around the defects is assumed to decrease through diffusion during annealing at temperatures below 900 °C. Interstitial Si is not sufficiently absorbed during annealing at temperatures higher than 900 °C.

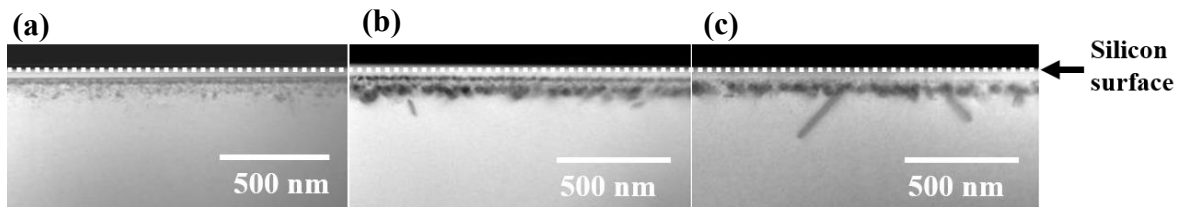


Fig. 4.15. TEM images of CH₃O ion-implanted region after 900 °C RTA for annealing duration of (a) 0, (b) 60, and (c) 300 s

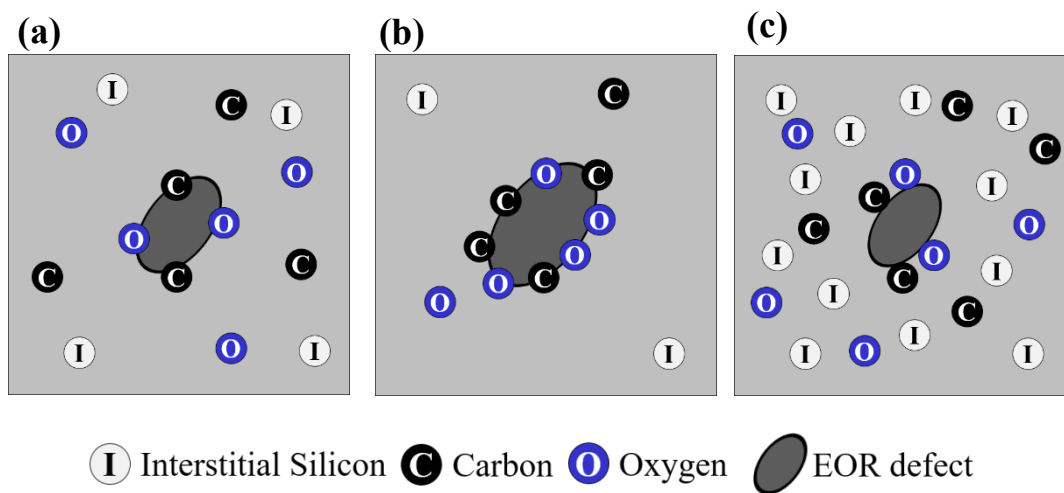


Fig. 4.16. Schematic images of formation behavior of CH₃O ion implantation defects at ramping-up rates of (a) 4, (b) 15, and (c) 60 °C/s

As a result, the CH₃O ion implantation defects are easily repaired during annealing at 1100 °C. Furthermore, in the case of ramping up at a rate of 4 °C/s, the duration of annealing at over 1000 °C is longer than that at a ramping-up rate of 15 °C/s. Because the CH₃O ion implantation defects were repaired by annealing above 1000 °C with the release of C and O (Figures 4.13 and 4.14), the CH₃O ion implantation defects are assumed to easily repair at 4 °C/s. This is also considered to be a factor causing the decrease in the density of CH₃O ion implantation defects.

In the case of ramping up at a high rate of 60 °C/s, it is considered that no defects were formed with sufficient size and density during the ramping-up process. The shorter the ramping-up process, the shorter the time for defect formation during annealing. Thus, it is considered that interstitial Si, C, and O were not aggregated during the ramping-up process (Figure 4.16(c)). CH₃O ion implantation defects are considered to easily repair during annealing at 1100 °C because they are not sufficiently stabilized by C and O. As a result, the density of CH₃O ion implantation defects was decreased by ramping up at 60 °C/s.

It is considered that interstitial Si, C, and O aggregated sufficiently during ramping up at 15 °C/s (in contrast to 60 °C/s) (Figure 4.16(b, c)). On the other hand, more interstitial Si is considered to remain in the case of ramping at 15 °C/s than that at 4 °C/s (Figure 4.16(b, c)). Furthermore, the duration of annealing at over 1000 °C and 15 °C/s was shorter than that at 4 °C/s. On the basis of these findings, it is considered that the defects formed at 15 °C/s can hardly repair themselves during annealing at 1100 °C, resulting in a higher density of the defects at other rates.

We assumed that the dependence of the density of CH₃O ion implantation defects on the ramping-up rate is determined by the formation behavior of EOR defects, namely

aggregation of interstitial Si and the interaction of C and O with the EOR defects. Regarding the remaining CH₃O ion implantation defects after annealing at 1100 °C, we found three important factors related to the ramping-up process. First, the duration of annealing at a temperature below 800 °C should be as short as possible. Second, the duration of annealing at a temperature of about 900 °C should be as long as possible. Finally, annealing at a temperature above 1000 °C should also be as short as possible.

4.5 Conclusions

In this section, we investigated the defect morphology and formation behavior in the CH₃O ion-implanted region, and we also investigated the diffusion behavior of C and O, which are introduced by CH₃O ion implantation. The results are summarized as follows:

1. There are two types of defects in the CH₃O ion-implanted region, namely a C-related defect and an EOR defect after heat treatment.
2. The C-related defect is considered to be formed by C aggregation, which is introduced by the CH₃O ion implantation. This is observed by TEM scans as 5 nm dot-shaped defects. This defect is also found in the hydrocarbon molecular ion-implanted region.
3. The EOR defect is never observed in the hydrocarbon molecular ion-implanted region. Therefore, this type of defect is considered to be peculiar to CH₃O ion implantation. We concluded that this defect is formed by the increase in ion implantation damage due to addition of O on the molecular ion.
4. The O concentration in the CH₃O ion-implanted region is higher than that of the hydrocarbon molecular ion implantation region after the epitaxial growth process. This result suggests that implanted O in the CH₃O ion remains in the implantation region during the epitaxial growth process. It is expected to increase the gettering capability by forming

new gettering sinks such as a VO complex. From these results, the proximity gettering technique using CH₃O ion implantation is expected to enhance the gettering capability in the ion implantation region.

5. The morphology of CH₃O ion implantation defects depends on the annealing temperature and the density of defects depends on the ramping-up rate. We found that the CH₃O ion implantation defect is formed only at annealing temperatures between 800 and 1000 °C. This behavior explains the diffusion and aggregation behavior of interstitial Si. We also found that the defect density increased with a ramping-up rate of 15 °C/s. This result is expected to enhance the gettering capability of the CH₃O ion implantation region by optimization of the heat treatment sequence in the epitaxial growth process.

Chapter.5

Characteristics of CH₃O ion-implanted Si epitaxial wafer

5.1 Introduction

In Chapter 3, we introduced our novel CH₃O molecular ion implantation technique to enhance the gettering capability. We showed that the CH₃O ion implantation technique can be applied to the proximity gettering Si epitaxial wafer fabrication process, as described in Chapter 3. Furthermore, as shown in Chapter 4, the CH₃O ion implantation technique has characteristics of forming two types of defects: C-related and EOR, in one-time ion implantation after the Si epitaxial growth process. This characteristic is expected to enhance the gettering capability of the ion-implantation region. The enhancement in gettering capability is expected to improve the characteristics of the advanced CMOS image sensor because of the more efficient elimination of metallic impurity contaminations from the device active region. Thus, the proximity gettering technique using CH₃O ion implantation is expected to improve the characteristics of advanced CMOS image sensors.

By contrast, there are some unclear characteristics of proximity gettering using CH₃O ion implantation. The effect of the EOR defect as an additional defect in CH₃O ion implantation on gettering capability is not clear. Furthermore, the effect of the O (which is implanted as an additional element in CH₃O ion implantation) on the characteristics of advanced CMOS image sensors is not clear. The purpose of this chapter is to investigate

the effect of the CH₃O ion implantation technique on the gettering capability and characteristics of advanced CMOS image sensors.

In Chapter 5.2, we compare the gettering capability of Ni contamination between the use of CH₃O and C₂H₃. Ni is a representative metallic impurity contaminant because it is a major component in the stainless steel used for equipment piping. Therefore, it is made clear that the effect of additional EOR defects act as gettering site for metallic impurity contamination during device process. In Chapter 5.3, we investigate the effect of CH₃O ion implantation on the density of white spot defects. We also investigated the behavior of the elements and defects introduced by CH₃O ion implantation during the device fabrication processes. From these experiments, we will show that the proximity gettering technique using CH₃O ion implantation can contribute to improving the characteristics of advanced CMOS image sensors.

5.2 Experimental sample conditions

5.2.1 The gettering test wafer sample

We used 12-inch n-type (100) P- and C-doped CZ single-crystal Si wafers. The implantation energy was 80 keV/ion. The dose of the CH₃O and C₂H₃ ions was 7.5×10^{14} C atoms/cm². The ion beam current was the same for CH₃O and C₂H₃, i.e., 550 μA. Epitaxial growth of the samples was conducted after CH₃O ion and C-cluster ion implantation. The epitaxial layer thickness was 9.0 μm. For the Ni-gettering test, the sample wafers were contaminated with Ni metallic impurities (2.5×10^{13} atoms/cm²) by spin coating with a metallic-impurity-contaminated acid solution. The initial Ni surface concentration was measured by inductively coupled plasma-MS (ICP-MS) after spin

coating. After the metallic-impurity contamination, the wafers were heated at 900 °C for 30 min for Ni diffusion treatment.

5.2.2 The CMOS image sensor sample

We used 12-inch n-type (100) P- and C-doped CZ single-crystal Si wafers. The P concentration was 5.0×10^{14} atoms/cm³. The C concentration was $2.7\text{--}3.0 \times 10^{16}$ atoms/cm³. The wafers used in this experiment were prepared from the same Si crystal ingot. These wafers were implanted with CH₃O multi-element molecular ions at room temperature. The CH₃O ions were implanted at an implantation energy of 80 keV/ion. The implantation dose of the CH₃O ions was 7.0×10^{14} ions/cm². The ion beam current of CH₃O was 550 μA. A Si layer was grown on the sample after CH₃O ion and C-cluster ion implantation. The thickness of the epitaxial Si layer was 5.0 μm.

5.2.3 Analysis method

The distribution profiles of C, H, O, Ni, and Cu were analyzed by SIMS. In the case of CMOS image sensor wafers, we mechanically polished the surface layer to a depth of about 1 μm before high-sensitivity SIMS analysis. The concentration profiles before and after the device processing were compared considering the polishing depth in the samples after the device process. A sample before the device process refers to the sample after Si epitaxial growth. The defects within the implantation range of the multi-element molecular cluster ions were analyzed by TEM. The C and O distribution profiles within the CH₃O ion-implantation region were analyzed by 3D-APT. In 3D-APT analysis, needle-shaped samples are prepared using an FIB. The samples for 3D-APT analysis were lifted out within 5 μm from their surface, which is within the CH₃O ion-implantation

region. The 3D-APT data were analyzed using integrated visualization and analysis software (IVAS) from Cameca.

To analyze the effect of the CH₃O ion implantation technique on the electrical properties of CMOS image sensors, we evaluated the density of white spot defects that were larger than 145 electrons/s in samples with and without CH₃O ion implantation by dark current spectrometry (DCS) [110-113]. DCS analysis enables the measurement of the density of electrical defects due to metallic impurity contamination and that of interface state defects in the CMOS device structure. In this study, DCS analysis was performed using a CMOS image device structure, which is a four-transistor-type pinned PD fabricated by a CMOS device process line [114, 115].

After the DCS analysis, we measured the physical properties, such as the density of defects and the concentration depth profiles of implanted atoms and metallic impurities in the same sample that was used for DCS analysis. The density of bulk micro defects (BMDs) was measured using a BMD analyzer (MO-441[®], Raytex Optima Incorporated).

5.3 Enhancement of gettering capability using the CH₃O ion implantation technique

In Chapter 4.1, we showed that CH₃O ion implantation can form two types of defects, C-related defects and EOR defects. This result suggests that the gettering capability is expected to improve using the CH₃O ion implantation technique. In this chapter, we compare the gettering capability of Ni between the CH₃O ion and C₂H₃ ion-implantation regions. We will discuss the effect of the EOR defect on the gettering capability of Ni.

Figure 5.1 shows the SIMS depth profiles measured on the CH₃O ion-implanted epitaxial growth samples (CH₃O ions were implanted at 80 keV at a dose of 7.5×10^{14} C

atoms/cm²) after the Ni metallic impurity contamination process. The C peak concentration was 6×10^{19} atoms/cm³ in the CH₃O ion-implantation region (Figure 5.1). Moreover, the O peak concentration in this implantation region was 3×10^{19} atoms/cm³. These results suggest that the C and O impurities remained at concentrations exceeding the solid solubility in the Si single-crystal wafers after the Ni metal impurity contamination process. We also confirmed that Ni impurities were gettered in the CH₃O ion-implantation region. Therefore, the CH₃O ion-implantation region can getter Ni metallic impurities.

The SIMS depth profiles measured on the CH₃O and C₂H₃ ion-implanted epitaxial growth samples (CH₃O and C₂H₃ ions were implanted at 80 keV at a C dose of 7.5×10^{14} C atoms/cm²) after the Ni metallic impurity contamination process and are shown in Figure 5.2. Ni concentration peaks were observed in the CH₃O and C₂H₃ ion-implantation region (Figure 5.2). From these results, both CH₃O and C₂H₃ ion implantation techniques could getter the Ni contamination. The Ni concentration in the CH₃O ion-implantation region was 2.0×10^{13} atoms/cm² and that in the C₂H₃ ion-implantation region was 1.8×10^{13} atoms/cm².

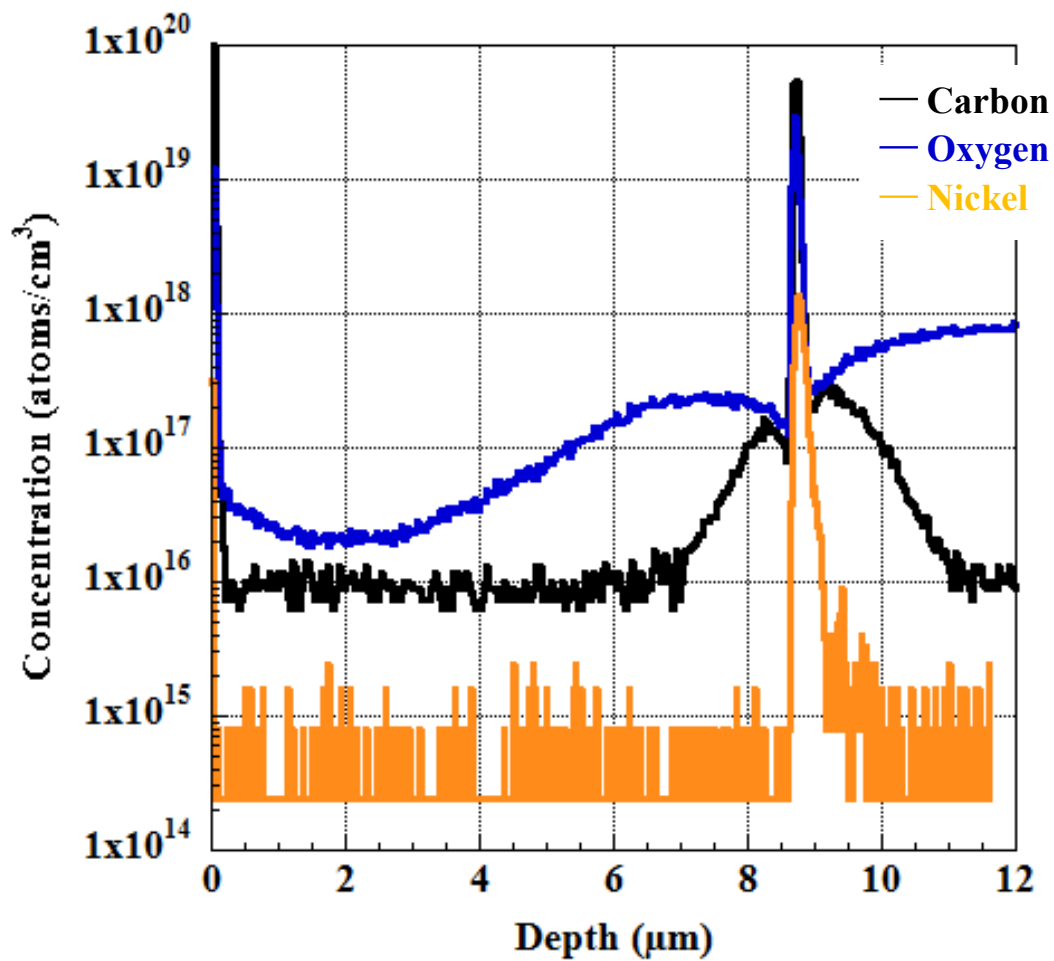


Fig. 5.1 SIMS depth profiles measured on a CH_3O ion-implanted epitaxially grown sample after Ni metallic-impurity contamination. The black, blue, and orange lines are the distribution profiles of C, O, and Ni, respectively.

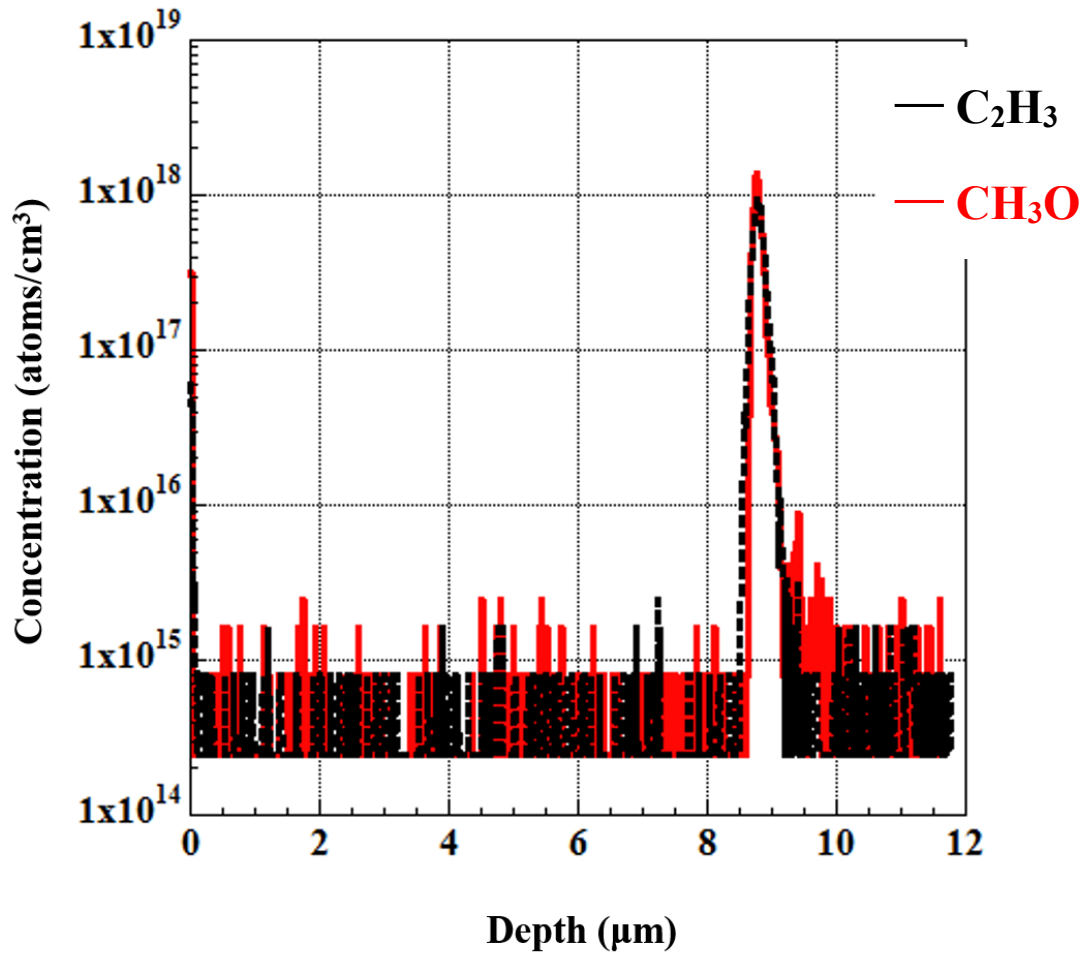


Fig. 5.2 SIMS depth profiles of Ni metallic-impurity contamination in CH_3O (red line) and C_2H_3 (black line) ion-implanted epitaxially grown samples

The Ni gettering efficiency of the CH₃O and C₂H₃ ion-implanted samples after Ni contamination is shown in Figure 5.3. The Ni gettering efficiency was calculated with the following equation,

$$\eta_{\text{eff}} = C_{\text{Ni}}/C_{\text{init}},$$

where η_{eff} is gettering efficiency, C_{Ni} is Ni contamination in the ion-implantation region, and C_{init} is initial surface contamination.

The Ni gettering efficiency in the CH₃O ion-implanted sample improved by 5.7% compared with the C₂H₃ ion-implanted sample (Figure 5.3). Thus, the CH₃O ion implantation technique presented a higher Ni gettering capability than C₂H₃ ion implantation.

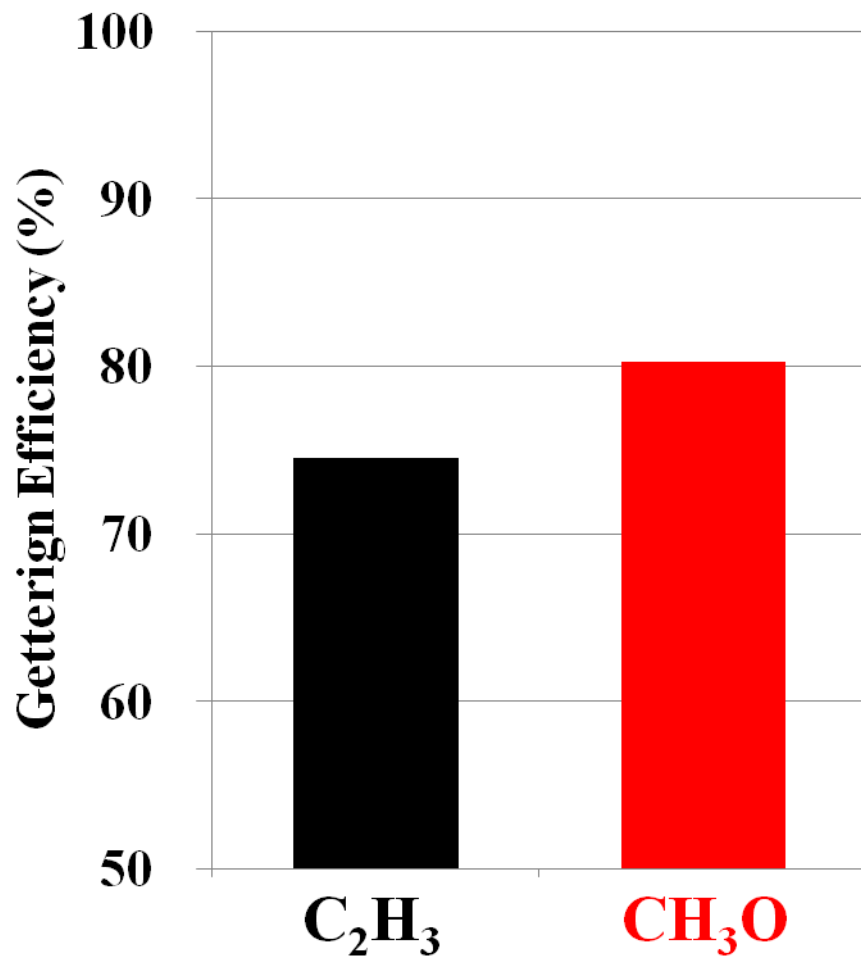


Fig. 5.3 Comparison of Ni gettering efficiency in C₂H₃ and CH₃O ion-implantation regions

The details of the gettering mechanism in the CH₃O ion-implantation region are not clear, but this improvement in gettering efficiency is considered to be the result of the effects of three kinds of estimated gettering sinks, as discussed below.

First, the C implantation region has a gettering capability on Ni. The C and O distribution depth profiles after the Ni metallic contamination process are shown in Figure 5.4. The C peak concentration in the CH₃O ion-implantation region was 5.5×10^{19} atoms/cm³ and that in the C₂H₃ ion-implantation region was 4.7×10^{19} atoms/cm³ (Figure 5.4). These results suggest that implanted C remains in the C₂H₃ and CH₃O ion-implantation region after the Ni metallic contamination process. Kurita *et al.* reported that the high C concentration region, which was formed by hydrocarbon molecular ion implantation, had a high gettering capability for various metals [54-58]. The CH₃O ion-implantation region had the same ordered C concentration as the C₂H₃ ion-implantation region (Figure 5.4). Furthermore, the CH₃O ion-implantation region had the same defects as the C₂H₃ ion-implantation region (Figure 4.3). Thus, it is conceivable that the CH₃O ion-implantation region has at least the same function as the C₂H₃ ion-implantation region.

Second, the EOR defects in the CH₃O ion-implantation region act as gettering sinks. As Figures 4.3 and 4.4 show, the CH₃O ion-implantation region had 50 nm defects. Kuroi *et al.* reported that secondary defects formed by high-energy ion implantation affect the gettering sinks [50]. The CH₃O ion implantation condition is not high energy. However, it is sufficiently conceivable that defects act as new gettering sinks, and the Ni gettering capability improves (Figure 5.1).

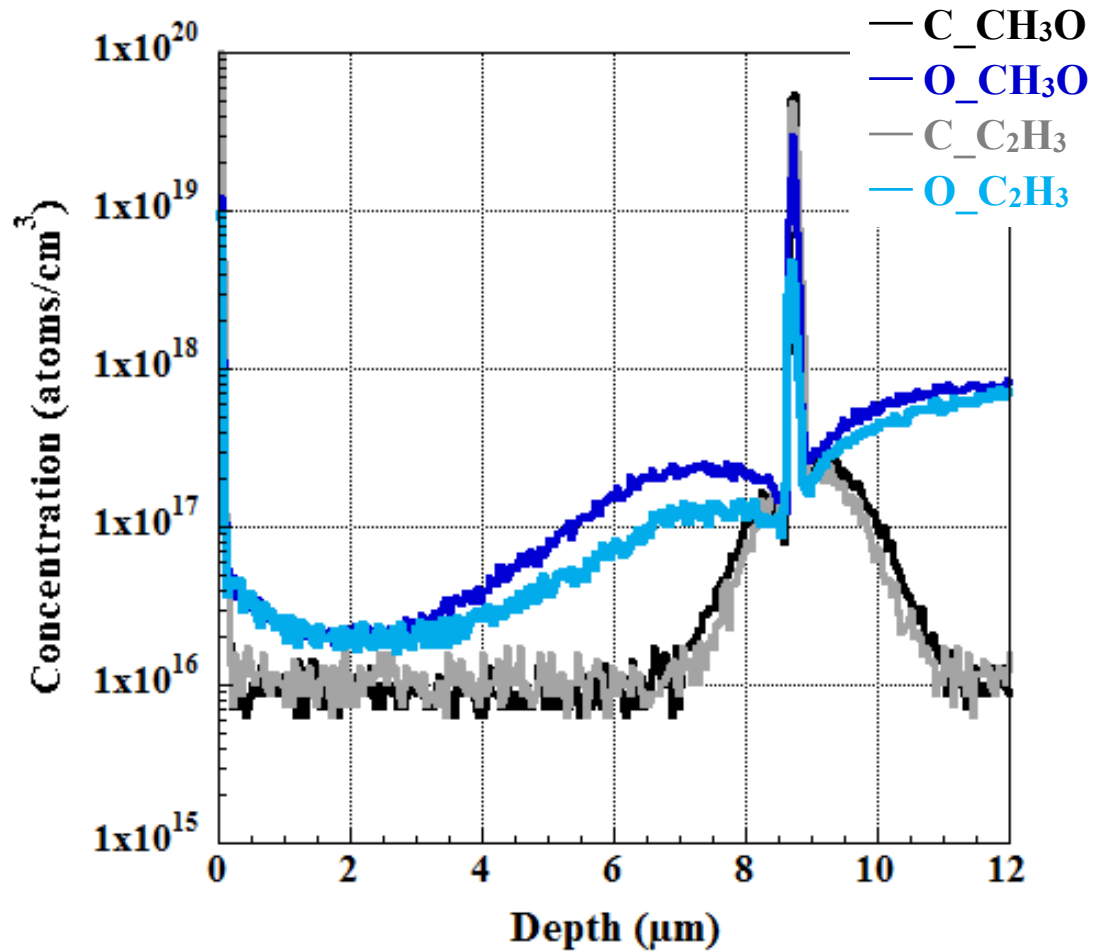


Fig. 5.4 SIMS depth profiles of C and O measured on CH₃O and C₂H₃ ion-implanted epitaxially grown samples after Ni metallic-impurity contamination. Black and gray lines are C distribution profiles for the CH₃O and C₂H₃ samples, respectively; dark blue and light blue lines are O distribution profiles for the CH₃O and C₂H₃ samples, respectively

Third, the VO complex point defects in the CH₃O ion-implantation region act as gettering sinks. The C concentration in the CH₃O and C₂H₃ ion-implantation regions was almost the same for each (Figure 5.4). However, the O peak concentration in the CH₃O ion-implantation region was over 10 times higher than that in the C₂H₃ ion implantation region (3.0×10^{19} atoms/cm³ for CH₃O and 1.5×10^{18} for C₂H₃). Shirasawa *et al.* used DFT to determine the binding energy between the metallic impurity and point defects [71-73]. In these calculations, the C-interstitial Si (C-I) complex, vacancy hydrogen (VH_n, n = 1 to 3) complex, or VO complex has a high binding energy with metallic impurities. In the case of CH₃O ion implantation, O was implanted at high concentration, and a vacancy was formed. Thus, it is considered that there was a high-concentration VO complex in the CH₃O ion-implantation region and the Ni gettering capability was improved due to the VO complex point defects.

Thus, it is considered that there are some factors for the increased gettering capability in the CH₃O ion-implantation region. Among them, the EOR defect in the CH₃O ion-implantation region is considered to contribute to the improvement in gettering capability of Ni contaminations.

5.4 Characteristics and effects of the CH₃O ion-implantation region for CMOS image sensor fabrication processes and performance

In the previous chapter, we showed that the gettering capability of an ion-implantation region was increased by CH₃O ion implantation. However, the method of Ni contamination discussed in Chapter 5.3 uses a contaminated liquid. Thus, the gettering behavior during the device fabrication process is not clear. Furthermore, the effect of the proximity gettering technique using CH₃O ion implantation on the characteristics of CMOS image sensors is not clear. In this chapter, first we explore the gettering behavior of the CH₃O ion-implantation region during the device fabrication process. Then, we investigate the defects and the implanted elements during the device fabrication process. Finally, we show the effect of the proximity gettering technique using the CH₃O ion implantation technique on the density of white spot defects.

5.4.1 Gettering effect of the CH₃O ion-implantation region on metallic impurity contamination during the CMOS image sensor device fabrication process

The distribution profiles of C, H, O, Ni, and Cu as a function of concentration after the device processes are presented in Figure 5.5. The concentration peaks of C, H, and O were observed at the same depth; thus, these concentration peaks were assumed to be attributable to CH₃O ion implantation. Furthermore, the Ni and Cu concentration peaks were observed at the same depth within the CH₃O ion-implantation region. These results suggest that within the CH₃O ion-implantation region, various metallic impurities are gettering. Furthermore, the CH₃O ion-implanted wafer forms two types of gettering sinks, the BMD and CH₃O ion-implantation regions. Nevertheless, Ni and Cu concentration

peaks were observed in the CH₃O ion-implantation region. This result suggests that the CH₃O ion-implantation region can getter metallic impurities during the device process.

To analyze the amount of Ni gettered during the device process, we analyzed the Ni concentration depth profiles by SIMS before and after the device process; see Figure 5.6(a, b). No Ni impurities were observed in the epitaxial layer and CH₃O ion-implantation region (Figure 5.6(a)). By contrast, a Ni concentration peak was observed within the CH₃O ion-implantation region (Figure 5.6(b)). The Ni concentration in the CH₃O ion-implantation region after the device process was 1.2×10^{11} atoms/cm². This result suggests that within the CH₃O ion-implantation regions, at least 1.2×10^{11} atoms/cm² of Ni impurities were gettered during the device processes.

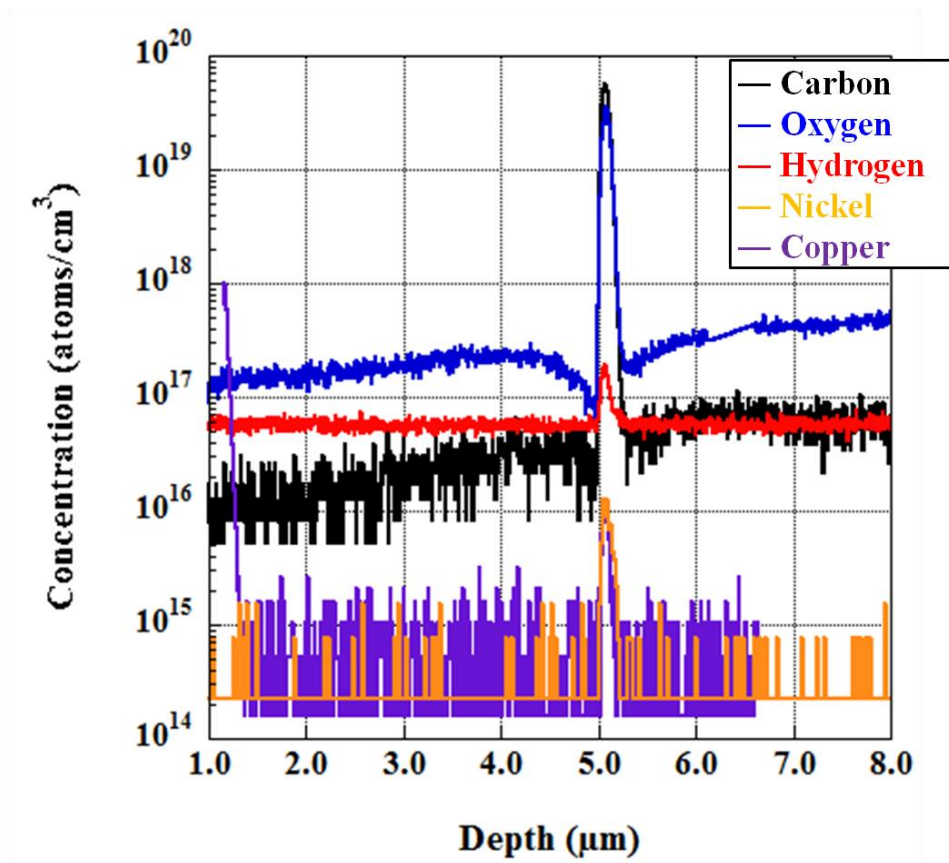


Fig. 5.5 SIMS depth profiles of C, O, H, Ni, and Cu after the device process

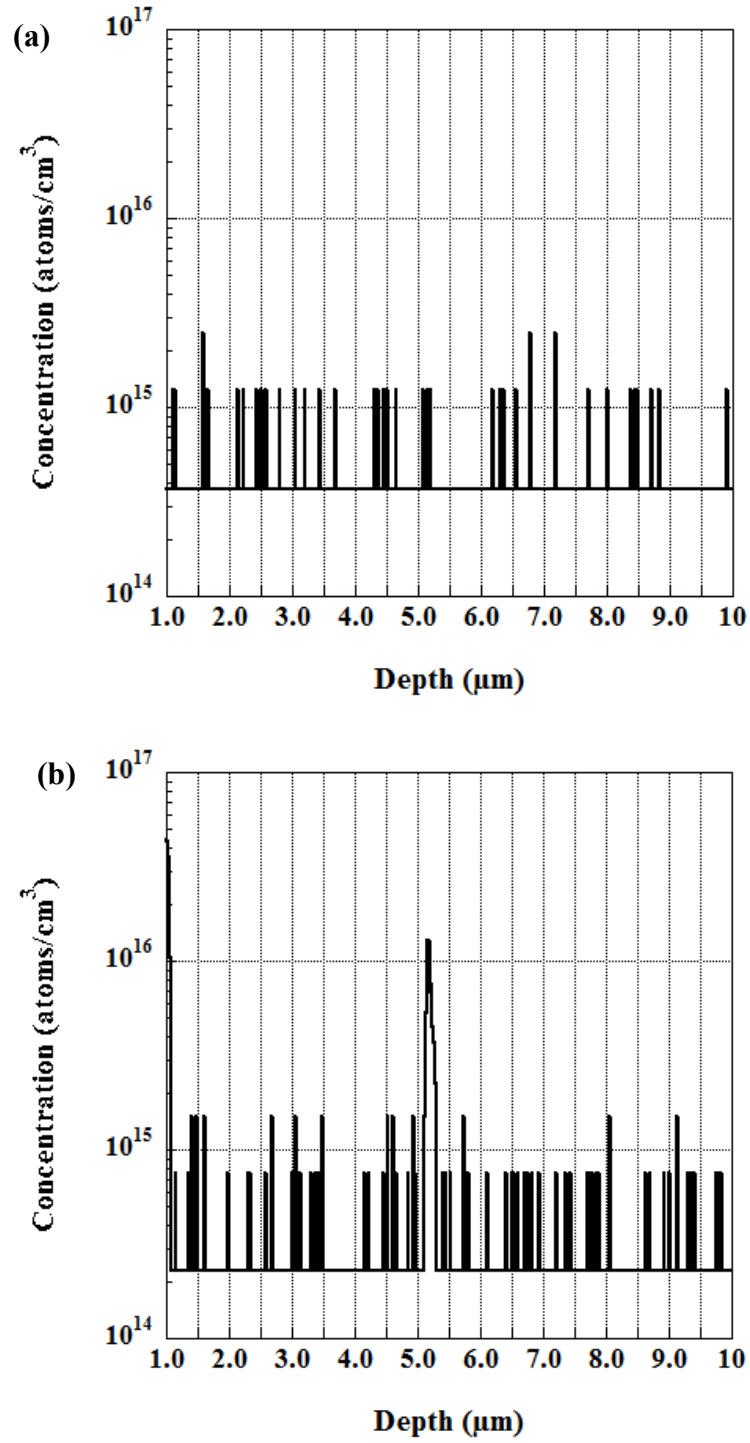


Fig. 5.6 Ni distribution profiles in the CH₃O ion-implanted wafer (a) before and (b) after the device process

5.4.2 Diffusion behavior of implanted elements by CH₃O ion implantation during the CMOS image sensor fabrication process

As shown above, gettering by CH₃O ion implantation is effective for metallic impurities during the device fabrication processes. In our previous study, we confirmed that the concentration peaks of C, O, and H occur within the CH₃O-implantation region, which are higher than their solid solubility because of two types of defects: stacking fault and C-related defect. We also confirmed that this range functions as the gettering sink for metallic impurities. Thus, understanding the diffusion behavior of implanted atoms and defect behavior during the device fabrication processes is important for understanding the effect of the CH₃O ion-implantation region. We investigated the diffusion behavior of C, O, and H, the three elements that were implanted by CH₃O ion implantation.

5.4.2.1 C-diffusion behavior

The C distribution profiles in Si epitaxial wafers with and without CH₃O ion implantation at a dose of 7.0×10^{14} ions/cm² are shown in Figure 5.7 before and after the device process. In the CH₃O ion-implanted epitaxial wafer, the C concentration in the CH₃O ion-implantation region before the device process was 5.0×10^{14} atoms/cm² and 5.1×10^{14} after. We confirmed that the C concentration near its peak was decreased by the device process. By contrast, the C concentration in the CH₃O ion-implantation region was higher than the solid solubility and was not changed by heat treatment. These results suggest that C atoms near their concentration peak diffused to the bulk of the Si wafer, whereas the C forming the concentration peak remained during the device heat treatment.

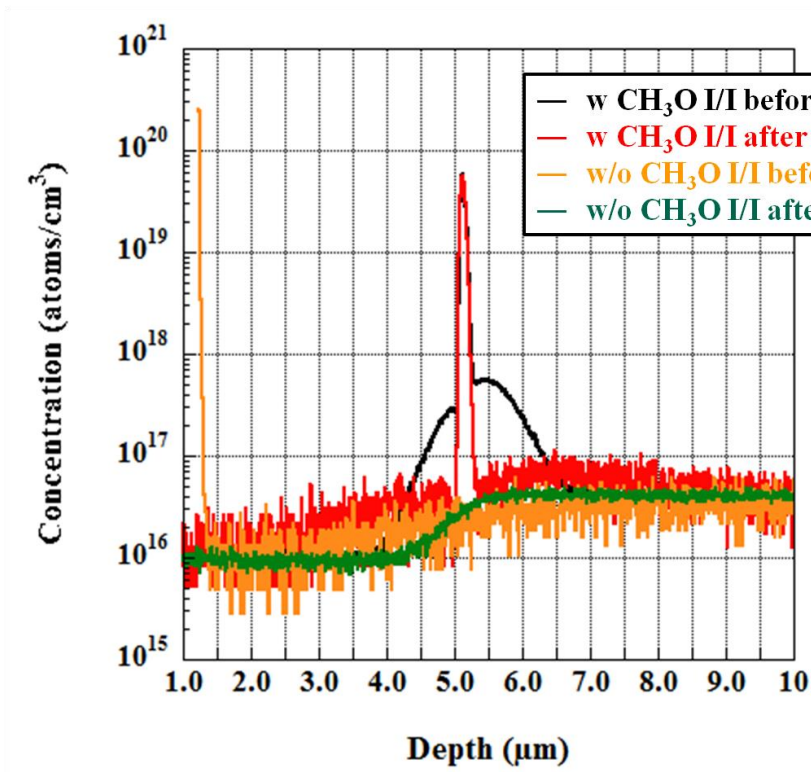


Fig. 5.7 C distribution profiles in CH₃O ion-implanted and unimplanted wafers (a) before and (b) after device process

In our previous study of Chapter. 4, it was found that the C implanted by CH₃O ion implantation generated defects through C aggregation. It is considered that the remaining C with its concentration peak higher than the solid solubility is due to the remaining defects generated by C aggregation. This high C concentration peak region functions as the gettering layer for metallic impurities. Thus, it is expected that the CH₃O ion-implantation region functions as a gettering sink during the CMOS device process.

5.4.2.2 O gettering behavior

Figure 5.8(a, b) shows the O distribution profiles before and after the device process. The O concentration peaks were observed in the CH₃O ion-implantation region. This indicates that this ion-implantation region gettered O before and after the device process. The O concentration in the epitaxial layer of the CH₃O ion-implanted wafer was higher than in the unimplanted wafer after epitaxial growth (Figure 5.8(a)). This difference was assumed to be due to the diffusion of implanted O into the epitaxial layer from the CH₃O ion-implantation region during the epitaxial layer growth process. By contrast, the O concentration in the epitaxial layer decreased in the CH₃O ion-implanted wafer after the device process (Figure 5.8(b)). The amount of O gettered in the CH₃O ion-implantation region before the device processes was 1.7×10^{14} atoms/cm² and 3.4×10^{14} after the processes. The amount of gettered O increased during the device process. This suggests that the CH₃O ion-implantation region can getter O atoms diffusing from the Si substrate during the device heat treatment.

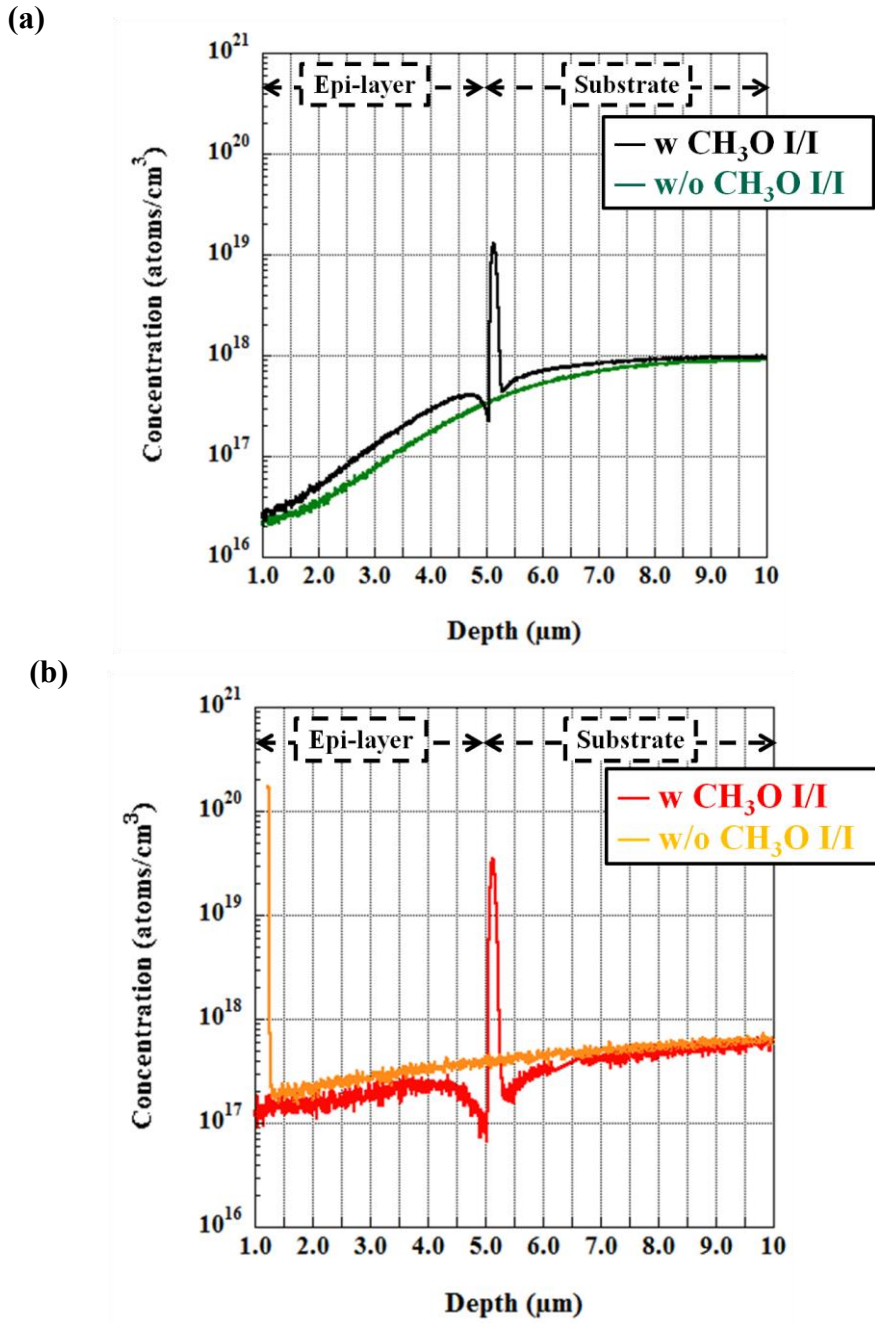


Fig. 5.8 O distribution profiles of CH₃O ion-implanted and unimplanted wafers (a) before and (b) after device process

Figure 5.9 shows the O-integrated concentrations from a depth of 1.4 μm to 5 μm , which is the interface of the Si substrate and the epitaxial layer where it can be measured by SIMS. The O-integrated concentration in the epitaxial layer without CH_3O ion implantation increased from 4.5×10^{13} to 1.0×10^{14} atoms/ cm^2 by the device heat treatment. However, in the CH_3O ion-implanted epitaxial wafer, the O concentration decreased from 6.8×10^{13} to 6.7×10^{13} atoms/ cm^2 . These results suggest that most of the O atoms that diffused from the Si substrate were gettered in the CH_3O ion-implantation region. Furthermore, the difference in the O distribution depth profile in the epitaxial layer was due to the diffusion of O that already existed in the Si epitaxial layer before the device process. Therefore, the CH_3O ion implantation technique does not increase the O concentration in the epitaxial layer, but rather reduces it by getting O during the device fabrication processes.

5.4.2.3 H gettering behavior

The H distribution profiles before and after the device process are shown in Figure 5.10. Before the device process, the H concentration in the CH_3O ion-implantation region was 8.6×10^{12} atoms/ cm^2 , and 1.2×10^{12} after that. The amount of H that diffused from the CH_3O ion-implantation region was 7.4×10^{12} atoms/ cm^2 . We confirmed that H diffused from the CH_3O ion-implantation region during the device process. Okuyama *et al.* reported the diffusion behavior in a CH_3O ion-implanted Si epitaxial wafer during isothermal annealing [59-61]. In their study, almost 7.4×10^{12} H atoms/ cm^2 diffused. Thus, the same amount of H diffused during the device process. Therefore, it is expected that the CH_3O ion-implanted Si epitaxial wafer can passivate the interface state defects by H diffusion from the CH_3O ion-implantation region.

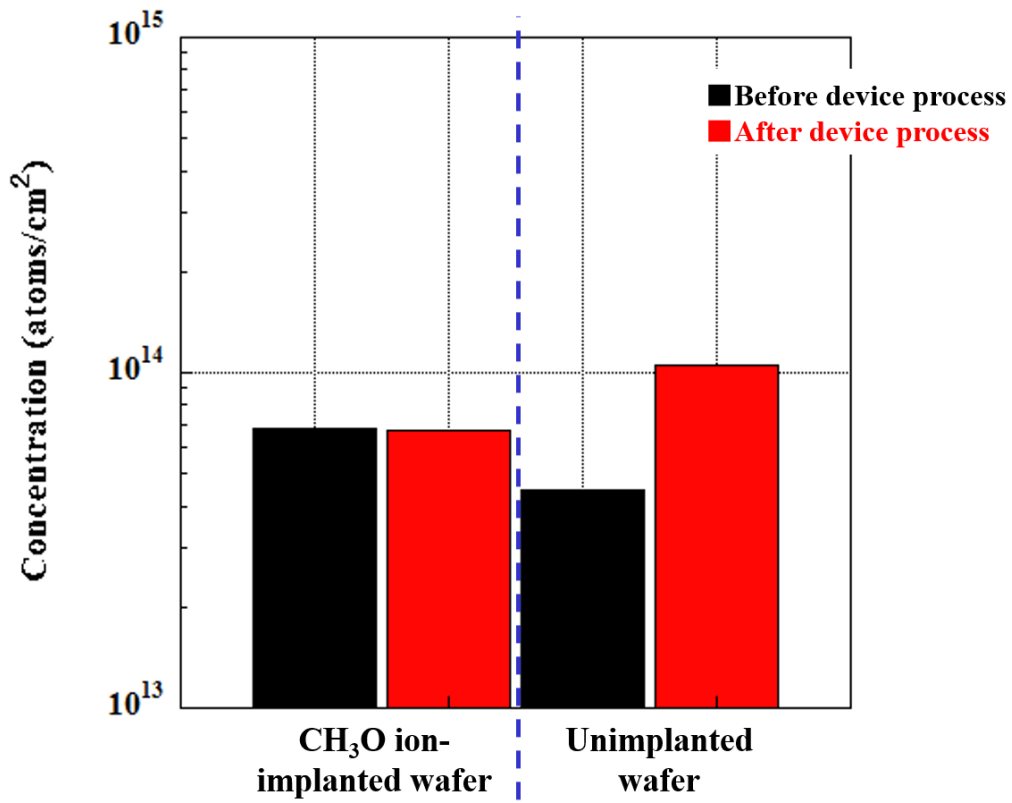


Fig. 5.9 O concentrations in epitaxial layer of wafers with and without CH₃O ion implantation before and after the device process

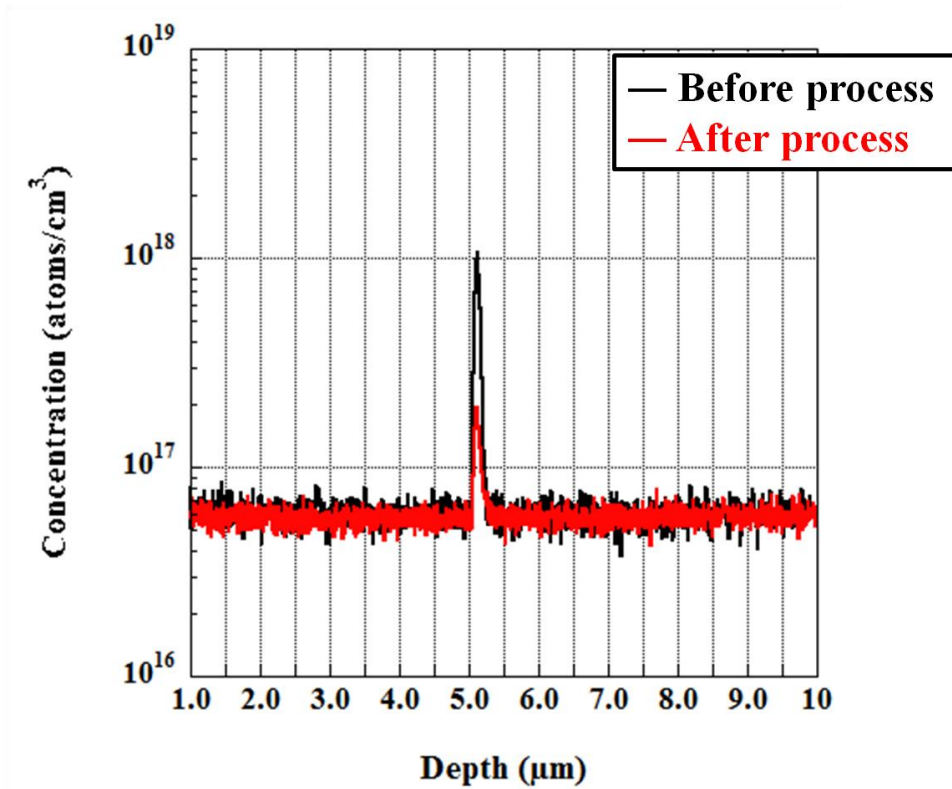


Fig. 5.10 H distribution profiles before and after the device process

5.4.3 Defect morphology observation in the CH₃O ion-implantation region

In the previous chapter, we investigated the diffusion behavior of ion-implanted atoms during the device fabrication process. Typically, the diffusion behavior of atoms and defect behavior are closely related. Furthermore, understanding the defects in Si crystals is important for understanding the gettering effect because the defects act as gettering sinks.

The CH₃O ion-implanted epitaxial wafer is expected to have two regions of gettering sinks: the CH₃O ion-implantation region and the BMD region. The CH₃O ion-implantation region is located near the interface between the epitaxial layer and the substrate (Figure 5.8). In contrast, the formation region of BMDs is the bulk of the Si substrate about 30 μm below the surface. Thus, the CH₃O ion-implantation region is located nearer to the device active region than the BMD region. In this chapter. 5.4.3, we investigate the defect behavior in the CH₃O ion-implanted epitaxial wafer during the device fabrication process.

5.4.3.1 BMD formation behavior

The BMD densities in the CH₃O ion-implanted and unimplanted Si epitaxial wafers analyzed using MO-441 are shown in Figure 5.11. CH₃O ions were implanted at a dose of 7.0×10^{14} ions/cm² and the BMD density in the unimplanted Si epitaxial wafer was 2.7×10^9 /cm³.

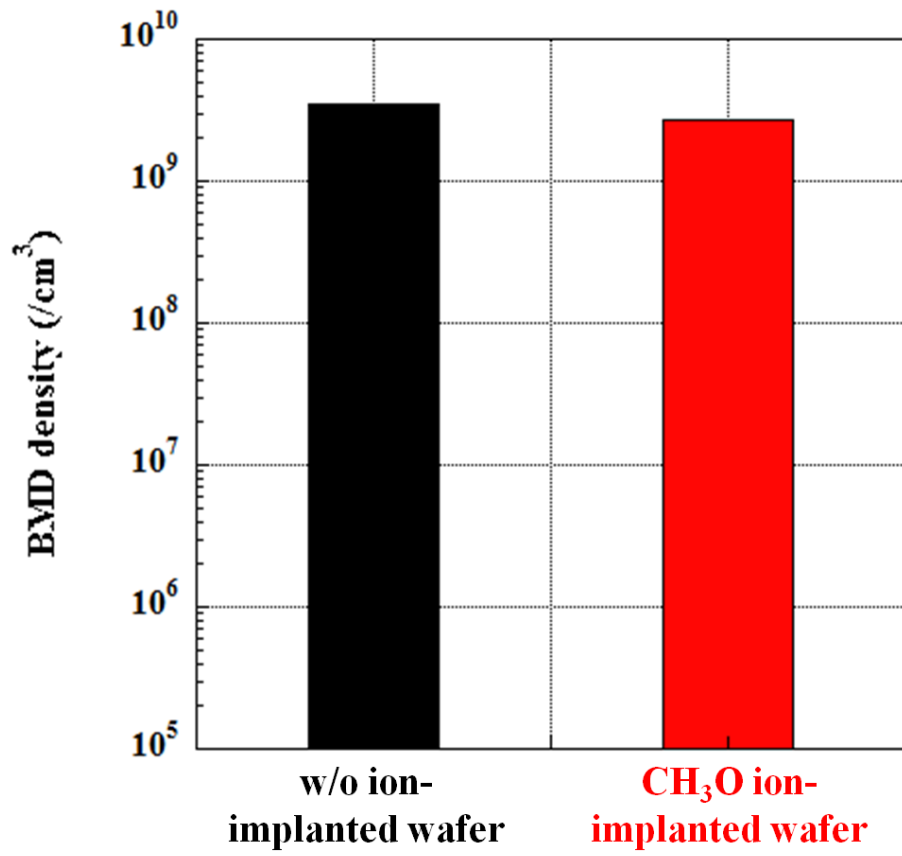


Fig. 5.11 BMD densities in CH₃O ion-implanted and unimplanted wafers

The BMD density in the CH₃O ion-implanted Si epitaxial wafer was $3.4 \times 10^9 / \text{cm}^3$, which is slightly higher than that of the unimplanted wafer. The reasons for the increase in BMD density are considered to be the difference between initial C and O levels in the Si substrate and the effects of C and O introduced by the CH₃O ion implantation. However, the depth of the BMD region is over 30 μm from the substrate/epitaxial layer interface.

Thus, the CH₃O ion-implantation region is far from the BMD region. It is considered that the impact of CH₃O ion implantation on BMD formation is small. We speculated that the difference in BMD density between the CH₃O ion-implanted and unimplanted wafers is due to the difference between the O and C concentrations in the substrate. From Figure 5.11 it is considered that the gettering capability of the BMD region in the unimplanted and CH₃O ion-implanted wafers because of the BMD density in these wafers is almost the same.

5.4.3.2 CH₃O ion-implanted defect behavior

Figure 5.12(a, b) shows cross-sectional TEM images of the CH₃O ion-implantation region before and after the device process, respectively. CH₃O ions were implanted at a dose of 7.0×10^{14} ions/cm². In Figure 5.12(a) and 5.12(b), two types of defect were observed: C-related defects of almost 5 nm in size and large ion implantation defects. The 5 nm defects were observed as black points in Figure 5.12(a, b). In a previous study of Chapter. 4, ion implantation defects were determined to be Si {111} stacking faults. We assumed that these two types of defect functioned as gettering sinks. Focusing on the stacking fault defects, their density did not change as a result of the device process, from which we assumed that the gettering capability for stacking fault defects was also unchanged during the device process.

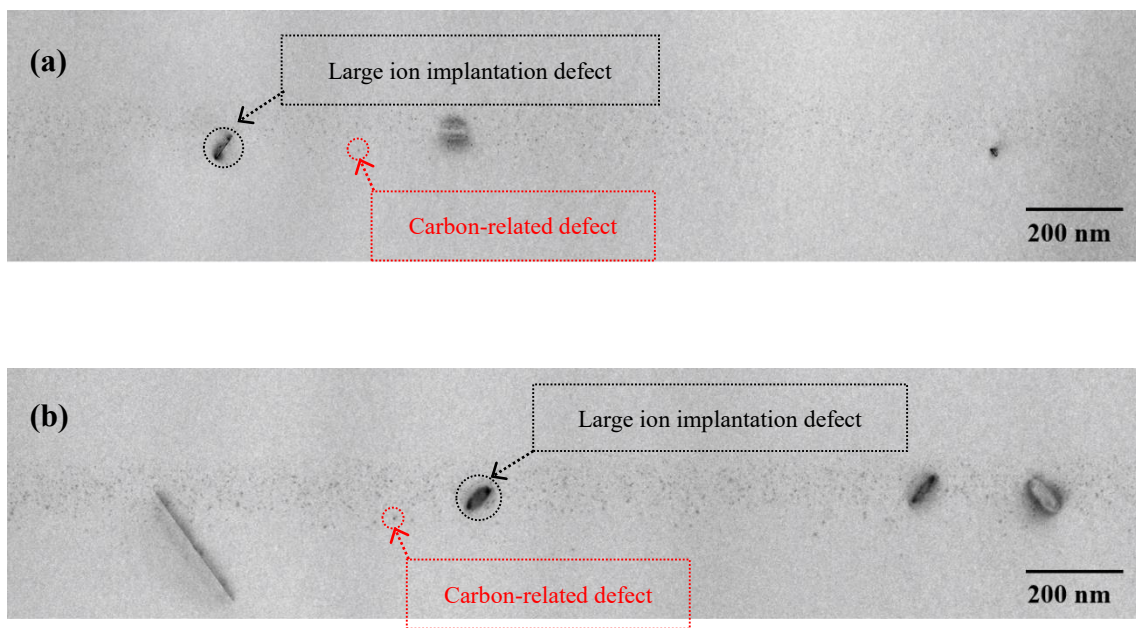


Fig. 5.12 Cross-sectional TEM images of CH_3O ion-implantation region (a) before and (b) after the device process

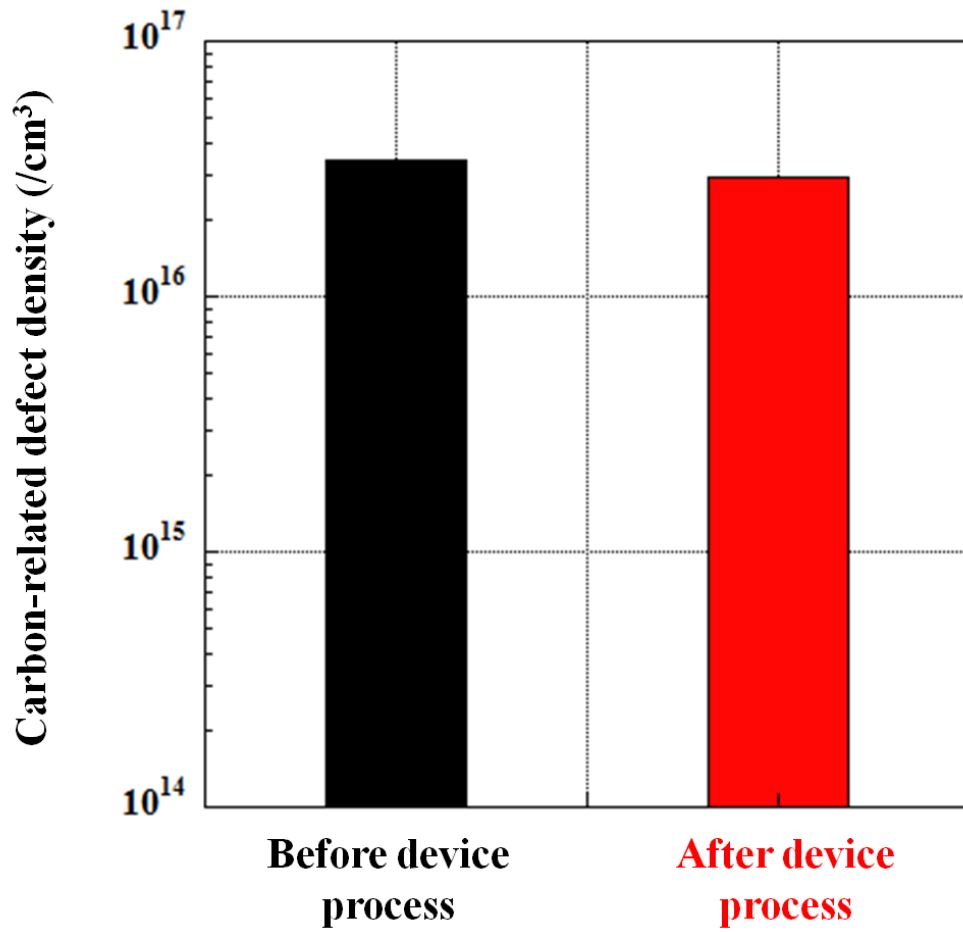


Fig. 5.13 C-related defect densities before and after the device process

The densities of the 5 nm C-related defects are shown in Figure 5.13. The defect density before the device process was $3.4 \times 10^{16} / \text{cm}^3$ and the defect density after the device process was $2.9 \times 10^{16} / \text{cm}^3$. The density of the 5 nm defects did not change as a result of the process.

In a study of the hydrocarbon molecular ion implantation technique, the gettering capability increased with increasing density of the 5 nm defect density [54-58]. Thus, we assumed that the gettering capability of the CH₃O ion-implantation region was maintained during the device process.

Figure 5.14 (a, b) shows cross-sectional SEM images of samples for C-related defect analysis by 3D-APT before and after the device process along with their C and O distribution maps. These samples were prepared for analysis of the 5 nm defects, which were located far from stacking fault defects, and aggregation of C and O was observed (Figure 5.14 (a, b)).

To reveal the C and O atom distributions, the maps showing 2 at.% C and 5 at.% O isoconcentration surfaces extracted from the CH₃O ion-implantation region before and after the device process are shown in Figure 5.14 (a, b). The regions with high C and O concentrations almost overlap. Furthermore, the O concentration in the O aggregation region after the device process was higher than before the device process. This result indicates that the C aggregation region can gather O that diffused from the CZ silicon substrate during the device process (Figure 5.14 (a, b)).

STEM images and 3D-APT analysis results for stacking fault defects in the samples before and after the device fabrication process are shown in Figure 5.15. The STEM images show stacking fault defects in the samples (Figure 5.15).

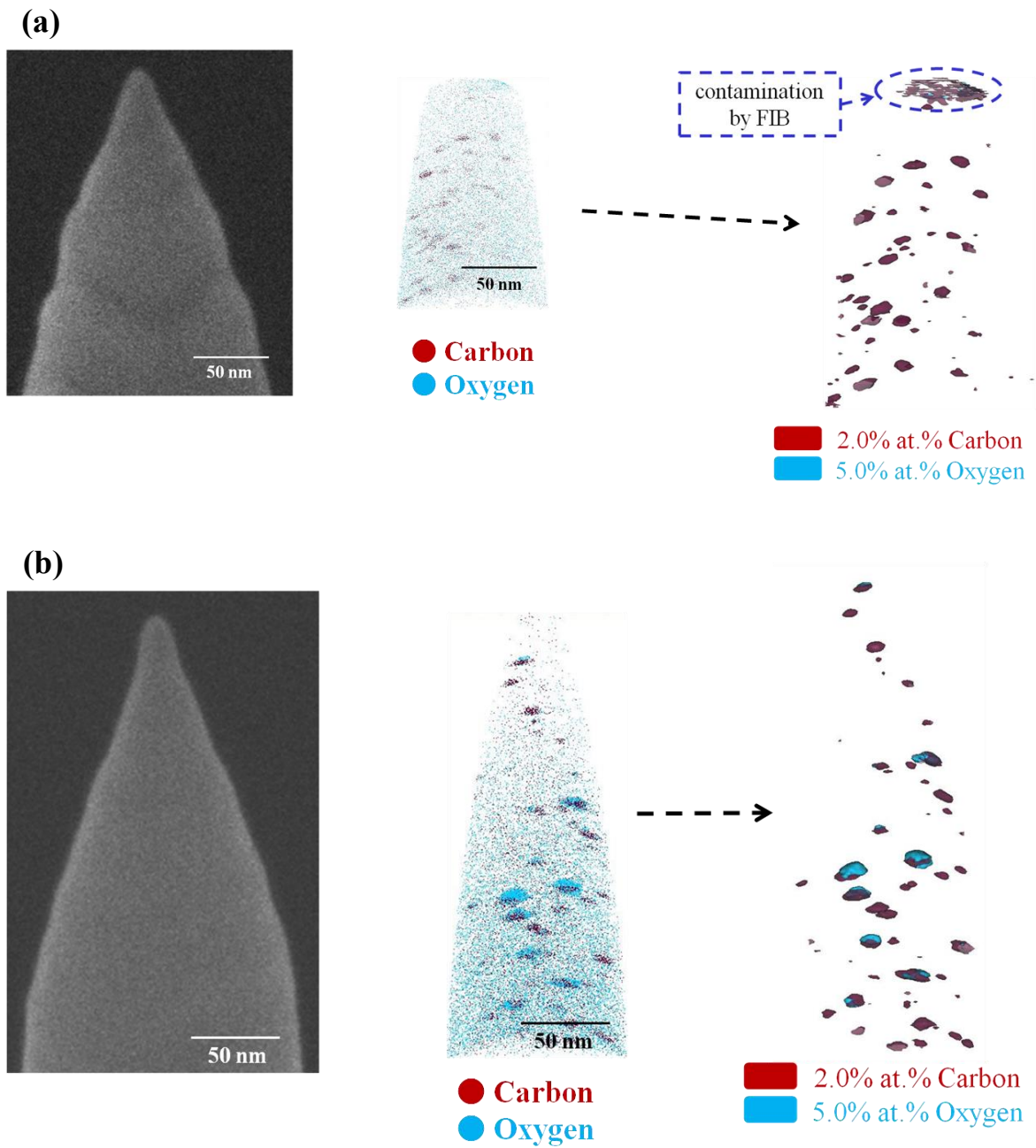


Fig. 5.14 Cross-sectional SEM images of needle-shaped samples and 3D-APT analysis results of atom maps and isoconcentration surfaces at 2.0 at.% C and 5.0 at.% O on C-related defects in the CH_3O ion-implantation region (a) before and (b) after the device process

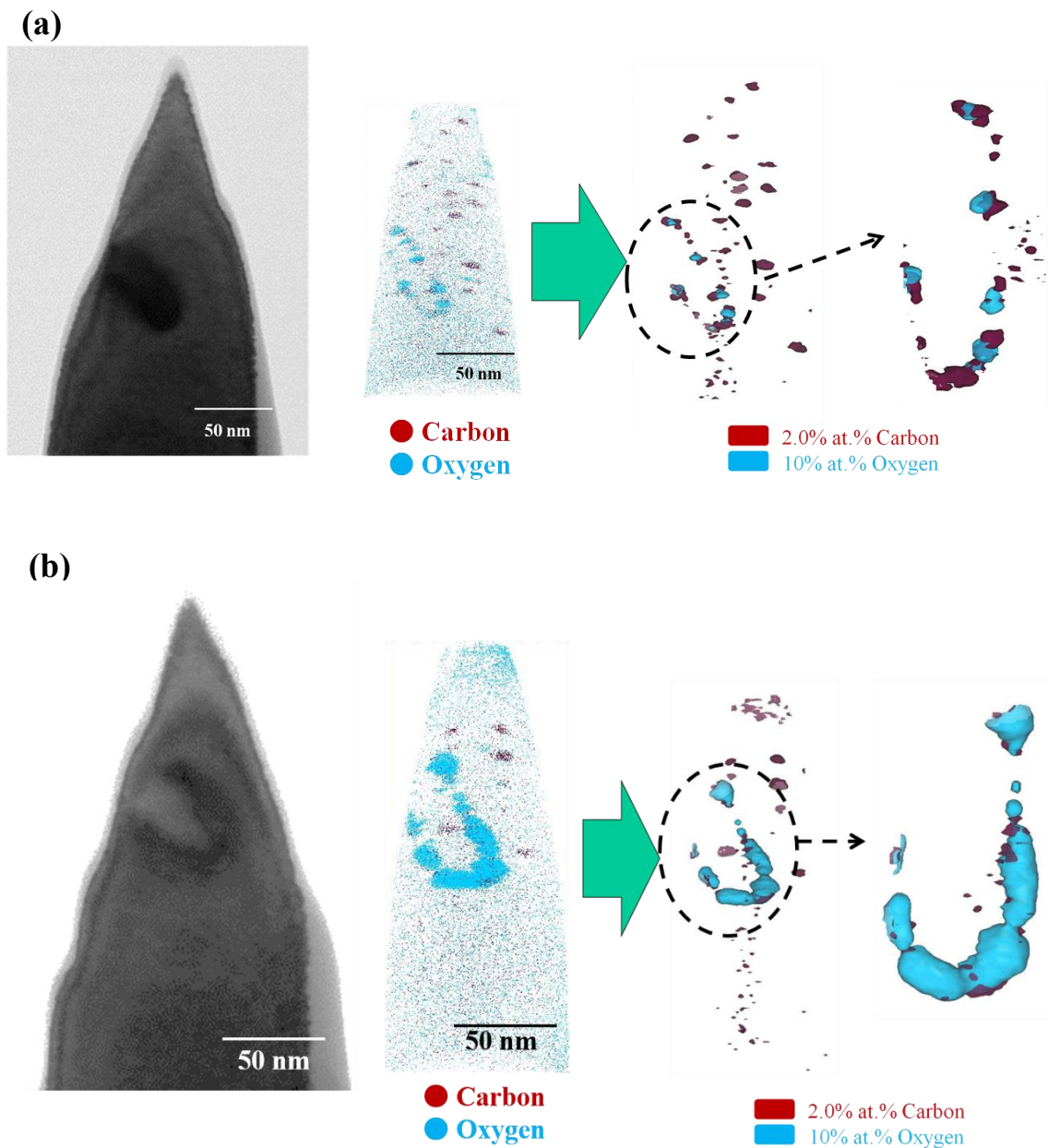


Fig. 5.15 Cross-sectional STEM images of needle-shaped samples and 3D-APT analysis results of atom maps and isoconcentration surfaces at 2.0 at.% C and 10 at.% O on stacking fault defects in the CH₃O ion-implantation region (a) before and (b) after the device process

The C and O distribution maps before and after the device process, which respectively show that the aggregations of C and O, are assumed to be located around the stacking fault defects (Figure 5.15 (a, b)).

To reveal the distribution of C and O atoms, the maps showing isoconcentration surfaces with 2 at.% C and 10 at.% O extracted from the CH₃O ion-implantation region before and after the device process are respectively shown in Figure 5.15 (a, b). The regions with high C and O concentrations almost overlap. Furthermore, the region with 10 at.% O after the device process was wider than that before the device process, suggesting that the O concentration in the CH₃O ion-implantation region around the stacking fault defects was significantly higher after the device process than before it. It is considered that the stacking fault defects function as gettering sinks for O impurities that diffused from the Si substrate during the device process. In particular, the O concentration around the stacking fault defects is higher than that around the C aggregation region near the stacking fault defects, indicating that the stacking fault defects are stronger gettering sinks for O than for the C aggregation region.

As mentioned above, the CH₃O ion-implantation region can getter various elements. It is assumed that this characteristic contributes to the reduction in white spot defect density. Then, why can the CH₃O-implantation region getter various elements? What is the mechanism underlying the gettering effect in the CH₃O ion-implantation region?

Generally, there are two mechanisms underlying the gettering effect in Si wafers. The first is segregation gettering. Segregation gettering is induced by the difference in solid solubility for metallic impurities [116]. If gettering sinks have higher solid solubility than the bulk of the Si crystal, the gettering sinks can gather the metallic impurities. The second is relaxation gettering. This type of gettering is caused by the stress field [25]. For

example, the stress field induced by a defect such as dislocations can getter metallic impurities.

The CH₃O ion-implantation region has two types of defect functioning as gettering sinks (Figure 5.12). Figure 5.14 also shows that C-related defects arise from C and O aggregation. This type of defect is similar to that generated by hydrocarbon molecular ion implantation. Kurita *et al.* reported that the mechanism of gettering C-related defects is segregation [54-58]. Therefore, it is considered that the mechanism of gettering C-related defects in the CH₃O ion-implantation region is segregation.

By contrast, a different mechanism of gettering stacking fault defects is assumed. In general, the mechanism of gettering secondary defects generated by ion implantation such as high-energy ion implantation is relaxation [117]. Because the ion-implanted defects in the CH₃O ion-implantation region are stacking fault defects, it is considered that the mechanism of gettering these defects is relaxation. However, the C complexes reside around the stacking fault defects (Figure 5.15). Moreover, the O atoms that diffused during the device heat treatment are gettered by the C complexes. Thus, it is considered that the C complexes around the stacking fault defects function as gettering sinks for metallic impurities. The mechanism of gettering the C complexes existing in the Si crystal bulk is segregation. In addition, Shirasawa *et al.* reported that the C complexes in the Si crystal have a high binding energy for various metallic impurities, as determined by DFT calculation [71-73]. Therefore, the mechanism of gettering the C complexes around the stacking fault defects is considered to be segregation. In conclusion, it is considered that the mechanism of gettering the stacking fault defects in the CH₃O ion-implantation region is a combination of the relaxation type for secondary defects and the segregation type for the C and O complexes.

In order to examine the contribution of each defects to oxygen gettering, an investigation was conducted using the results in Fig. 5.15. Fig. 5.16 shows the average number of oxygen atoms gettered by each defects. The gettered oxygen atoms in C-related defects are defined as the atoms located within the 10 nm square cube centered on the aggregated carbon as shown Fig. 5.15 (a). The gettered oxygen atoms by EOR defect are defined as the atoms located within the rectangular which include the EOR defect as shown Fig. 5.15 (b). As shown Fig. 5.14 (b) and 5.15 (b), the EOR defect is not completely include in the 3D-APT samples. The number of oxygen atoms gettered by the EOR defect showed in Fig. 5.16, shows the corrected value assuming that 3/4 of gettered oxygen atoms are included in analysis region. As shown in Fig. 5.16, the amount of gettered oxygen in EOR defects and C-related defects are increased after the device process. It is found that these defects function as gettering site on diffused oxygen during device process. And the number of gettered oxygen in EOR defects is higher than that in C-related defects. An increase rate of oxygen atoms in each defects are almost same. Therefore, these defects function to the same extent as gettering sites for oxygen.

Fig. 5.17 shows the concentration of the oxygen gettered by each defects. The gettered oxygen concentration was calculated from the number of gettered oxygen atoms by each defects as shown in Fig. 5.16, and the defect density of each defects from TEM observation results as shown in Fig. 5.12. The C-related defects assumed to be uniformly distributed in CH₃O implanted region which width is 200 nm. As shown in Fig. 5.17, the concentration of the oxygen gettered by the C-related defects was higher than that of EOR defects. This result suggests that the C-related defect is more effective on the oxygen gettering than EOR defect. This difference is considered to be occurred by the deference of the density of each defects. The density of C-related defect is almost $3.5 \times 10^{16} \text{ cm}^{-3}$.

On the other hand, The density of EOR defect is almost $6.4 \times 10^{13} \text{ cm}^{-3}$. Therefore, the C-related defects can getter higher concentration of oxygen than EOR defects, because of the high density of the defects. However, the EOR defects can getter the 31% of oxygen in after device process sample compare with the C-related defects. This result suggests that the EOR defects also contribute to the oxygen gettering during device process.

Fig. 5.18 shows the comparison of gettered oxygen concentration between the 3D-APT results and the SIMS results. As shown in Fig. 5.18, it is consistent that the oxygen concentration tends to increase after the device process. On the other hand, the concentration of gettered oxygen calculated from 3D-APT results were half of the SIMS analysis results. This difference is considered to be occurred by two reasons. The first is the difference in atom detection efficiency. The atom yield of 3D-APT is lower than SIMS. The atom yield of 3D-APT in this study is almost a half. The second is non-uniformity of C-related defects. The oxygen atoms diffuse only from the silicon substrate during device process. Amount of gettered oxygen by C-related defects located deeper region is higher than that by C-related defects located shallow region. From these reasons, the oxygen concentration calculated from 3D-APT results were different from the calculation from SIMS results.

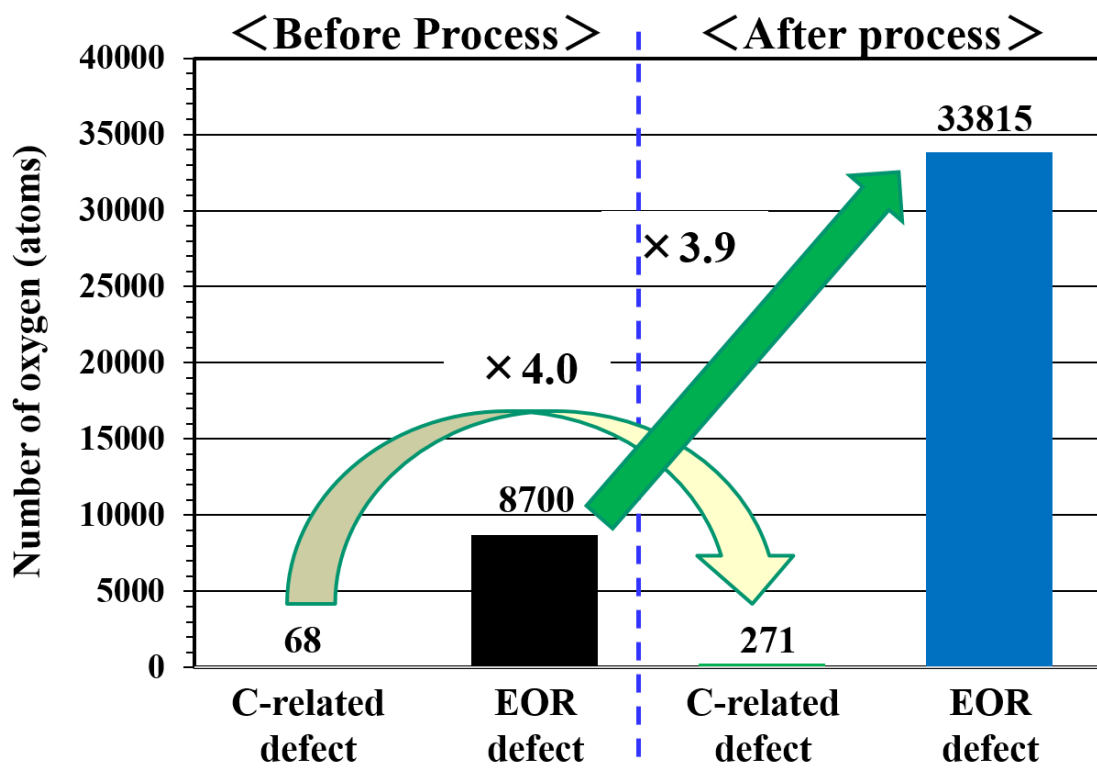


Fig. 5.16. The number of oxygen atoms gettered by the C-related and EOR defect

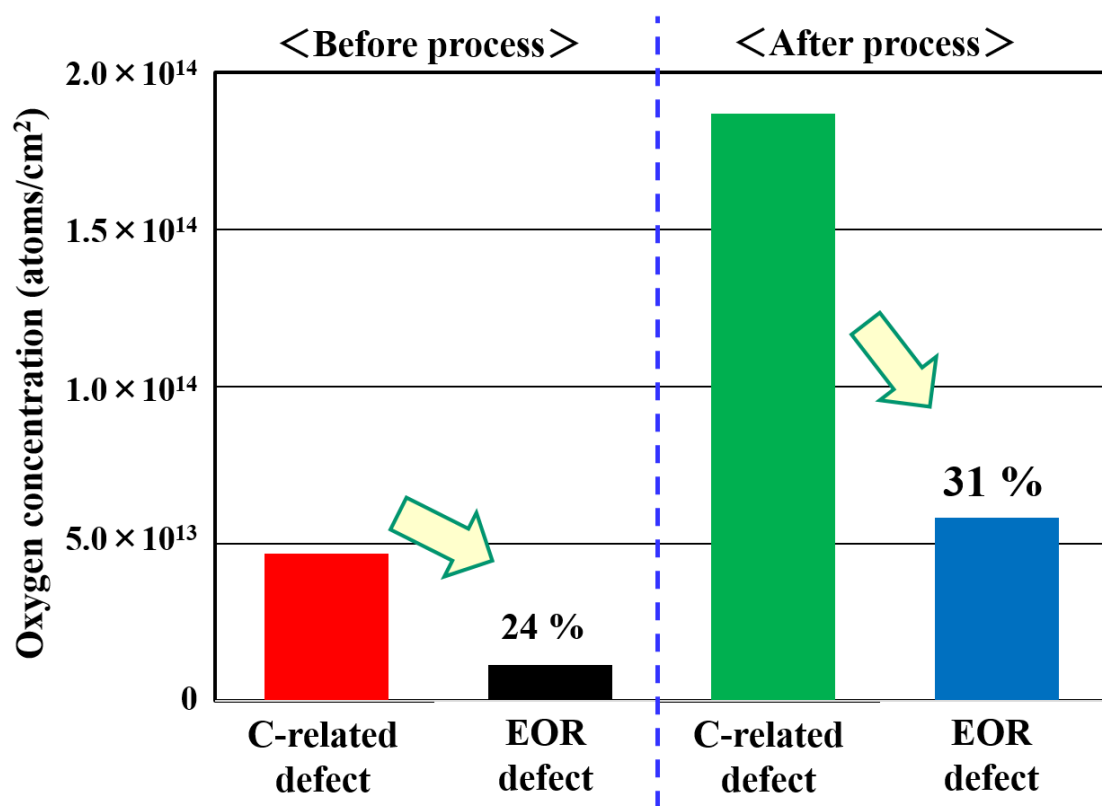


Fig. 5.17. The concentration of the oxygen gettered by C-related and EOR defects.

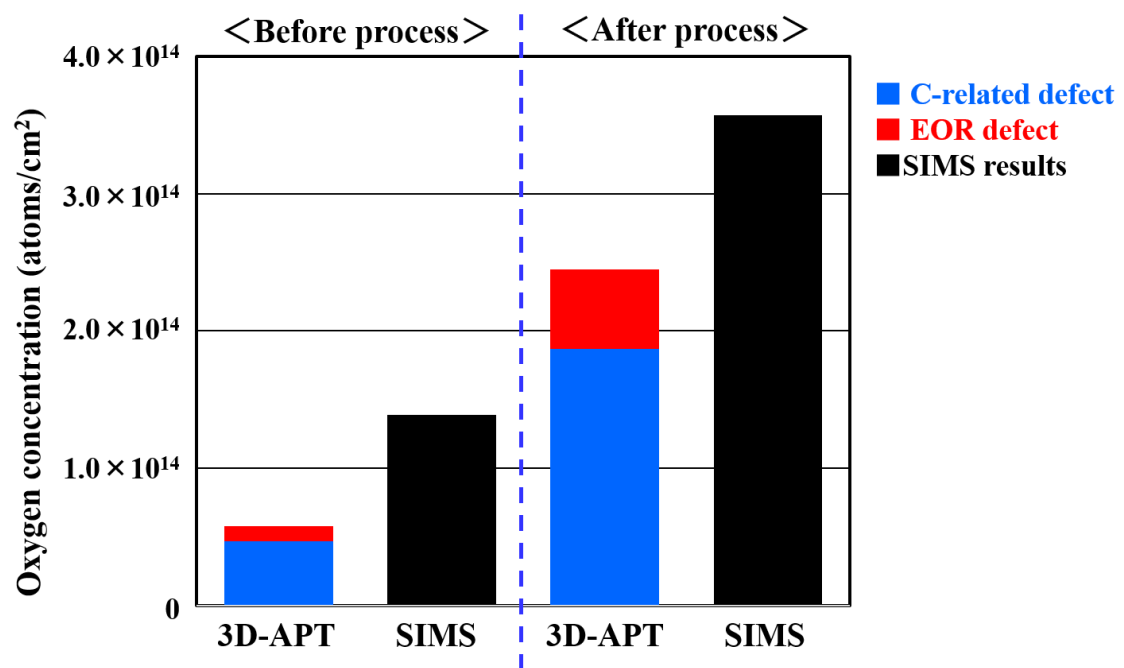


Fig. 5.18. The comparison of gettered oxygen concentration between the 3D-APT results and the SIMS results.

5.4.4 Reduction in white spot defect density by using CH₃O ion implantation

In the previous chapter, we confirmed that the CH₃O ion-implantation region is effective for gettering metallic impurities during the device fabrication process. Furthermore, the H atoms that diffused during the device fabrication process are expected to passivate the Si/SiO₂ interface. These characteristics are expected to improve the electrical properties of CMOS image sensors. In this chapter, we report on the effects of CH₃O ion implantation on the electrical properties of CMOS image sensors by measuring the DCS; these effects determine the density of white spot defects. Figure 5.19 shows that the density of white spot defects is larger than 145 electrons/s when comparing between CH₃O ion-implanted and unimplanted Si epitaxial wafers. CH₃O ions were implanted at a dose of 7.0×10^{14} ions/cm². As shown in Figure 5.19, the density of white spot defects was decreased by CH₃O ion implantation, suggesting that the latter implantation could improve the electrical properties of CMOS image sensors.

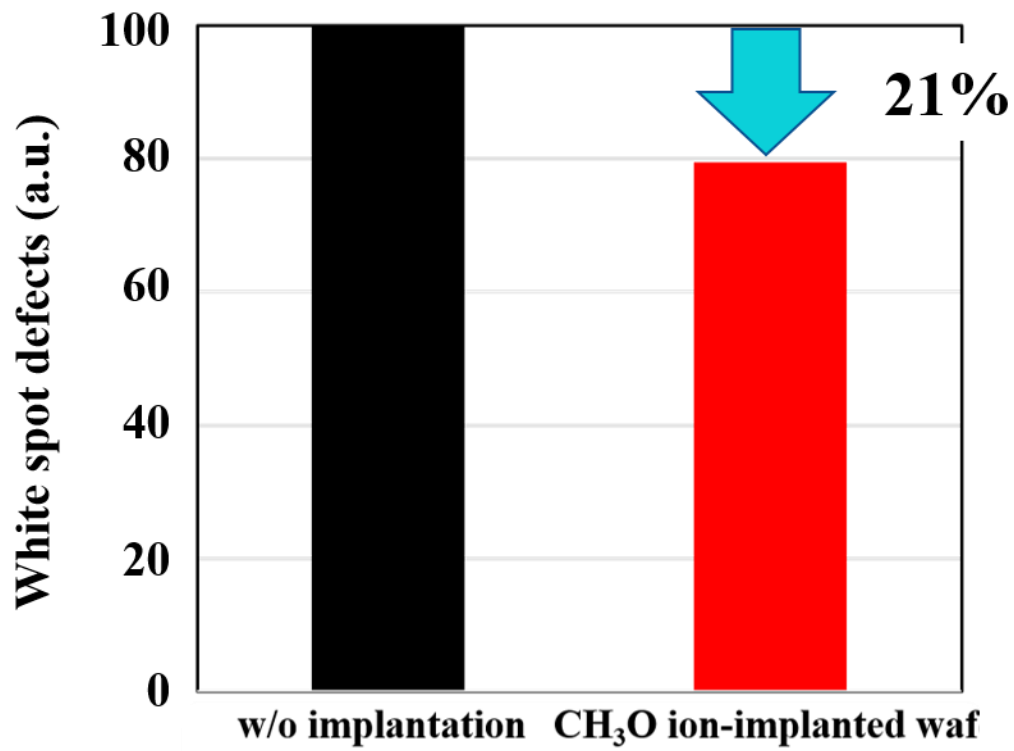


Fig. 5.19 Density of white spot defects in wafers with and without CH₃O ion implantation

Why can CH₃O ion implantation reduce the white spot defect density in CMOS image sensors? We assume that there are three possible mechanisms.

First, the gettering capability for metallic impurities is higher during the CMOS device process. In particular, the metallic impurities have a large effect on the density of white spot defects [112, 113, 118, 119]. The deep energy levels that were formed by metallic impurities function as electron–hole pair centers generated by thermal energy without photo irradiation. As a result, the CMOS image sensors generate unexpected electrical signals that are detected as white spot defects. Russo *et al.* reported the effect of metallic contaminations on the dark current of CMOS image sensors [119]. Metallic contaminations significantly affects the increase of dark current. Fig. 1.3 shows the temperature dependence on the dark current [23]. The diffusion current is the dark current caused by the diffusion of minority carrier from the bulk of silicon substrate to the PD. The generation current is the dark current caused by the deep energy levels in silicon crystal band gap caused by the metallic contaminations in PD.

In the room temperature operation, the generation current is higher than the diffusion current. If there is no metallic impurities, the dark current can be reduced to 1/10 at room temperature operation. The CH₃O ion-implantation region can getter more metallic impurities than the BMD region as shown in Figures 5.5 and 5.6. The CH₃O ion-implantation region can be formed closer to the device region than the BMD region.

The CH₃O ion-implantation region is considered to be effective for gettering metallic contaminations in device region during device processes. Thus, CH₃O ion-implantation technology is quite useful to reduce white spot defects in CMOS image sensors.

Second, the oxygen concentration in the epitaxial layer is reduced during the device process. The CH₃O ion implantation reduced the O concentration to 3.8×10^{13} atoms/cm² in the epitaxial layer (Figure 5.9). This reduction was achieved by the O gettering in the CH₃O ion-implantation region. As shown in Figure 5.8, the CH₃O ion-implantation region can getter O that diffused from the Si substrate during the device heat treatment. The O in the device structure region accounts for the lag characteristics of CMOS image sensors [66]. Furthermore, Kaneda and Ohtani reported that the O–B complex generates an energy level in Si band gaps [65]. B is used to form the p-type region in device structures such as PDs. Thus, it is considered that the O concentration reduction reduces the white spot defect density via the reduction in the concentration of the O–B complex.

Third, H gettering occurs in the CH₃O ion-implantation region. In general, the Si/SiO₂ interface state defects form the electrical state in Si crystal band gaps. This electrical state easily forms holes and electrons by thermal energy without photo irradiation. As a result, the Si/SiO₂ interface state defects increases the density of white spot defects.

As shown in Figure 5.10, the concentration of H that diffused during the device process was 7.4×10^{12} atoms/cm². In general, the density of Si/SiO₂ interface states is almost 10^{11} atoms/cm². Although the amount of H that diffused was higher by a factor of 10 than that of the density of Si/SiO₂ interface state defects, we assumed that the amount of H was sufficient to passivate the Si/SiO₂ interface. It is expected that H that diffused from the CH₃O ion-implantation region passivated the interface state defect formed in device structures, such as the Si/SiO₂ interface.

In conclusion, it is considered that white spot defect density reduction was achieved through these three mechanisms, accounting for the high gettering capability of the CH₃O ion-implantation region for metallic impurities.

5.5 Conclusion

In this chapter, we compared the gettering capability of CH₃O and C₂H₃ ion-implantation regions, and also discussed the effect of the proximity gettering technique using CH₃O ion implantation on the characteristics of the CMOS image sensor performance. The results are summarized as follows:

1. The gettering capability of the CH₃O ion-implantation region on Ni was higher than that of the C₂H₃ ion-implantation region. This increase in gettering capability is assumed to be due to the formation of EOR defects, which do not form in the ion-implantation region with a hydrocarbon molecule such as C₂H₃.
2. The CH₃O ion-implantation region after the device fabrication process can getter the metals Ni, Cu, and Fe. This result suggests that the gettering site introduced by CH₃O ion implantation acts as a strong gettering site for the metallic impurity contaminations during device fabrication processes.
3. The behavior of the defect introduced by CH₃O ion implantation during the device fabrication process was investigated. It is found that the defect remained through the fabrication process, and it is assumed that these defects also act as gettering sites during the device fabrication process.
4. We analyzed the distribution of C and O atoms in the CH₃O ion-implantation region close to and far from the EOR defects. It is found that the EOR defects in the CH₃O ion-implantation region function as a gettering site on O more strongly than do C-related defects. From this result, it is assumed that EOR defects act as strong gettering sinks on other elements such as metallic impurity contaminations.
5. The density of white spot defects can be decreased using CH₃O ion-implanted Si epitaxial wafers. This result suggests that CH₃O ion implantation could contribute to

improving the characteristics of advanced CMOS image sensors and that the concept of the proximity gettering using multi-element molecular ion implantation is effective.

Chapter. 6

Conclusions

In this thesis, we developed a new molecular ion implantation technology, namely “CH₃O ion implantation technology” for proximity gettering, and we investigated the basic characteristics of an Si epitaxial wafer implanted by the CH₃O molecular ion. Furthermore, we also investigated whether proximity gettering technology using CH₃O ion implantation can improve the CMOS image sensor’s electrical performance.

In Chapter 2, the principles of the equipment and analysis methods that were used in this thesis were described. In particular, the ion implantation apparatus “CLARIS®” was described; it uses organic molecules as the gas source and ionizes the gas by electron impact for the formation of a molecular ion beam.

In Chapter 3, multi-element molecular ion beam formation and the characteristics of CH₃O ion implantation were studied. Molecular ions, such as the CH₃O ion, which is assumed to consist of three elements, is formed by the ionization of diethyl ether using electron impact. The ion with mass 31 was selected for implantation, and was assumed to have the formula CH₃O. Using the ion of mass number 31, we observed in the ion implantation region the concentration peaks of C, H, and O. From this result, we determined that CH₃O ion implantation can be performed using diethyl ether as the gas source. We also investigated the implantation damage of CH₃O ion implantation using TEM. The implantation damage was higher for implantation with the CH₃O ion than with the C₂H₃ ion. We revealed from TCAD calculation that the increase in CH₃O ion implantation damage was caused by the added O. The damage trend of CH₃O ion

implantation was the same as that of C_2H_3 ion implantation, which is the conventional hydrocarbon molecular ion implantation. This result suggests that CH_3O ion implantation can be applied to the fabrication process of hydrocarbon molecular ion-implanted Si epitaxial wafers. From these studies, we investigated that CH_3O ion implanted Si epitaxial wafer is able to fabricate using the fabrication process on the hydrocarbon molecular ion implanted Si epitaxial wafer.

In Chapter 4, the fundamental characteristics of CH_3O ion-implanted Si epitaxial wafers were studied. We found that the CH_3O ion implantation region contains two types of defects. One type of defect is a 5 nm black point defect, which was also observed in the hydrocarbon molecular ion implantation region. This defect is considered to be formed by the aggregation of implanted C. The other defect is a 50 nm defect, which is peculiar to the CH_3O ion implantation region and was never observed in the hydrocarbon molecular ion implantation region. From TEM observations and FFT analysis of the defect, we found that the 50 nm defect is an EOR defect, which has the shape of a stacking fault defect formed by the aggregation of interstitial Si. Because the interstitial concentration at the EOR of CH_3O ion implantation is higher than that of C_2H_3 ion implantation, we concluded that 50 nm defects were formed by the aggregation of interstitial Si that increased with the added O in CH_3O ion implantation. The dependence of the EOR defect density in the CH_3O ion implantation region on the ramping-up rate after annealing at 1100 °C for 300 s was also investigated. We conclude that the dependence on the density of the EOR defect was caused by the temperature dependence of the behavior of the EOR defect. The aggregation behavior of interstitial Si and the gettering behavior of C and O at the EOR defect were considered to be determined by the

temperature dependence of the EOR defect formation behavior and the dependence of the EOR defect density on the ramping-up rate.

In Chapter 5, the gettering capability of the CH₃O ion implantation region and the effect of the CH₃O ion-implanted Si epitaxial wafer on a CMOS image sensor were studied. The Ni gettering test results of the CH₃O ion-implanted Si epitaxial wafer suggest that the gettering capability of the CH₃O ion-implanted region was higher than that of the C₂H₃ ion-implanted region. We consider that the gettering capability was increased by the EOR defect acting as gettering sinks in the CH₃O ion-implanted region.

Finally, we investigated the effect of proximity gettering technology using CH₃O ion implantation technology. The gettering capability of the CH₃O ion-implanted region was found to be effective in metallic impurity contaminations such as Ni, Cu, and Fe introduced during the CMOS image sensor fabrication processes. We also found that the white spot defect could decrease using CH₃O ion-implanted Si epitaxial wafers. This result suggests that CH₃O ion-implanted Si epitaxial wafers can improve the electrical properties of CMOS image sensors.

From the studies in this thesis, we found that our new molecular ion implantation technology for proximity gettering technology was effective for the improvement of CMOS image sensor device performance. We believe that multi-element molecular ion implantation can contribute to advanced CMOS image sensors.

References

- [1] M. A. Schuster and G. Strull, *IEE Trans. Electron Devices* **13**, 906 (1966).
- [2] W. S. Boyle and G. E. Smith, *Bell Syst. Tech. J.* **49**, 587 (1970).
- [3] 米本 和也 : 改訂 CCD/CMOS イメージセンサの基礎と応用 (CQ 出版社, 2018).
- [4] Marc Loinaz, Kanwar Jit Singh, Andrew J. Blanksby, David A. Inglis, Kamran Azadet, and Bryan D. Ackland, *ISSCC Dig. Technical Papers*, 168 Feb. (1998).
- [5] 相澤 清晴, 江木 雄一郎, 浜本 隆之, 羽鳥 光俊, 丸山 裕孝, 大竹 浩, 瀧口 吉郎, 阿部 正英, *映像情報メディア学会*, **51**, 2, 270 (1997).
- [6] S. Kawahito, M. Yoshida, M. Sasaki, K. Umehara, Y. Tadokoro, K. Murata, S. Doushod, and A. Matsuzawa, *ISSCC Dig. Technical Papers*, 184, Feb (1997).
- [7] W.T. Freeman, D.B. Anderson, P. Beardsley, C.N. Dodge, M. Roth, C.D. Weissman, W.S. Yerazunis, H. Kage, I. Kyuma, Y. Miyake, and K. Tanaka, *IEEE Computer Graphics and Applications*, **18**, 3, 42 (1998).
- [8] T. Sugiyama, S. Yoshimura, R. Suzuki, and H. Sumi, *ISSCC Dig. Technical Papers*, 434, Feb (2002).
- [9] S. Iwabuchi, Y. Maruyama, Y. Ohgishi, M. Muramatsu, N. Karasawa, and T. Hirayama, *ISSCC Dig. Technical Papers*, 302, Feb (2006).
- [10] S. Yoshihara, Y. Nitta, M. Kikuchi, K. Koseki, Y. Ito, Y. Inada, S. Kuramochi, H. Wakabayashi, M. Okano, H. Kuriyama, J. Inutsuka, A. Tajima, T. Nakajima, Y. Kudoh, F. Koga, Y. Kasagi, S. Watanabe, and T. Nomoto, *ISSCC Dig. Technical Papers*, 492, Feb (2006).
- [11] M. H. White, D. R. Lampe, F. C. Blaha, and I. A. Mack, *IEEE, J. Solid-State Circuits* SC-9, 1 (1974).

- [12] 寺西信一, 河野明啓, 織田英嗣, 新井浩一, 石原保雄, テレビジョン学会 45 (1981).
- [13] 三村秀典, 原和彦, 川人祥二, 青木徹, 廣本宣久 : ナノビジョンサイエンス (コロナ社, 2009)
- [14] A. Aenov, R. Balasubramaniam, A. R. Brown, and J. H. Davies, IEEE Trans. Electron Devices **50** 839 (2003).
- [15] 志礼拓磨, 徐成昊, 伊藤真也, 川人祥二 : テレビジョン学会 **32**, 37 (2008).
- [16] S. Kawahito and N. Kawai, in Proc. International Image Sensors Workshop, 226 (2007).
- [17] 高橋秀和, 映像情報メディア学会誌 **62**, 303 (2008).
- [18] K. Yonemoto, T. Iizuku, S. Nakamura, K. Harada, K. Wada, M. Negishi, H. Yamada, T. Tsunakawa, K. Shinohara, T. Ishimaru, Y. Kamide, T. Yamasaki, M. Yamagishi, ISSCC Dig. Tech. Papers, 214, (1990).
- [19] N. Teranishi, A. Kohono, Y. Ishihara, E. Oda, K. Arai, IEDM Tech. Dig., 324 (1982)
- [20] C. Claeys and E. Simoen, *Metal Impurities in Silicon-and Germanium-Based Technologies* (Springer, Switzerland, 2018), Chap. 7, p. 332.
- [21] E. R. Weber, Appl. Phys A. **30**, 1 (1983).
- [22] A. A. Istratov and E. R. Weber, Appl. Phys A. **66**, 123 (1998).
- [23] J. Nakamura, *Image sensors and signal processing for digital still cameras* (CRC Press, Tokyo, 2006)
- [24] 佐藤 信彦 : 第 78 回応用物理学会秋季学術講演会, 5p-A204-9 (2017)
- [25] J. S. Kang and D. K. Schroder, J. Appl. Phys. **65**, 2974 (1989).
- [26] 志村 史夫 : 半導体シリコン結晶工学 (丸善株式会社, 1993)
- [27] D. Gilles, E. R. Weber, and S. Hahn, Phys. Rev. Lett. **64**, 196 (1990).

- [28] M. Aoki, A. Hara, and A. Ohsawa, *J. Appl. Phys.* **72**, 895 (1992).
- [29] G. A. Rozgonyi, P.M. Petroff, and M. H. Read, *J. Electrochem. Soc.* **122**, 1725 (1975).
- [30] C. M. Hsieh, J. R. Mathews, H. D. Seidel, K. A. Pickar, and C. M. Drum, *Appl. Phys. Lett.*, **22**, 238 (1973).
- [31] R. A. Logan and M. Schwartz, *J. Appl. Phys.*, **26**, 1287 (1995).
- [32] R. L. Meek and T. E. Seidel, *J. Phys. Chem. Solids* **36**, 731 (1975).
- [33] E. J. Mets, *J. Electrochem. Soc.* **112**, 420 (1965).
- [34] T. E. Seidel, R. L. Meek, and A. G. Cullis, *J. Appl. Phys.*, **46**, 600 (1975).
- [35] C. W. Pearce and V. J. Zaleckas, *J. Electrochem. Soc.* **126**, 1436 (1979).
- [36] G. A. Rozgonyi and R. A. Kushner, *J. Electrochem. Soc.* **123**, 570 (1976).
- [37] M. C. Chen and V. J. Silverstri, *J. Electrochem. Soc.* **129**, 1294 (1982).
- [38] A. S. Salih, H. J. Kim, R. F. Davis, and G. A. Rozgonyi, *Appl. Phys. Lett.*, **46**, 419 (1985).
- [39] P. H. Robinson and F. P. Heiman, *J. Electrochem. Soc.*, **118**, 141 (1971).
- [40] S. Kishino, K. Nagasawa, and T. Iizuka, *Jpn. J. Appl. Phys.*, **19** L466 (1980)
- [41] K. Nagasawa, Y Matsushita, and S. Kishino, *Appl. Phys. Lett.* **37**, 622 (1980)
- [42] S. M. Hu, *J. Appl. Phys.*, **52**, 3974 (1981)
- [43] M. Aoki, A. Hara, and A. Ohsawa, *J. Appl. Phys.* **72**, 895 (1992).
- [44] T. Y. Tan, E. E. Garner, and W. K. Tice, *Appl. Phys. Lett.* **30**, 175 (1977)
- [45] M. Hourai, K. Murakami, T. Shigematsu, N. Fujino, and T. Shiraiwa, *Jpn. J. Appl. Phys.*, **28**, 2413 (1989).
- [46] H. Hiesimair, A. A. istratov, S. A. Mchugo. C. Flink, and E. R. Weber, *J. Electrochem. Soc.*, **145**, 4259 (1998).
- [47] K. Sueoka, S. Sadamitsu, Y. Koike, T. Kihara, *J. Electrochem. Soc.* **147**, 3074 (200).

- [48] 株式会社 SUMCO : 固体撮像素子用半導体基板およびその製造方法, 特許 4650493.
- [49] 中居克彦 : 最新シリコンデバイスと結晶技術, 清水博文(編集) (REALIZE, 2005).
- [50] T. Kuroi, Y. Kawasaki, S. Komori, M. Inuishi, K. Tsukamoto, H. Shinyashiki, and T. Shingyoji, *Jpn. J. Appl. Phys.* **32**, 303 (1993).
- [51] ソニー株式会社 : 半導体基板、固体撮像素子及びこれらの製造方法, 特開平 06-338507.
- [52] ソニー株式会社 : 固体撮像素子の製造方法、及び半導体基板の製造方法, 特許 4613886, 2010-10-29.
- [53] 信越半導体株式会社 : エピタキシャルウェーハの製造方法およびエピタキシャルウェーハ, 特開 2008-294245.
- [54] 栗田一成 : 応用物理 **84**, 628 (2015)
- [55] 栗田一成, 門野武, 奥山亮介, 廣瀬諒, 梶田亜由美, 奥田秀彦, 古賀祥泰, 表面化学 37, 104 (2016)
- [56] K. Kurita, T. Kadono, R. Okuyama, R. Hirose, A. Onaka-Masada, Y. Koga, and H. Okuda, *Jpn. J. Appl. Phys.* **56**, 049201 (2017).
- [57] K. Kurita, T. Kadono, R. Okuyama, S. Shigematsu, R. Hirose, A. Onaka-Masada, Y. Koga, and H. Okuda. *Phys. Status Solidi A*, “14, 1700216 (2017).
- [58] K. Kurita, T. Kadono , R. Okuyama, R. Hirose, A. Onaka-Masada, Y. Koga and H. Okuda, *Sensors* 2019, 19(9), 2073 (2019).
- [59] R. Okuyama, A. Onaka-Masada, S. Shigematsu, T. Kadono, R. Hirose, Y. Koga, H. Okuda, and K. Kurita, *Jpn. J. Appl. Phys.* **57**, 081302 (2018).
- [60] R. Okuyama, T. Kadono, A. Masada, R. Hirose, Y. Koga ,H. Okuda, and K. Kurita,

- Jpn. J. Appl. Phys. **56**, 025601 (2017).
- [61] R. Okuyama, S. Shigematsu, R. Hirose, A. Masada, T. Kadono, Y. Koga, H. Okuda, and K. Kurita, Phys Status Solidi C, 1700036(2017).
- [62] I. Yamada, *Materials Processing by Cluster Ion Beams, History, Technology, and Applications*, (CRC Press, Tokyo, 2015).
- [63] I. Yamada, J. Matsuo, N. Toyoda, and A. Kirkpatrick, Mater. Sci. Eng. R **34**, 231 (2001).
- [64] M. Tanjyo, N. Hamamoto, T. Nagayama, S. Umisedo, Y. Koga, N. Maehara, H. Une, T. Matsumoto, N. Nagai, and J. O. Borland, ECS Trans. **18** [1] 1059 (2009)
- [65] T. Kaneda and A. Ohtani, Ext. Abstr. (77th Autumn Meet. 2016); Japan Society of Applied Physics and Related Societies, 14p-P6-10 [in Japanese].
- [66] A. Ohtani and T. Kaneda, Ext. Abstr. (77th Autumn Meet. 2016); Japan Society of Applied Physics and Related Societies, 14p-P6-11 [in Japanese].
- [67] S.M Sze, Semiconductor Devices, Physics and Technology, 2nd Ed. (John Wiley & Sons, 2002), p.182. (Chapter 6).
- [68] X. W. Wang and T. P. Ma, Appl. Phys. Lett. **60**, 2634 (1992)
- [69] Y. Nishioka, K. Ohyu, Y. Ohji, N. Natsuaki, and K. Mukai, J. Appl. Phys, **66**, 3909 (1989)
- [70] H. N. Chern, C. L. Lee, T. F. Lei, IEEE Trans. Elec. Device., **41**, 5, (1994)
- [71] S. Shirasawa, K. Sueoka, T. Yamaguchi, and K. Maekawa: J. Electrochemica. Soc. **4**, 351 (2015).
- [72] S. Shirasawa, K. Sueoka, T. Yamaguchi, and K. Maekawa: Ext. Abstr. (76th Autumn Meet. 2015); Japan Society of Applied Physics and Related Societies, 14p-PB7-2, 2015 [in Japanese].

- [73] S. Shirasawa, K. Sueoka, T. Yamaguchi, and K. Maekawa: Mater. Sci. Semicond. Process. **44**, 13 (2016).
- [74] J. F. Ziegler edit: “ION IMPLANTATION APPLICATIONS, SCIENCE AND TECHNOLOGY Edition: 2016”, (Ion Implantation Technology Co., 2016).
- [75] 伊藤糾次, 鶴島稔夫, 谷口和雄, 大泊巖: イオン・インプラントレーション-理論と応用-, (昭晃堂, 1976).
- [76] 難波進: エレクトロニクス技術全書 8 イオン注入技術, (工業調査会, 1975).
- [77] N. Hamamoto, S. Umisedo, N. Maehara, Y. Kawamura, Y. Nakashima, Y. Hashino, Y. Koga, H. Une, M. Tanjyo, T. Nagayama, H. Onoda, Development of new cluster Ion Implanter “CLARIS” 日新電機技報 **54**, 2, (2009).
- [78] 日本表面化学会編: 二次イオン質量分析法 (丸善, 1999).
- [79] 片岡祐次, 応用物理 **79**, 321 (2010).
- [80] 松尾二郎, 応用物理 **79**, 326 (2010).
- [81] 大見忠弘, 新田雄久: シリコンの科学 (REALIZE, 1996).
- [82] 田中信夫: 走査透過顕微鏡の物理 (共立出版, 2018).
- [83] 堀内繁雄: 高分解能電子顕微鏡 (共立出版, 1988).
- [84] D. Blavette, E. Cadel, A. Fraczkiewicz, and A. Menand, Science **286**, 2317 (1999).
- [85] M. K. Miller and R. G. Forbes: *Atom-Probe Tomography: The Local Electrode Atom Probe* (Springer, 2014).
- [86] 宝野和博, 応用物理 **79**, 317 (2010).
- [87] K. Thompson, P. L. Flaitz, P. Ronsheim, D. J. Larson, and T. F. Kelly, Science **317**, 1370 (2007).
- [88] S. Dugury, T. Philippe, F. Cristiano, and D. Blavette, Appl. Phys. Lett., **97**, 242104 (2010).

- [89] K. Hoummda, D. Mangelinck, B. Gault, and M. Cabié, *Scr. Mater.* **64**, 378 (2011).
- [90] A. Vella, B. Mazumder, G. Da. Costa, and B. Deconihout, *J. Appl. Phys.*, **110**, 044521 (2011).
- [91] A. Cerezo and G. D. W. Smith, *Appl. Phys. Lett.*, **88**, 154103 (2006).
- [92] 大久保忠勝, Y. Chen, 小塚雅也, 宝野和博, *まてりあ* **50**, 397 (2011).
- [93] M. Morita, M. Karasawa, T. Asaka, and M. Owari, *J. Surf. Aneal.* **20** 177 (2014).
- [94] Y. Shimizu, K. Inoue, H. Takamizawa, F. Yano, and Y. Nagai, *J. Vac. Soc. Jpn.* **56**, 340 (2013) [in Japanese].
- [95] R. M. Silverstein, F. X. Webster, and D. J. Kiemle : *Spectrometric Identification of Organic Compounds Seventh Edition* (Wiley 2005)
- [96] 石川 順三 : *荷電粒子ビーム工学* (コロナ社, 2001)
- [97] 藤本文範, 小牧 研一郎 : *イオンビーム工学—イオン・固体相互作用編* (内田老鶴圃, 1995)
- [98] R. Okuyama, A. Masada, S. Shigematsu, T. Kadono, R. Hirose, Y. Koga, H. Okuda and K. Kurita, *Jpn. J. Appl. Phys.*, **57**, 011301 (2018)
- [99] Synopsys Sentaurus Process User's Manual, Release J-2014.09 (Synopsys Inc., Zurich, 2014).
- [100] D. Pomerantz, *J. Appl. Phys.*, **38**, 5020 (1967).
- [101] M. Nakamura, T. Kato, and N. Oi, *Jpn. J. Appl. Phys.*, **7** 512 (1968).
- [102] K. S. Jones and G. A. Rozgony, *Rapid Thermal Processing, Science and Technology* (Academic Press, 2012) Chap. 5, p. 123.
- [103] R. B. Fair, *Rapid Thermal Processing, Science and Technology* (Academic Press, 2012)
- [104] C. Bonafos, D. Mathiot, and A. Claverie, *J. Appl. Phys.* **83**, 3008 (1998).

- [105] H. Wong, N. W. Cheung, P. K. Chu, J. Liu, and J. W. Mayer, *Appl. Phys. Lett.* **52**, 1023 (1988)
- [106] M. Tamura, *Appl. Phys. Lett.* **23**, 651 (1973)
- [107] M. Tamura and T. Suzuki, *Nuclear Instruments and Methods in Physics Research*, **B39**, (1989), 318-329.
- [108] H. Wong, N. W. Cheung, P. K. Chu, J. Liu, and J. W. Mayer, *Appl. Phys. Lett.* **52** (1988) 1023.
- [109] T. J. Magee, C. Leung, H. Kawayoshi, R. Ormond, B. K. Furman, C. A. Evans, Jr. and D. S. Day, *Appl. Phys. Lett.* **39** (1981) 413.
- [110] F. Russo, G. Moccia, G. Nardone, R. Alfonsetti, G. Polsinelli, A. D'Angelo, A. Patacchiola, M. Liverani, P. Pianezza, T. Lippa, M. Carlini, M.L. Polignano¹, I. Mical¹, E. Cazzini¹, M. Ceresoli¹, and D. Codegoni¹, *Solid-State Electron*, **91** 91 (2014).
- [111] F. Russo, G. Nardone, M. L. Polignano, A. D'Ercole, F. Pennella, M.D.Felice, A.D. Monte, A. Matarazzo, G. Moccia, G. Polsinelli, A. D'angelo, M. Liverani, and F. Irrera, *ECS J. Solid State Sci. Techn.*, **6**, 217 (2017).
- [112] T. Yamaguchi, T. Yamashita, T. Kamino, Y. Goto, T. Kuroi, and M. Matsuura, 2016 IEEE Symposium on VLSI Technology.
- [113] T.Yamaguchi, T.Kamino, Y.Goto, M.Kimura, M.Inoue and M.Matsuura: The 8th Forum on the Science and Technology of Silicon Materials 2018, S6-3.
- [114] H. Takahashi, M. Kinoshita, K. Morita, T. Shirai, T. Sato, T. Kimura, H. Yuzurihara, and S. Inoue: *ISSCC Dig. Tech. Pap.* **78**, (2004).
- [115] M. Mori, M. Katsuno, S. Kasuga, T. Murata, and T. Yamaguchi: *ISSCC Dig. Tech. Pap.* **80**, (2004).

- [116] L. Baldi, G. F. Cerofolini, G. Ferla, and G. Frigerio, *Phys. Status Solidi* **48**, 525 (1978).
- [117] K. Kurita, T. Kadono, R. Okuyama, R. Hirose, A. Onaka-Masada, Y. Koga, and H. Okuda: *Jpn. J. Appl. Phys.* **55**, 121301 (2016).
- [118] F. Russo, G. Moccia, G. Nardone, R. Alfonsetti, G. Polsinelli, A. D'Angelo, A. Patacchiola, M. Liverani, P. Pianezza, T. Lippa, M. Carlini, M.L. Polignano¹, I. Mical¹, E. Cazzini¹, M. Ceresoli¹, and D. Codegoni¹, *Solid-State Electron*, **91** 91 (2014).
- [119] F. Russo, G. Nardone, M. L. Polignano, A. D'Ercole, F. Pennella, M.D.Felice, A.D. Monte, A. Matarazzo, G. Moccia, G. Polsinelli, A. D'angelo, M. Liverani, and F. Irrera, *ECS J. Solid State Sci. Techn.*, **6**, 217 (2017).

List of Figures

Fig. 1.1. Schematic diagrams of the image sensor system (a) CCD, (b) CMOS

Fig. 1.2. Schematic diagram of the PD

Fig. 1.3. Temperature dependence of dark current [23]

Fig. 1.4. Schematic diagram of each gettering technology: (a) EG, (b) IG, and (c) proximity gettering

Fig. 1.5. Schematic diagram of the manufacturing process of hydrocarbon molecular ion implanted Si epitaxial wafers

Fig. 1.6. Concept of multi-element molecular ion implantation technology

Fig. 2.1. Schematic diagram of the ion implantation apparatus

Fig. 2.2. Schematic diagram of the SIMS analytical instrument [73]

Fig. 2.3. Schematic diagram of secondary ion formation in SIMS analysis [73]

Fig. 2.4. Schematic diagram of TEM analysis [81]

Fig. 2.5. Imaging principle of TEM analysis [81]

Fig. 2.6. Schematic diagram of 3D-APT analysis [93]

Fig. 3.1. Mass spectrum of molecular ions obtained by ionization of diethyl ether

Fig. 3.2. SIMS depth distribution of C, H, and O after CH₃O ion implantation

Fig. 3.3. ϵ dependence of nuclear stopping cross section [97].

Fig. 3.4. Cross-sectional image of CH₃O molecular ion-implanted region.

The molecular ion dose [molecular ions/cm²] was

(a) 5.0×10^{14} , (b) 1.0×10^{15} , (c) 1.5×10^{15} , and (d) 2.0×10^{15} .

Fig. 3.5. Cross-sectional TEM image of the molecular ion-implanted region with a dose of 1×10^{15} [molecular ions/cm²]

(a) CH₃O-ion-implanted wafer, (b) C₂H₃-ion-implanted wafer

Fig. 3.6. Distribution depth profiles of C, H, and O and damage calculated using TCAD simulation

Fig. 4.1. Sample preparation flow of molecular ion-implanted Si epitaxial wafer

Fig. 4.2. Profiles of various RTA processes at different rates, as shown

Fig. 4.3. Cross-sectional TEM images of CH₃O ion implantation region.

The implantation doses were (a) 5.0×10^{14} , (b) 7.5×10^{14} , (c) 1.0×10^{15} , and (d) 2.0×10^{15} ions/cm². The implantation energy was 80 keV

Fig. 4.4. Clear resolution cross-sectional TEM image of the CH₃O ion implantation region. The ion dose was 1.0×10^{15} ions/cm²

Fig. 4.5. High-resolution cross-sectional TEM image of 50 nm defects in CH₃O ion implantation region. (a) Overall image of the 50 nm defects; (b) expansion image of 50 nm defects; (c) FFT

Fig. 4.6. Depth distribution profiles of C, H, and O in CH₃O ion-implanted epitaxial wafer obtained using SIMS. The blue line is C, the black line is H, and the red line is O

Fig. 4.7. O distribution profiles of CH₃O and C₂H₃ ion-implanted Si epitaxial wafers. The red line is the CH₃O ion-implanted Si epitaxial wafer, and the black line is the C₂H₃ ion-implanted one. The epitaxial thickness was 9 μm

Fig. 4.8. Cross-sectional TEM images of CH₃O ion-implanted region after (a) CH₃O ion implantation and (b) RTA

Fig. 4.9. Profiles of damage concentration generated by CH₃O ion implantation calculated by TCAD simulation

Fig. 4.10. TEM images of CH₃O ion-implanted region after RTA at 1100 °C for 300 s, at ramping-up rates of (a) 4, (b) 8, (c) 15, (d) 60 °C/s

Fig. 4.11. Dependence of density of CH₃O ion-implanted defects on ramping-up rate

Fig. 4.12. Dependence of density of CH₃O ion-implanted defects on ramping-up rate and annealing time

Fig. 4.13. SIMS analysis results of CH₃O ion-implanted region after RTA treatment. Depth profiles of (a) C and (b) O concentrations

Fig. 4.14. TEM images of CH₃O ion-implanted region after RTA for 300 s at (a) 800, (b)

900, (c) 1000, and (d) 1100 °C

Fig. 4.15. TEM images of CH₃O ion-implanted region after 900 °C RTA for annealing duration of (a) 0, (b) 60, and (c) 300 s

Fig. 4.16. Schematic images of formation behavior of CH₃O ion implantation defects at ramping-up rates of (a) 4, (b) 15, and (c) 60 °C/s

Fig. 5.1 SIMS depth profiles measured on a CH₃O ion-implanted epitaxially grown sample after Ni metallic-impurity contamination. The black, blue, and orange lines are the distribution profiles of C, O, and Ni, respectively.

Fig. 5.2 SIMS depth profiles of Ni metallic-impurity contamination in CH₃O (red line) and C₂H₃ (black line) ion-implanted epitaxially grown samples

Fig. 5.3 Comparison of Ni gettering efficiency in C₂H₃ and CH₃O ion-implantation regions

Fig. 5.4 SIMS depth profiles of C and O measured on CH₃O and C₂H₃ ion-implanted epitaxially grown samples after Ni metallic-impurity contamination. Black and gray lines are C distribution profiles for the CH₃O and C₂H₃ samples, respectively; dark blue and light blue lines are O distribution profiles for the CH₃O and C₂H₃ samples, respectively

Fig. 5.5 SIMS depth profiles of C, O, H, Ni, and Cu after the device process

Fig. 5.6 Ni distribution profiles in the CH₃O ion-implanted wafer (a) before and (b) after the device process

Fig. 5.7 C distribution profiles in CH₃O ion-implanted and unimplanted wafers (a) before and (b) after device process

Fig. 5.8 O distribution profiles of CH₃O ion-implanted and unimplanted wafers (a) before and (b) after device process

Fig. 5.9 O concentrations in epitaxial layer of wafers with and without CH₃O ion

implantation before and after the device process

Fig. 5.10 H distribution profiles before and after the device process

Fig. 5.11 BMD densities in CH₃O ion-implanted and unimplanted wafers

Fig. 5.12 Cross-sectional TEM images of CH₃O ion-implantation region (a) before and (b) after the device process

Fig. 5.13 C-related defect densities before and after the device process

Fig. 5.14 Cross-sectional SEM images of needle-shaped samples and 3D-APT analysis results of atom maps and isoconcentration surfaces at 2.0 at.% C and 5.0 at.% O on C-related defects in the CH₃O ion-implantation region (a) before and (b) after the device process

Fig. 5.15 Cross-sectional STEM images of needle-shaped samples and 3D-APT analysis results of atom maps and isoconcentration surfaces at 2.0 at.% C and 10 at.% O on stacking fault defects in the CH₃O ion-implantation region (a) before and (b) after the device process

Fig. 5.16. The number of oxygen atoms gettered by the C-related and EOR defect

Fig. 5.17. The concentration of the oxygen gettered by C-related and EOR defects.

Fig. 5.18. The comparison of gettered oxygen concentration between the 3D-APT results and the SIMS results.

Fig. 5.19 Density of white spot defects in wafers with and without CH₃O ion implantation

List of Publications

Full Length Papers

(1) Proximity gettering of silicon wafers using CH₃O multi-element molecular-ion-implantation technique” (Chppter. 3·4·5)

R. Hirose, T. Kadono, R. Okuyama, S. Shigematsu, A. Onaka-Masada, H. Okuda, Y. Koga, and K. Kurita

Japanese J. Appl. Phys.57.096503(2018)

(2) Effect of ramping-up rate on end of range defect in multielement molecular-ion (CH₃O)-implanted silicon wafer” (Chppter. 3·4)

R. Hirose T. Kadono, R. Okuyama, A. Onaka-Masada, S. Shigematsu, K. Kobayashi, Y. Koga, and K. Kurita

Japanese J. Appl. Phys.58. 121002 (2019)

(3) Proximity gettering technique using CH₃O multi-element molecular ion implantation for white spot defect density reduction in CMOS image sensor” (Chppter. 5)

R. Hirose, T. Kadono, R. Okuyama, A. Onaka-Masada, S. Shigematsu, K. Kobayashi, Y. Koga, and K. Kurita

Japanese J. Appl. Phys. 58.091002(2019)

(4) Proximity Gettering of Carbon Cluster Ion Implanted Silicon Wafers for CMOS Image Sensors“

- Gettering Effects of Transition Metal, Oxygen, and Hydrogen Impurities –

K. Kurita, T. Kadono , R. Okuyama, R. Hirose, A. Onaka-Masada, Y. Koga and H. Okuda

Japanese J. Appl. Phys. 55(2016) 121301(7pp)

DOI: 10.75671/JJAP.57.121301

(5) Trapping and diffusion kinetic of hydrogen in carbon-cluster ion-implantation projected range in Czochralski silicon wafers

R. Okuyama , A. Onaka-Masada , T. Kadono , R. Hirose, Y. Koga ,H. Okuda and K. Kurita

Japanese J. Appl. Phys. 56(2017) 025601(6pp)

(6) Trapping and diffusion behaviour of hydrogen simulated with TCAD in projection range of carbon-cluster implanted silicon epitaxial wafers for CMOS image sensors

R. Okuyama , A. Onaka-Masada , T. Kadono , R. Hirose, Y. Koga ,H. Okuda and K. Kurita

Physica Status Solidi C: Current Topics in Solid State Physics,1700036(2017)

(7) Proximity gettering technology for advanced CMOS image sensors using carbon cluster ion-implantation technique: A review

K. Kurita, T. Kadono , R. Okuyama , R. Hirose, A. Onaka-Masada, Y. Koga and H. Okuda

Physica Status Solidi A ,1700216(2017)

(8) Defect Engineering on Dose and Size in Carbon Cluster Implanted Silicon Wafers

R. Okuyama , A. Onaka-Masada , T. Kadono , R. Hirose, Y. Koga ,H. Okuda and K. Kurita

Japanese J. Appl. Phys. 57,011301(2018)

(9) Effect of low oxygen concentration on iron gettering capability in carbon-cluster ion implanted Si wafer for CMOS image sensor

A. Onaka-Masada, T. Nakai, R. Okuyama, H. Okuda, T. Kadono, R. Hirose, Y. Koga, K. Kurita, and K. Sueoka

Japanese J. Appl. Phys.57, 021304 (2018)

(10) Room-temperature bonding of epitaxial layer to carbon-cluster-ion-implanted silicon wafers for CMOS image sensors

Y. Koga, T. Kadono, S. Shigemastu, R. Hirose, A. Onaka-Masada, R. Okuyama, H. Okuda, K. Kurita

Japanese J. Appl. Phys. 57,061302(2018)

(11)” Diffusion kinetic of hydrogen in silicon wafer implanted with CH₃O molecular ions for CMOS image sensors”

R. Okuyama, A. Masada, S. Shigematsu, T. Kadono, R. Hirose, Y. Koga, H. Okuda, and K. Kurita

Japanese J. Appl. Phys.57.081302(2018)

(12)”Gettering mechanism in hydrocarbon-molecular ion-implanted epitaxial silicon wafers revealed by three-dimensional atom imaging”

A. Onaka-Masada, T. Nakai, R. Okuyama, H. Okuda, T. Kadono, R. Hirose, Y. Koga, K. Sueoka and K. Kurita

Japanese J. Appl. Phys.57.091302(2018)

(13)” Gettering Sinks for Metallic Impurities Formed by Carbon-cluster Ion Implantation in Epitaxial Silicon Wafers for CMOS Image Sensor”

A. Onaka-Masada, T. Nakai, R. Okuyama, H. Okuda, T. Kadono, R. Hirose, Y. Koga, K. Sueoka and K. Kurita

IEEE Journal of the Electron Devices Society, 6, 1200 (2018)

(14)” Proximity Gettering Design of Hydrocarbon Molecular Ion Implanted Silicon Wafers using Direct Bonding Technique for Advanced CMOS Image Sensors”:

K. Kurita, Y. Koga, R. Okuyama ,T. Kadono, S. Shigematsu, A. Onaka-Masad, R. Hirose and H. Okuda

“Semiconductor Wafer Bonding: Science, Technology, and Applications 15”

ECS Transactions, Volume 86, (5)77-93(2018).

DOI:10.1149/08605.007ecst

(15)” Proximity Gettering Design of Silicon Wafers using Hydrocarbon Molecular Ion Implanted Silicon Wafers for CMOS Image Sensors”

K. Kurita, T. Kadono , R. Okuyama, R. Hirose, A. Onaka-Masada, Y. Koga and H. Okuda

Sensors 2019, 19(9), 2073.

(16) "A Review of Proximity Gettering Technology for CMOS image sensors using Hydrocarbon Molecular Ion Implanted Silicon Wafers for CMOS Image Sensors"
K. Kurita, T. Kadono, R. Okuyama, R. Hirose, A. Onaka-Masada, Y. Koga and H. Okuda
Sensors and Materials, Vol.31, No.6 (2019) 1939-1955.

(17) "Molecular and atomic hydrogen diffusion behavior by reaction kinetic analysis in projection range of hydrocarbon molecular ion for CMOS image sensors"
R. Okuyama, A. Masada, S. Shigematsu, T. Kadono, R. Hirose, Y. Koga, and K. Kurita
Physica Status Solidi A, 2019, 216, 1900175 (2019): Applications and Materials Science.

(18) "Fundamental characteristics of cyanide-related multielement ion-implanted epitaxial Si wafers for high-performance CMOS image sensors"
A. Suzuki, R. Okuyama, A. Masada, S. Shigematsu, T. Kadono, R. Hirose, Y. Koga, and K. Kurita
Physica Status Solidi A, 2019, 216, 1900172 (2019): Applications and Materials Science.

Proceedings

(1) Proximity Gettering Design of Silicon Wafers Using Hydrocarbon Molecular Ion Implantation Technique for Advanced CMOS Image Sensors
K. Kobayashi, R. Okuyama, T. Kadono, A. Onaka-Masada, R. Hirose, S. Shigematsu, A. Suzuki, Y. Koga, K. Kurita
2018 22nd International Conference on Ion Implantation Technology (IIT) 16-21 Sept. 2018

(2) Re-crystallization Behavior of Amorphous Layer in Hydrocarbon Molecular Ion Implanted Region Using Flash Lamp Annealing
K. Kurita, T. Kadono, S. Shigematsu, R. Hirose, R. Okuyama, A. Onaka-Masada, H. Okuda, Y. Koga, J.G. Park
2018 22nd International Conference on Ion Implantation Technology (IIT) 16-21 Sept. 2018

International Conference

(1) ” The effect of proximity gettering technology using CH₃O molecular ion implantation on CMOS image sensor fabrication process” (Chapter. 3)

R. Hirose, T. Kadono, R. Okuyama, A. Onaka-Masada, S. Shigematsu, K. Kobayashi,

Y. Koga and K. Kurita

22nd International Conference on Secondary Ion Mass Spectrometry – SIMS-22, October 20 to 25, 2019, Kyoto, Japan.

(2) “Development of CH₃O molecular ion implanted silicon epitaxial wafer for CMOS Image sensor” (Chapter. 4)

R. Hirose, R. Okuyama, T. Kadono, A. Masada, K. Kobayashi, S. Shigematsu, Y. Koga and K. Kurita

The 8th Forum on the Science and Technology of Silicon Materials 2018

(Okayama)

Nov. 18-21, 2018, Okayama, JAPAN

(3) “Development study of Silicon Epitaxial Wafer for CMOS image sensors by using multi-element molecular cluster ion implantation” (Chapter. 4)

R. Hirose, T. Kadono, R. Okuyama, S. Shigematsu, A. Masada, H. Okuda , Y. Koga, and K. Kurita

ICDS 2017:29th International Conference on Defect in Semiconductor, July31-August4,2017,Matsue,Japan.

(4) ” Characteristics of Carbon Cluster Ion Implanted Epitaxial Silicon Wafers” - Development study of multi-elements molecular ion implantation technique – (Chapter. 3)

R. Hirose, R. Okuyama, T. Kadono, A. Onaka-Masada, H. Okuda, Y. Koga, K. Kurita, and N. Miyamoto

21th International Conference on Ion Implantation Technology (NCK University, Taiwan, 2016/9/22)